



5-2000

Development and education of a liquid jet atomization and spray evolution simulation

Nancy Diane O'Brien

Follow this and additional works at: https://trace.tennessee.edu/utk_graddiss

Recommended Citation

O'Brien, Nancy Diane, "Development and education of a liquid jet atomization and spray evolution simulation. " PhD diss., University of Tennessee, 2000.
https://trace.tennessee.edu/utk_graddiss/8374

This Dissertation is brought to you for free and open access by the Graduate School at TRACE: Tennessee Research and Creative Exchange. It has been accepted for inclusion in Doctoral Dissertations by an authorized administrator of TRACE: Tennessee Research and Creative Exchange. For more information, please contact trace@utk.edu.

To the Graduate Council:

I am submitting herewith a dissertation written by Nancy Diane O'Brien entitled "Development and education of a liquid jet atomization and spray evolution simulation." I have examined the final electronic copy of this dissertation for form and content and recommend that it be accepted in partial fulfillment of the requirements for the degree of Doctor of Philosophy, with a major in Mechanical Engineering.

Roy J. Schulz, Major Professor

We have read this dissertation and recommend its acceptance:

Charles Merkle

Accepted for the Council:

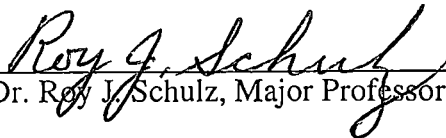
Carolyn R. Hodges

Vice Provost and Dean of the Graduate School

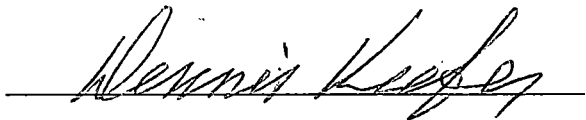
(Original signatures are on file with official student records.)

To the Graduate Council:

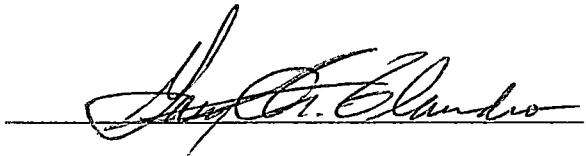
I am submitting herewith a dissertation written by Nancy Diane O'Brien entitled "Development and Evaluation of a Liquid Jet Atomization and Spray Evolution Simulation." I have examined the final copy of this dissertation for form and content and recommend that it be accepted in partial fulfillment of the requirements for the degree of Doctor of Philosophy, with a major in Mechanical Engineering.


Dr. Roy J. Schulz, Major Professor


We have read this dissertation
and recommend its acceptance:







Accepted for the Council:


Associate Vice Chancellor
and Dean of The Graduate School

Development and Evaluation of a Liquid Jet Atomization
and Spray Evolution Simulation

A Dissertation
Presented for the
Doctor of Philosophy
Degree
The University of Tennessee, Knoxville

Nancy Diane O'Brien

May, 2000

Acknowledgments

I would like to thank my major professor, Dr. Roy Schulz, for his patience and guidance over the years. I would also like to thank Dr. Charles Merkle for his direction and advice, which proved invaluable in the completion of this work. My greatest thanks goes to my parents, without their love and support I could not have completed this dissertation.

Abstract

A new computer model for liquid atomization and breakup has been developed. The new code, LISAM, was written specifically to model non-reacting liquid sprays injected into simple chamber geometries. Momentum and continuity equations are solved to model the gas flow, and gas/droplet interaction is included through a gas momentum source term. Parametric studies and comparisons with experimental data were performed. Parametric studies yielded conclusions about drop size distributions and spray penetration behavior. Turbulence modeling is not currently included in LISAM, however the results of parametric simulations with viscosity levels set at higher levels suggest that turbulence effects may be important for both drop sizes and spray dispersal. Parcel injection rates must be large enough to ensure statistically significant results. Trade-offs in parcel injection rate and grid density must be made to find a level that provides accurate predictions without resulting in unreasonably high run times. Comparisons with NASA water/air experiments underscored the need for more complete experimental information. Experimental researchers need to provide as much detailed information on experimental setup and data acquisition as possible. Simple test configurations that provide drop size and velocity distributions as well as spray penetration rates and even gas field visualization would be useful for detailed evaluation of code models.

TABLE OF CONTENTS

Chapter	Page
1 An Introduction to Liquid Sprays	1
1.1 Introduction	1
1.1.1 What is Liquid Atomization and Why is it Important?	1
1.1.2 Computer Simulation of Liquid Atomization	2
1.2 Mechanics of Liquid Jet Atomization	3
1.2.1 Liquid Jet Breakup Regimes	4
1.3 Computational Modeling of Liquid Atomization	6
1.4 Organization and Purpose of This Dissertation	6
2 LISAM Computer Simulation	8
2.1 Introduction	8
2.2 LISAM Overview	8
2.2.1 Features and Assumptions	9
2.2.2 Input Parameters	10
2.2.3 Output Parameters	10
2.2.4 Program Logic	10
2.2.5 Grid Generation	13
2.2.6 Solving the Flow Equations	13
2.3 LISAM Description	14
2.3.1 Liquid Phase Modeling	15
2.3.1.1 Liquid Injection and Breakup	16
2.3.1.1.1 Reitz Model	16
2.3.1.1.1.1 Reitz Model Breakup Criteria	23
2.3.1.1.2 O'Brien Model	27

2.3.1.1.3 Taylor Analogy Model	29
2.3.1.1.4 Non-Dimensional Breakup Time Model	34
2.3.1.1.5 Andrews Model	37
2.3.1.2 Liquid Collision and Coalescence	44
2.3.1.3 Gravitational Effects	47
2.3.1.4 Droplet Drag	48
2.3.1.4.1 Velocity Adjustment Due to Drag	49
2.3.2 Gas Phase Modeling	51
2.3.2.1 Solving the Gas Momentum Equation	54
2.3.2.1.1 Gas Momentum Equation Numerical Methods	57
2.3.2.1.2 Momentum Equation Boundary Conditions	58
2.3.2.2 Solving the Gas Continuity Equation	59
2.3.2.2.1 Continuity Equation Boundary Conditions	59
2.3.2.2.2 Solving for Gas Pressure	60
2.3.2.3 Dual Timestepping	60
2.3.3 Particle Mover	62
2.4 LISAM Summary	63
3 Spray Characterization and LISAM Data Analysis Techniques	64
3.1 Introduction	64
3.2 Experimental Techniques	64
3.3 Spray Characterization	67
3.3.1 Drop Size Measurements	67
3.3.2 Spray Penetration Rate	70
3.3.3 Particle Locations and Distributions	71
3.3.4 Flow Field Quantities	71
3.4 Evaluating Simulation Results	72

4 LISAM Simulation Results and Comparisons	73
4.1 Introduction	73
4.2 Experimental Data	73
4.2.2 Diesel Spray Data	78
4.3 Computational Studies	79
4.3.1 Results of Parametric Studies	79
4.3.1.1 Comparison of Baseline Results with Experiment	82
4.3.1.2 Impact of Statistics on LISAM Predictions	89
4.3.1.3 Time-Averaged Sauter Mean Diameter Measurements	91
4.3.1.4 Spraytip Penetration Rates	105
4.3.2 Comparison of LISAM results to Water/Air Experiment	124
4.3.3 Summary of Computational Studies Using LISAM	149
5 Conclusions and Recommendations	151
5.1 Introduction	151
5.2 Conclusions	151
5.3 Recommendations for Future Work	152
References	153
Appendices	157
Appendix A Sample LISAM Input File	158
Appendix B Discretization of Gas Momentum Equation	159
Vita	163

LIST OF TABLES

Table	Page
2-1. LISAM Input Parameters.	11
4-1. Configurations for Experimental Studies.	75
4-2. Water/Air Injection Experiments Modeled using LISAM.	77
4-3. Lisam Parametric Studies Using Tetradecane/Nitrogen.	80
4-4. Grid Configurations for Parametric Studies.	81

LIST OF FIGURES

Figure	Page
1-1. Illustration of Liquid Jet Atomization Regimes.	5
2-1. LISAM Logic Flow Chart.	12
2-2. Probability Function and Distribution of the Non-Dimensional Breakup Time.	36
2-3. Diagram for Andrews Liquid Core Injection Model.	42
2-4. Sketch of Steady State Andrews Model Core Behavior.	43
2-5. Area Weighting of Gas Velocity.	52
2-6. Flow Chart for Gas Solver Sub-Iteration Process.	53
2-7. Two dimensional Staggered Grid.	55
2-8. Three Dimensional Staggered Grid.	55
4-1. Diagrams of Experimental Configurations	76
4-2. Comparison of Computational and Experimental Time Averaged Sauter Mean Diameters.	83
4-3. Drop Size Population and Percent Mass Distributions at 6.6 cm for Baseline LISAM Prediction.	85
4-4. Comparison of Computational and Experimental Tip Penetration Histories. ...	86
4-5. Baseline Spray Pattern at 4.5 msec.	87
4-6. Enlarged View of Baseline Spray Pattern at 4.5 msec.	88
4-7. Baseline Spray Pattern at 4.5 msec 'X-Y' view.	90
4-8. Spray Pattern for $Pinj=10^4$	92
4-9. Spray Pattern for $Pinj=10^5$ (Baseline).	93
4-10. Spray Pattern for $Pinj=10^6$	94

4-11.	Spray Pattern for $\text{Pinj}=10^7$.	95
4-12.	Axial Distribution of SMD for Various Breakup Models.	97
4-13.	Axial Distribution of SMD for Various Values of B_1 in Reitz Model.	98
4-14.	Axial Distribution of SMD with Variation of B_1 in Andrews Model.	99
4-15.	Axial Distribution of SMD With and Without Collisions.	100
4-16.	Drop Size Population and Percent Mass Distribution at 6.6 cm for LISAM Simulation with Collisions.	103
4-17.	Sauter Mean Diameter Distributions with Variation in Drag Routine.	104
4-18.	Spray Penetration for Different Grid Spacings.	106
4-19.	Centerline Gas Axial Velocity Profiles for Different Grid Spacings after 1 msec.	107
4-20.	Spray Penetration Variation Due to Breakup Model.	109
4-21.	Spray Penetration for Various Values of B_1 Using Reitz Model.	110
4-22.	Spray Penetration for Various Particle Injection Rates.	111
4-23.	Spray Penetration for Different $\Delta\tau$.	113
4-24.	Centerline Gas Axial Velocity Profiles for Different $\Delta\tau$ at 1 msec.	114
4-25.	Spray Penetration for Various Differencing Schemes.	115
4-26.	Centerline Gas Axial Velocity Profiles for Different Differencing Schemes at 1 msec.	116
4-27.	Convergence Criteria Effect on Spray Penetration.	117
4-28.	Centerline Gas Axial Velocity Profiles for Different Convergence Criteria at 1 msec.	118
4-29.	Spray Penetration Variation for Different Drag Routines.	119
4-30.	Variation in Spray Penetration with Various Definitions of Tip Location.	121
4-31.	Spray Penetration Rate with Adjusted Initial Velocity.	122

4-32.	Comparison of Numerical and Experimental Drop Sizes for Case w1. . . .	126
4-33.	Comparison of Numerical and Experimental Drop Sizes for Case w1 (Enlarged View).	127
4-34.	Comparison of Numerical and Experimental Axial Velocities for Case w1.	128
4-35.	Comparison of Numerical and Experimental Drop Sizes for Case w2. . . .	129
4-36.	Comparison of Numerical and Experimental Axial Velocities for Case w2.	130
4-37.	Comparison of Numerical and Experimental Drop Sizes for Case w3. . . .	131
4-38.	Comparison of Numerical and Experimental Axial Velocities for Case w3.	132
4-39.	Drop Size Population Distribution at a Radius of 0.035 cm and an Axial Location of 5.1 cm for Case w3.	134
4-40.	Drop Size Population Distribution at a Radius of 1.0 cm and an Axial Location of 5.1 cm for Case w3.	135
4-41.	Comparison of Numerical and Experimental Drop Sizes for Case w4. . . .	136
4-42.	Comparison of Numerical and Experimental Axial Velocities for Case w4.	137
4-43.	Comparison of Numerical and Experimental Drop Sizes for Case w5. . . .	138
4-44.	Comparison of Numerical and Experimental Axial Velocities for Case w5.	139
4-45.	Comparison of Numerical and Experimental Drop Sizes for Case w6. . . .	140
4-46.	Comparison of Numerical and Experimental Axial Velocities for Case w6.	141
4-47.	Comparison of Numerical and Experimental Drop Sizes for Case w7. . . .	142
4-48.	Comparison of Numerical and Experimental Axial Velocities for Case w7.	143
4-49.	Comparison of Numerical and Experimental Drop Sizes for Case w8. . . .	144
4-50.	Comparison of Numerical and Experimental Axial Velocities for Case w8.	145
4-51.	Comparison of the Effects of Methods of Average Drop Size Calculation.	147
4-52.	Effect of Varying Initial Drop Size.	148

LIST OF SYMBOLS

a_{parcel}	droplet acceleration in ϕ direction [cm/sec ²]
A	undamped oscillation amplitude
A_1	empirical constant = 0.188
b	collision impact parameter
b_{cr}	critical value of impact parameter
B_0	empirical constant, = 0.61
B_1	empirical constant, = 10
B_b	empirical constant, = 2.9
B_c	empirical constant, = 7
C_b	constant of proportionality, = 1/2
C_d	damping force constant, = 5
C_D	drag coefficient for the drop
C_F	external force constant, = 1/3
C_k	restoring force constant, = 8
D	liquid orifice diameter [cm]
D_{10}	mean length diameter [cm], [μm]
D_{30}	mean volumetric diameter [cm], [μm]
D_{32}	sauter mean diameter [cm], [μm]
D_{mv}	mean volumetric diameter [cm], [μm]

F	force [dynes]
F_D	aerodynamic drag force on drop [dynes]
g_ϕ	gravitational acceleration in the ϕ direction
h	generic grid cell width [cm]
L	length [cm]
L_b	liquid jet length when breakup occurs [cm]
L_{core}	length of liquid core [cm]
$L_{core_{ss}}$	steady liquid core length [cm]
L_{core_t}	transient liquid core length [cm]
\dot{m}	mass flow rate [g/sec]
m_{child}	mass in 'child' parcel [g]
m_{core}	liquid mass in core [g]
m_p	mass per computational particle injected [g]
m_{parcel}	total mass in a computational parcel [g]
m_{parent}	mass in 'parent' parcel [g]
m_{prev}	the total mass that has previously been injected into the system [g]
n	number of collisions
\bar{n}	mean value of the number of collisions, n
np_{inj_n}	number of computational particles that should be injected in timestep n
N	number of e-folding times before λ_d appears, = 11
N_{grid}	number of grid points in a given coordinate direction

N_x	number of particles in parcel x
p_n	number of physical particles per computational particle
P	gas pressure [dynes/cm ²]
P_{inj}	rate at which computational particles are injected [particles/sec]
P_n	Poisson distribution
r_1	radius of drop in parcel containing larger drops in collision calculation [cm]
r_2	radius of drop in parcel containing smaller drops in collision calculation [cm]
r_{32}	Sauter mean radius
r_{child}	radius of 'child' drop
r_{new}	radius of new drop [cm]
r_p	particle radius [cm]
R	chamber radius [cm] or gas constant [erg/g·K]
\mathcal{R}	random number
Re	Reynold's number
S_{drop}	source term for gas-liquid interactions
t	time [sec]
t_b	time at which λ_b appears [sec]
t_{bu}	critical time for TAB breakup
t_d	viscous damping time or time at which λ_d appears [sec]
t^n	time at the end of timestep n [sec]
T	Taylor parameter or gas temperature [K]
u_g	'x' component of gas transverse velocity [cm/sec]

u_p	'x' component of parcel transverse velocity [cm/sec]
v_g	'y' component of gas transverse velocity [cm/sec]
v_p	'y' component of parcel transverse velocity [cm/sec]
V_{err}	velocity convergence criteria
V_{gas}	gas velocity in ϕ direction [cm/sec]
V_{inj}	liquid axial velocity at injection [cm/sec]
$V_{p,\phi}$	droplet velocity in ϕ direction [cm/sec]
V_r	droplet radial velocity [cm/sec]
V_{rad}	droplet radial velocity [cm/sec]
V_{rel}	liquid-gas relative velocity [cm/sec]
V_{wave}	wave speed of the fastest growing wave [cm/sec]
V_x	magnitude of the velocity vector for parcel x [cm/sec]
V_ϕ	velocity in the ϕ direction [cm/sec]
Vol_{cell}	volume of a computational cell [cm ³]
w_g	axial gas velocity [cm/sec]
w_p	axial drop velocity [cm/sec]
W_n	weighting function
We	Weber number
x	drop distortion [cm] or transverse chamber direction
\dot{x}	dx/dt
\ddot{x}	d^2x/dt^2
x_p	droplet 'x' radial position [cm]

X_{injector}	x location of injector [cm]
y	non-dimensional drop distortion or transverse chamber direction
\dot{y}	dy/dt
y_p	droplet 'y' radial position [cm]
Y_{injector}	y location of injector [cm]
z	axial chamber direction
Z	Ohnesorge parameter
z_p	droplet axial position [cm]
α	empirical constant, = 4
γ	r_1/r_2
Δm_{inj}	mass that should be injected during timestep [g]
Δt	computational timestep [sec]
ΔV_{child}	magnitude of velocity change for 'child' parcel [cm/sec]
Δx	grid spacing in x direction [cm]
Δy	grid spacing in y direction [cm]
Δz	grid spacing in z direction [cm]
$\Delta \tau$	dual timestep [sec]
ϕ	x,y or z position [cm]
ϑ	liquid void fraction [volume of gas/volume of cell]

θ	liquid spray angle [rad]
Θ	maximum spray angle [rad]
λ_b	wavelength for core break [cm]
λ_d	dominant wavelength [cm]
Λ	characteristic wavelength [cm]
μ	kinematic viscosity [dynes-sec/cm ²]
ν	collision frequency [collisions/sec]
ρ	density [g/cm ³]
ρ_{err}	density convergence criteria
σ	liquid surface tension [g/sec ²]
τ	characteristic time for droplet breakup [sec]
τ_d	e-folding time [sec]
ϕ_{ran}	random angle [0:2 π] [rad]
ω	oscillation frequency [rad/sec]
Ω	characteristic wave growth rate [rad/sec]

Superscripts

n	current time level
$n+1$	next time level

Subscripts

- 1 parcels with larger drops
- 2 parcels with smaller drops
- g gas
- liq liquid
- ϕ any (x,y, or z) coordinate axis

Chapter 1

An Introduction to Liquid Sprays

1.1 Introduction

The dispersal of liquids into gas (liquid spraying) is an important and common problem in engineering applications. Liquid sprays are found in a wide variety of industrial and commercial applications. They provide fuel for combustion processes in rockets, gas turbines, furnaces, and automobile engines [1]. They deliver agricultural materials for crop dusting and fertilization [1]. Liquid sprays are also used in industrial and commercial paint spraying, as well as, many other applications [1]. As the role of liquid spraying in advanced technologies expands, so does the need to describe and predict the behavior of these sprays. Computer simulations of liquid spray behavior in a gas allow engineers to optimize the configuration of a liquid injection system to meet the needs of a specific liquid spray problem. This dissertation focuses on the development, evaluation and application of a numerical liquid injection, atomization and spray evolution simulation for the prediction of the behavior of a liquid sprayed into a gas.

1.1.1 What is Liquid Atomization and Why is it Important?

Liquid atomization is a process where liquid is changed from a large continuous mass to a distribution of small drops [1]. Atomization occurs when the surface tension forces that serve to hold the fluid together are overcome by internal forces, like those created by the liquid's radial velocity, and external forces, e.g. aerodynamic forces [1]. Even after a liquid droplet has broken away from the main body it can still atomize

further if conditions are right. This multi-stage process creates a wide range of drop sizes that depend not only on the initial injection conditions of the bulk liquid, but also on the conditions that can allow secondary atomization (breakup of initial or primary drops) to occur [1].

The desired distribution of drop sizes is very dependant on the process or application being considered. In combustion processes, a well dispersed spray of small droplets promotes more efficient heat and mass transfer between liquid and gas [2]. A well vaporized spray uses less fuel and reduces pollutants by promoting more complete combustion. A large number of very small drops will have a great deal more surface area than a few large drops. This large amount of surface area helps promote mixing and evaporation, and therefore, a more efficient combustion process [1,3]. For other applications, however, very small drops would not be desirable. In crop spraying, small, low velocity drops would be more prone to evaporation and drifting to the wrong settling location [1]. These effects would result in poor spray coverage and wasted liquid [1]. Therefore, for these applications, an injection process that results in larger droplets is required. The ability to predict the performance of a liquid injection system without expensive trial-and-error testing is extremely advantageous.

1.1.2 Computer Simulation of Liquid Atomization

By using computer simulations, many different liquid injection configurations can be evaluated without the time or expense of real-world testing. Also, there are significant difficulties in accurately measuring droplet/spray characteristics in dense sprays. The lack of reliable data makes computational prediction of spray characteristics even more valuable.

There have been many different approaches to the modeling of liquid spray atomization [4, 5, 6, 7,8]. Most attempt to model the formation and growth of waves on the surface of liquid jets and drops. By predicting how these waves grow and disrupt the liquid, it is hoped that droplet behavior during atomization can be predicted. Generally, droplet (or jet) disintegration will begin when the wavelength of the disturbing wave grows to an appreciable fraction of the droplet (or jet) diameter. Details of several atomization modeling methods are given in Chapter 2.

1.2 Mechanics of Liquid Jet Atomization

As a liquid column, or jet, passes through a gas field there are competing forces on the surface of the liquid. Surface tension forces tend to hold the liquid column together, while external aerodynamic forces tend to pull the surface apart. The conflict between these opposing forces creates perturbations on the liquid surface which, if large enough, will lead to the breakup of the liquid column [1]. The breakup of the liquid jet is referred to as the 'primary' atomization process [1]. If the resulting droplets are large enough, they too will undergo a breakup process, known as 'secondary' atomization [1]. Many different properties contribute to the atomization process, making it difficult to accurately model. The physical properties of the liquid and gas, the velocities and temperatures of both fluids, and the injector configuration all contribute to the atomization process [9]. To better describe the breakup of liquid jets the atomization process is broken into different regimes which describe the behavior of the jet during breakup.

1.2.1 Liquid Jet Breakup Regimes

Liquid jet breakup is commonly broken into four regimes [1]:

- **Rayleigh regime** Breakup occurs many jet diameters downstream of the nozzle and is caused by axisymmetric wave growth. Surface oscillations are induced by surface tension forces. The resulting drops have a diameter larger than the jet diameter. [9] (See Figure 1-1a)
- **First wind-induced breakup regime** Breakup also occurs many jet diameters from the nozzle, but the drops are now smaller than the jet diameter. The relative liquid/gas velocity induces a pressure distribution across the jet which augments the surface tension effect seen in the Rayleigh regime. [9] (See Figure 1-1b)
- **Second wind-induced breakup regime** The relative liquid/gas motion induces short wavelength waves. The unstable growth of these waves causes jet breakup closer to the nozzle and results in drops much smaller than the jet diameter. In this regime, the wave growth induced by the relative velocity is opposed by surface tension forces. [9] (See Figure 1-1c)
- **Atomization regime** The jet completely disintegrates at the nozzle and breakup is complete. Average drop size is substantially smaller than the nozzle diameter. The breakup mechanism is not well understood. [9] (See Figure 1-1d)

By defining the characteristics of different regimes of liquid jet breakup, physical models can be developed to represent the behavior of liquid during an injection process.

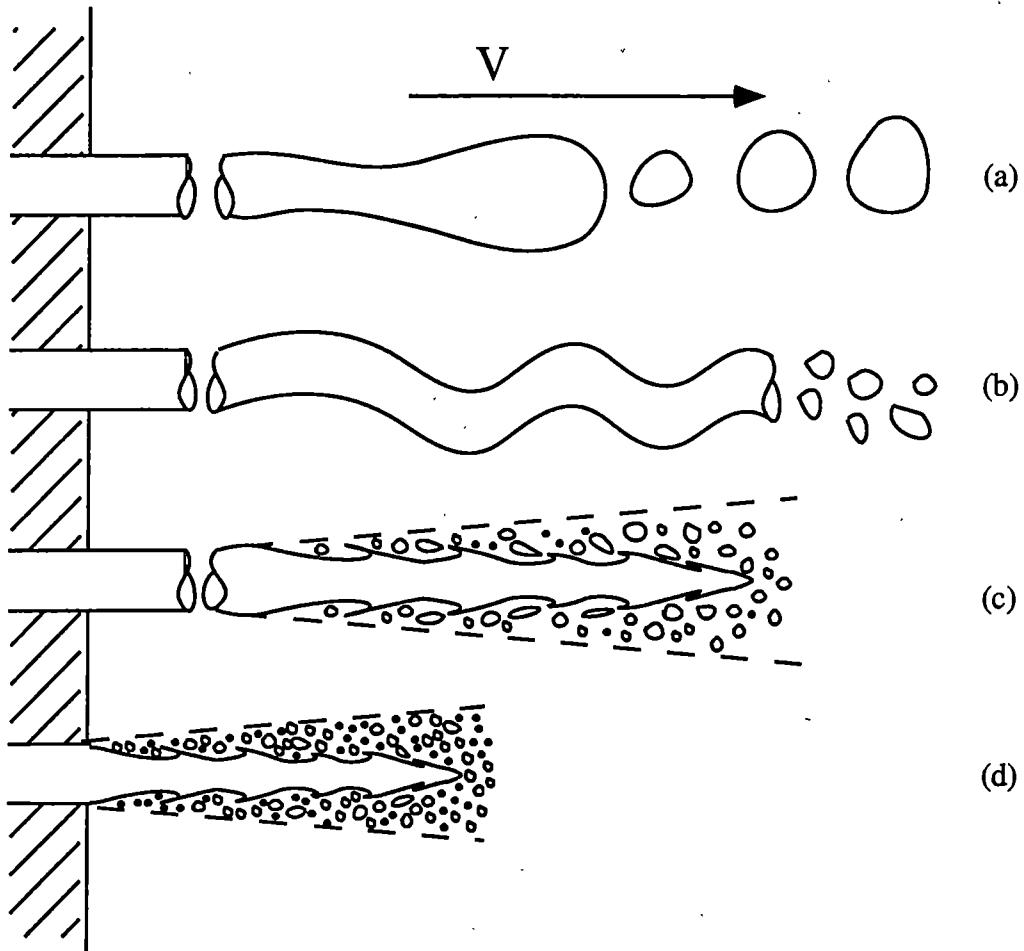


Figure 1-1. Illustration of Liquid Jet Atomization Regimes.

Adapted from: [10]

1.3 Computational Modeling of Liquid Atomization

Typically, computer programs attempting to model the behavior of a two-phase, liquid/gas, system rely on a combination of techniques to predict the behavior of the flow. The gas flow is modeled by solving the Navier-Stokes equations using any of the commonly used computational fluid dynamics methods for internal flows [11]. The presence of the liquid phase in the gas flow is accounted for in the momentum conservation equations by including a source term [4,5,6,12], thereby coupling the gas behavior to the liquid behavior. The liquid flow is typically modeled using a stochastic computational particle technique [4,6,12] with randomization of velocities and directions of drops and Monte Carlo techniques included to allow a relatively small number of computational particles to represent a large number of physical liquid droplets [4,12]. (See Chapter 2 for a complete description of the techniques used in this dissertation.)

1.4 Organization and Purpose of This Dissertation

This dissertation describes a study in which various computational injection/breakup models were critically examined to determine their relative effectiveness. To make a consistent evaluation of these models, they were all tested using the same numerical code to resolve the gas flow field. The gas solver was also developed as part of this dissertation work so that all of the variables that can effect the predicted jet atomization behavior and spray evolution could be controlled. This consistent framework allowed the author to study the effects on the predicted results of computational parameters such as grid density, grid dimensions, timestep, etc. (see Chapter 4). Comparisons to experimental and other computational data were also made. A complete description of the computer program used in these studies is given in

Chapter 2. Data analysis is discussed in Chapter 3, and results are presented in Chapter 4. Chapter 5 presents conclusions drawn from this study and makes recommendations for future work.

The overall purpose of this study was to provide a computational environment in which to conduct a critical review, evaluation, comparison and development of liquid injection and atomization models for single stream and coaxial injectors. Also, the computer code provides a framework for predicting the performance of new liquid injector designs, particularly for liquid rocket motors. The user can select a liquid injection and atomization model to use from a menu of those models incorporated into the code. This will significantly reduce the computational effort and expense of evaluating new injector designs.

Chapter 2

LISAM Computer Simulation

2.1 Introduction

Preliminary studies of liquid sprays for this work were made by the author using the computer simulation program KIVA-3 [13], developed by Los Alamos National Laboratory. KIVA-3 is capable of modeling complex chemically reacting flows with moving grids [13]. Based on the author's experience with the KIVA-3 program the decision was made to write a new more efficient code specifically to model non-reacting liquid sprays injected into simple chamber geometries. This effort resulted in the code described in this chapter. Many of the liquid modeling concepts used in this code were taken directly from KIVA [12], however, different assumptions and solution techniques were used in other areas of the code, including atomization modeling and gas flow modeling.

2.2 LISAM Overview

This section provides a detailed description of the computer simulation developed to model the behavior of liquid jets injected into a gas filled chamber. The primary modeling features and assumptions of the Liquid Injection Spray Atomization Model (LISAM) are given. Input and output parameters are discussed. An overview of the program logic is presented. Grid generation is outlined and the gas flow solver is briefly discussed.

After this basic introduction to LISAM, a detailed discussion of both the liquid

and the gas phase models is presented, including discussion of the various atomization models used and an in-depth description of the gas phase equations and solution techniques.

2.2.1 Features and Assumptions

The primary features and assumptions of the Liquid Injection Spray Atomization Model (LISAM) are:

- three dimensional, time dependent code with gas phase modeled using an Approximate Factorization computational fluid dynamics technique [11], coupled with a particle-in-cell liquid phase model
- rectangular, uniform grid
- a single straight tube and a coaxial liquid/gas injector were modeled
- inner iterations and dual time stepping numerical techniques are implemented for solving the gas flow
- gas velocity, gas pressure and gas density are solution variables
- liquid and gas temperature and viscosity are assumed to be constant
- turbulence effects are not modeled
- liquid phase change (evaporation) is not modeled

Features of LISAM that were taken from KIVA-3 directly include the particle/gas drag model (Section 2.3.1.4), the particle collision/coalescence model (Section 2.3.1.2) and particle/gas momentum source term calculation (Section 2.3.2.1) [12].

2.2.2 Input Parameters

The LISAM code requires input parameters that describe both the gas and liquid injection, the physical dimensions of the chamber, and the computational parameters needed. A sample input file is shown in Appendix A. A detailed listing of input parameters is given in Table 2-1. All variables in LISAM are in cgs (cm-grams-sec) units, to maintain consistency and continuity with KIVA.

2.2.3 Output Parameters

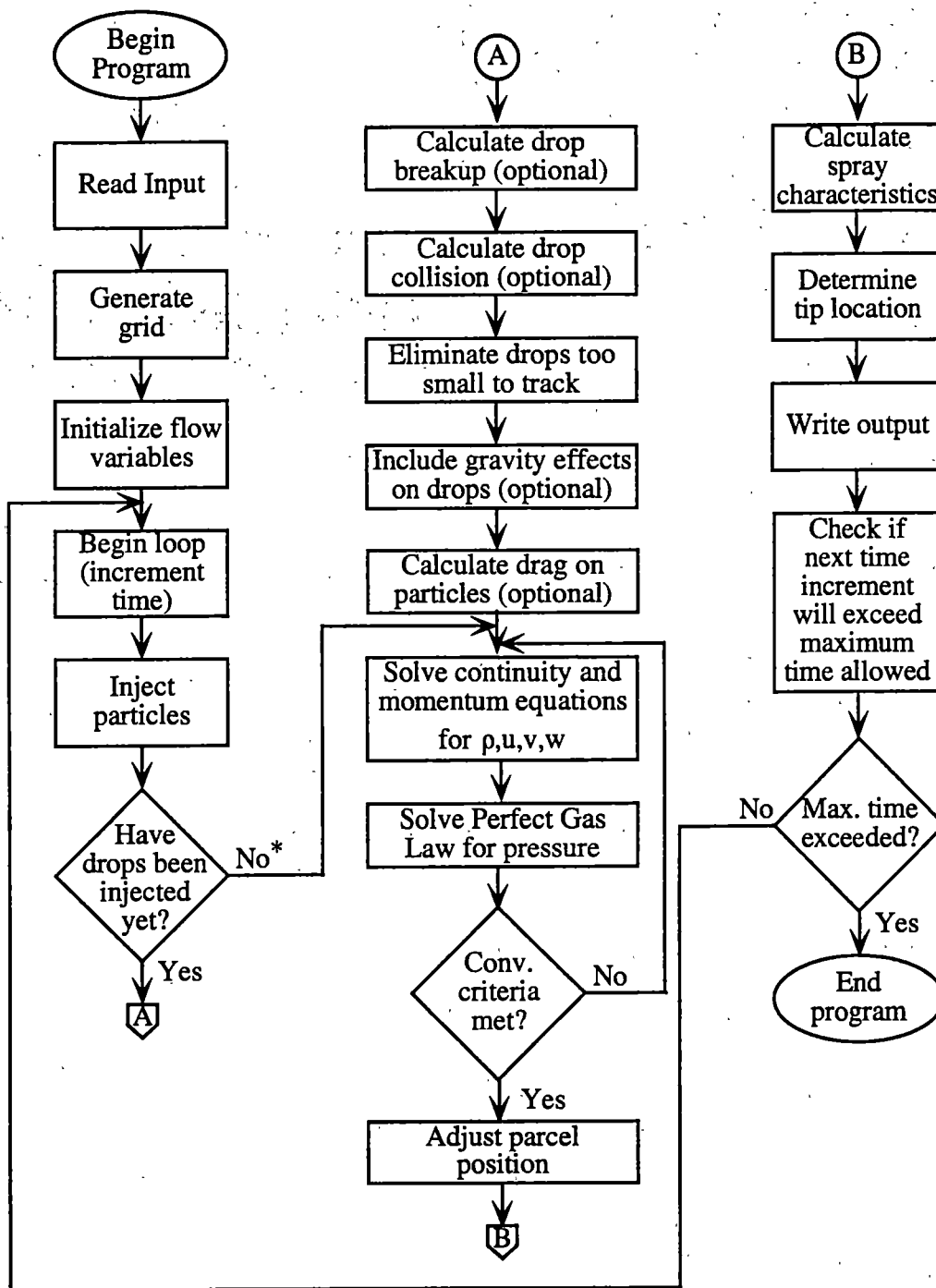
All pertinent gas and liquid properties are available as output. Distributions of gas pressure, density, and velocity are available, as well as the positions, velocities, and sizes of droplets. With this information the flow field can be characterized and conclusions about the predicted liquid spray behavior can be drawn.

2.2.4 Program Logic

LISAM can be divided into three computational phases: input and program control operations; droplet and gas flow computation; and output control. A flow chart of LISAM logic is shown in Figure 2-1. The first column in the flow chart shows the basic program control mechanisms of LISAM: parameter input, grid generation, variable initialization. The first column also includes the time incrementation, particle injection, and a computational logic check for droplet presence. Column two contains the primary functions of LISAM: particle breakup, particle drag calculation, gas flow solver and particle mover. Column three shows the output control functions in LISAM: data output and program shutdown. A detailed description of LISAM's primary functions (column

Table 2-1. LISAM Input Parameters.

Code control parameters	Physical dimensions	Gas properties	Liquid properties
primary timestep	chamber width	injection velocity	injection velocity
dual timestep	chamber length	pressure	density
relaxation factors (velocities and density)	gas annulus diameter	temperature	viscosity
convergence criteria	post thickness	viscosity	surface tension
grid dimensions	liquid nozzle diameter	gas constant	particle injection rate
restart file (in/out)		gravitational acceleration	droplet breakup model
			collision model (y/n)
			drag model (y/n -single/cluster)



* - It can take several cycles at the beginning of the program before the first liquid parcel is injected.

Figure 2-1. LISAM Logic Flow Chart.

2) will be given in Section 2.3.

2.2.5 Grid Generation

LISAM utilizes a very basic grid generation scheme. It calculates a uniform Cartesian grid in each coordinate direction. The number of grid points in each direction is a LISAM input. The spacing in a coordinate direction is defined as:

$$h = \frac{L}{N_{\text{grid}} - 1} \quad (2.1)$$

where

h = the width of a grid cell,

L = the total dimension in the coordinate direction,

N_{grid} = the number of grid points in the coordinate direction.

Details of how the grid is applied to the two-phase modeling situation, including the implementation of a staggered grid, are given in Section 2.3.2.

2.2.6 Solving the Flow Equations

The liquid and gas flow fields in LISAM are coupled. The particle behavior affects the gas behavior and vice versa. By calculating the drag effects the gas has on a particle, a new particle velocity can be determined (see Section 2.3.1.4) and a particle drag momentum source term for the gas momentum equation can be calculated (see Section 2.3.2.1). In this way, the gas momentum equations are coupled to the particle movements, just as the particle movements are coupled to the gas. A complete

description of this algorithm is given in Section 2.3.2.2.

The gas flow equations are also coupled to each other. The momentum equations for the three velocity components are solved sequentially for their respective velocity component. Once all components are found, the continuity equation is solved for density. The perfect gas law is then used to solve for pressure (with temperature held constant). In this way, each velocity component is coupled to the others and they are all coupled to density and pressure. The momentum solver is described in Section 2.3.2.1 and the continuity solver is described in Section 2.3.2.2.

2.3 LISAM Description

LISAM is a computer code that predicts three-dimensional, time dependent, two phase flows. It uses a Cartesian coordinate system with the z axis oriented along the chamber length (the 'axial' direction). The 'x' and 'y' notation refers to properties perpendicular to the chamber axis (in the 'transverse' direction). This gives a computational domain that is a rectangular box. The origin of the coordinate system is placed at the center of the injection plane. All other spatial variables are referenced from this point.

In the following sections, the various components of the LISAM code will be described in detail. The computational algorithm can be broken into two sections, one modeling the liquid (droplet) phase and the other modeling the gas phase. The two phases are coupled but solved sequentially: liquid then gas.

2.3.1 Liquid Phase Modeling

The liquid phase is modeled in several steps. The first step is the introduction of liquid into the system using an injection model that is based on mono-disperse drop size distributions. However, any initial drop size distribution could be incorporated. Once liquid particles (droplets) have been introduced into the system, their physical behavior (breakup, interaction, and movement) is modeled. Droplet injection and breakup in LISAM can be modeled using one of several different techniques: a liquid injection and breakup model developed by Reitz [4], the O'Brien model (a modified version of the Reitz model developed for LISAM), the Taylor Analog Breakup model used in KIVA [12], a non-dimensional time breakup model [14], and an injection and breakup model developed by Andrews [5]. Collisions between particles which can lead to droplet coalescence or a change in droplet velocity and direction can be simulated. After breakup and collision, any droplets that have been broken into particles small enough to be considered vapor (0.1% of initial droplet mass) are removed from the system. Gravitational effects on the particle velocities are accounted for (optionally), and the effect of the gas motion on the drops (causing either droplet deceleration or acceleration) is calculated. These gas interaction effects are also used to compute the particle/gas interaction momentum source term used in the gas momentum equation (see Section 2.3.2.2). The gas flow is now solved (see Section 2.3.2.2). Once a new gas field has been determined, the particle positions are updated (see Section 2.3.3), and a new iteration is begun.

2.3.1.1 Liquid Injection and Breakup

As previously stated, LISAM incorporates several injection/breakup models which the user selects for predicting injection, atomization and spray evolution. The injection model used depends on the breakup model that has been chosen by the user. Each atomization (breakup) model makes different assumptions of how liquid enters the system; these assumptions must be accounted for in the corresponding injection routine. The first injection/atomization model to be discussed was developed by Reitz and Diwakar [6] and later modified by Reitz [4].

2.3.1.1.1 Reitz Model

The Reitz injection model assumes that liquid enters the system as discrete computational packets or parcels comprising several physical droplets, with each physical particle having a diameter equal to the injector nozzle diameter. This injection method creates a mono-disperse jet [4]. Reitz's model involves several steps:

- determine the number of computational particles to inject,
- compute the number of real particles represented by each computational particle,
- determine their initial position in the chamber, and
- specify their injection velocity based on input values.

The first step in the liquid injection model is to determine the number of particles to inject during the current timestep. The computational particle injection rate, P_{inj} , (an input parameter), when combined with the injected liquid mass flow ($\dot{m}_{liq} = \rho VA$), determines the number of computational particles that should be injected during timestep n [12].

$$np_{inj_n} = \frac{\Delta m_{inj}}{m_p} \quad (2.2)$$

where

np_{inj_n} = number of computational particles that should be injected in timestep n,

Δm_{inj} = the mass that should be injected during this timestep [g],

m_p = the mass per computational particle injected [g/particle], $= \frac{\dot{m}_{liq}}{P_{inj}}$,

where

P_{inj} = the rate at which computational particles are injected
[particles/sec],

\dot{m}_{liq} = the physical liquid mass injection rate [g/sec].

The expected injected mass, Δm_{inj} , is the maximum possible mass of liquid that *could* be injected during this timestep. It is defined as [12]:

$$\Delta m_{inj} = (\dot{m}_{liq} \cdot t^n) - m_{prev} \quad (2.3)$$

where

$t^n = \sum_{i=1}^n \Delta t_i$, time at the end of the timestep n [sec],

$m_{prev} = \sum_{i=1}^{n-1} np_{inj_i} m_p$ = the total mass that has previously been injected into the
system [g].

This expected injected mass fixes the maximum number of particles that can be injected

into the system. The number of computational particles injected must, however, be a discrete integer. For example, if $np_{inj} < 1$, no particles would be injected during the i th timestep. The uninjected mass from that and subsequent timesteps would then accumulate until enough mass to form a computational particle is available. This method of accumulating excess mass ensures that mass that should be injected into the system is not lost to due particle discretization [12].

Once the number of computational particles to be injected during a timestep has been determined, the size of the physical particles can be assigned, and the number of physical particles per computational particle can be calculated. The Reitz model assumes a mono-disperse jet [4], i.e. all the physical droplets have the same initial diameter equal to the nozzle diameter, an input parameter. The physical drop size and mass per computational particle, m_p , are then used to calculate the number of physical particles represented by a single computational particle [12], as shown in equation (2.4).

$$p_n = \frac{m_p}{\frac{4}{3} \pi \rho_{liq} r_p^3} \quad (2.4)$$

where

p_n = number of physical particles per computational particle,

ρ_{liq} = input liquid density [g/cm^3],

r_p = physical particle radius (nozzle radius) [cm].

The denominator of equation (2.4) is the mass of a single physical drop. Therefore the ratio of the mass of a computational particle to the mass of a physical particle gives the number of physical drops per computational drop. This value, p_n , does not need to be a discrete integer (unlike np). Because the physical drops are not individually modeled,

partial drops can be represented. Representing multiple physical droplets with a single computational particle allows a liquid spray composed of an extremely large number of physical droplets to be modeled by a relatively small number of computational parcels and changes an unfeasible direct calculation into a manageable statistical model [15]. The value of P_{inj} , rather than p_n , is controlled by the user because it is P_{inj} that directly effects the statistical accuracy of the model results [15, 16]. The number of computational parcels required to adequately model a system is determined by the size of the computational mesh, and the dispersion of the computational parcels within that mesh [15]. As the number of computational parcels is increased, the statistical accuracy of the model will improve, but with a corresponding loss in computational efficiency. Therefore, given computational resources, it is often necessary to balance the need for accuracy in a solution with the computational limitations of the available computing facilities [15, 16].

With the number of both physical and computational particles determined, particle velocities can be computed. The input value of liquid injection velocity is taken to be the axial component of droplet velocity [4]. The radial component of velocity is given by [4]:

$$V_r = V_{inj} \tan\left(\frac{\theta}{2}\right) \quad (2.5)$$

where

V_r = radial component of particle velocity [cm/sec],

θ = the spray angle [rad].

The spray angle used in equation (2.5) is chosen, by pseudo-random number generator, to vary uniformly between 0 and a maximum spray angle, Θ [4]. This maximum spray

cone angle is defined empirically by [4]:

$$\tan\left(\frac{\Theta}{2}\right) = \frac{A_1 \Lambda \Omega}{V_{inj}} \quad (2.6)$$

where

Θ = maximum possible spray angle [rad],

A_1 = empirical parameter = 0.188,

Λ = the wavelength of the fastest growing wave for the droplet, to be defined in equation (2.7)

Ω = the maximum wave growth rate for the droplet, to be defined in equation (2.8).

A_1 is a parameter whose value is nozzle design dependent [4]. The value given here is the one used by Reitz for “sharp entrance constant diameter tube nozzles with length-to-diameter ratios of 4-8” [4]. The parameters Λ and Ω are developed in reference [4].

They “characterize the fastest growing wave on a liquid surface.” [4] They are derived from a perturbation-type stability analysis of flow in a liquid cylinder, where the fastest growing waves on the cylinder is assumed to represent the wave that would most likely result in liquid jet breakup [4]. A curve fit of wave growth rates versus Weber number yields equations for Λ and Ω (Equations (2.7) and (2.8)). A detailed explanation of how Λ and Ω result from this analysis is provided by Reitz [4].

$$\frac{\Lambda}{r_p} = 9.02 \frac{(1 + 0.45Z^{0.5})(1 + 0.4T^{0.7})}{(1 + 0.87We_g^{1.67})^{0.6}} \quad (2.7)$$

$$\Omega \left[\frac{\rho_{liq} r_p^3}{\sigma} \right]^{0.5} = \frac{(0.34 + 0.38We_g^{1.5})}{(1 + Z)(1 + 1.4T^{0.6})} \quad (2.8)$$

where

σ = liquid surface tension (input) [g/sec²],

Z = Ohnesorge parameter, = $\frac{We_{liq}^{0.5}}{Re_{liq}}$,

T = Taylor parameter, = $Z \cdot We_g^{0.5}$,

where

We_x = Weber number = $\frac{\rho_x V_{rel}^2 r_p}{\sigma}$ (x: liq - liquid, g - gas),

Re_{liq} = Reynold's number for a physical droplet = $\frac{V_{rel} \cdot r_p \cdot \rho_{liq}}{\mu_{liq}}$

where

V_{rel} = relative velocity between liquid and gas [cm/sec],

μ_{liq} = liquid kinematic viscosity [dynes-sec/cm²].

With the maximum spray angle determined, a spray angle for the particle injection is chosen. This spray angle determines the radial velocity of the injected computational particle, and therefore that of the physical particles. The two components of the radial velocity are assigned using the polar-to-cartesian transformation. The particles are randomly assigned an angle in the radial plane. The 'x' and 'y'

components of particle velocity are given as:

$$u_p = V_r \cos(\phi_{ran}) \quad (2.9)$$

$$v_p = V_r \sin(\phi_{ran}) \quad (2.10)$$

where

u_p = the 'x' component of transverse velocity [cm/sec],

v_p = the 'y' component of transverse velocity [cm/sec],

ϕ_{ran} = an angle chosen from a uniform deviate [0:2 π] [rad].

Once the parcel velocities have been determined, the location of the new droplets is calculated. Because this injection method places drops in the system at the beginning of an iteration, a randomization technique is used to simulate a continuous injection process [4]. Without this randomization, the particles would be injected in 'waves,' and the injector would appear to operate in a pulsed, rather than continuous, fashion. The initial particle position is determined using equations (2.11), (2.12), and (2.13) [4].

$$x_p = X_{injector} + u_p \cdot \Delta t \cdot \mathcal{R} \quad (2.11)$$

$$y_p = Y_{injector} + v_p \cdot \Delta t \cdot \mathcal{R} \quad (2.12)$$

$$z_p = w_p \cdot \Delta t \cdot \mathcal{R} \quad (2.13)$$

where

x_p = initial x-component of the droplet position [cm],

y_p = initial y-component of the droplet position [cm],

z_p = initial axial droplet position (downstream of injector) [cm],

X_{injector} = x-component of the injector location [cm],

Y_{injector} = y-component of the injector location [cm],

u_p = initial x-component of the liquid velocity [cm/sec],

v_p = initial y-component of the liquid velocity [cm/sec],

w_p = initial axial liquid velocity [cm/sec],

Δt = the input timestep [sec],

$\mathcal{R} = [0:1]$, chosen by a pseudo-random number generator with a uniform deviate.

The use of the fractional random number allows LISAM to simulate a continuous injection of particles by varying the location a particle will first appear in the system (within the limits of the maximum possible distance traveled in a single timestep, $V \cdot \Delta t$).

With particle position, velocity and number known, the particles can be included in the computational model. After particle injection is completed, LISAM determines if any particles in the system have met any breakup criteria.

2.3.1.1.1.1 Reitz Model Breakup Criteria

The Reitz model allows physical droplets to breakup into smaller drops (equation (2.14a)) or grow into larger drops (equation (2.14b)) [4]. The radius of the new drop being formed from an existing particle is given as

$$r_{\text{new}} = \begin{cases} B_0 \Lambda & (B_0 \Lambda \leq r_p) & (2.14a) \\ \min \left[\left(\frac{3\pi r_p^2 V_{\text{rel}}}{2\Omega} \right)^{0.33}, \left(\frac{3r_p^2 \Lambda}{4} \right)^{0.33} \right] & (B_0 \Lambda > r_p, \text{ only once per parent drop}) & (2.14b) \end{cases}$$

where

r_{new} = radius of newly formed drop [cm],

$B_0 = 0.61$, empirical constant [4].

Equation (2.14a) assumes that new, small drops will form with a radius directly proportional to the wavelength of the fastest growing wave on the parent drop [4]. Equation (2.14b) applies to the more unusual situation in which a parent drop actually increases in diameter. This situation occurs physically in the Rayleigh regime (see Section 1.2.1) of liquid injection where it is possible for drops shed from the primary jet to form with a larger diameter than the liquid jet itself [4]. This initial jet-to-droplet breakup process, with droplet growth, is never allowed to happen more than once for each computational particle. Equation (2.14b) “assumes that the jet disturbance has a frequency $\Omega/2\pi$ (a drop is formed each period) or that drop size is determined for the volume of liquid contained under one surface wave” [4]. For all other droplet breakups, the primary particle breakup mechanism is modeled by equation (2.14a).

On a real drop, the wave, of wavelength Λ , that forms on the surface will take a finite time to develop, and induce droplet breakup. To model this behavior in LISAM, the parent particle size is adjusted at each timestep, even if new particles are not created. In this way, the changes in the particle characteristics leading up to droplet breakup are

modeled. Reitz and Diwakar [6] give an expression for the rate at which the size of the parent drop changes prior to shedding a new drop.

$$\frac{dr_p}{dt} = \frac{-(r_p - r_{new})}{\tau} \quad (2.15)$$

where

$$\tau = \frac{3.726 \cdot B_1 \cdot r_p}{\Lambda \cdot \Omega} \quad (2.16)$$

τ is a characteristic time for droplet breakup [4]. In equation (2.15), both r_p , and r_{new} are being adjusted to satisfy the changing conditions of the droplet during its breakup process. The parameter, B_1 , is an empirical constant that is not well defined [4]. Reitz uses the value $B_1 = 10$ for his high speed liquid (>85 m/s) injection studies [4].

During this ‘formation’ period, the parent droplet number, p_n , and size, r_p , are adjusted to conserve mass. The adjusted parent size is found by using an implicit finite difference form of equation (2.15). This form is shown in equation (2.17).

$$r_{p_adj} = \frac{r_p + r_{new} \left(\frac{dt}{\tau} \right)}{1 + \left(\frac{dt}{\tau} \right)} \quad (2.17)$$

As parent particle size is adjusted prior to “new” droplets being created in the system, the number of real droplets per computational particle in the parent parcel must be adjusted to conserve mass. The adjusted physical parent particle number is found using equation (2.18).

$$P_{n_{adj}} = P_n \left(\frac{r_p}{r_{p_{adj}}} \right)^3 \quad (2.18)$$

When the breakup criteria specified by Reitz [4] are satisfied, newly created “child” particles are added to the system as a new computational particle. Reitz sets the breakup criteria to be [4]:

- the total mass that has been accumulated for a “child” computational parcel representing the newly formed drops is greater than 3% of the computational parent’s total injected mass, and
- the number of new drops in the “child” computational parcel is greater than the original number of physical drops in the parent parcel.

The mass transferred from parent parcel to the “child” parcel is calculated as:

$$m_{child} = \frac{4}{3} \pi \rho_{liq} \sum_i n_{p(i)} (r_{p(i)}^3 - r_{p(i)_{adj}}^3) \quad (2.19)$$

where the sum over ‘i’ is over all timesteps since the last parent breakup. The number of real drops in the child computational parcel is determined using equation (2.20)

$$P_{n_{child}} = \frac{m_{child}}{\frac{4}{3} \pi \rho_{liq} r_{child}^3} \quad (2.20)$$

where

$$r_{child} = B_0 \Lambda$$

and Λ has been recalculated as the parent drop radius was changing.

Once the breakup criteria are met, a child computational parcel is introduced to the system at the same location as the parent parcel, but given a velocity vector oriented randomly in a plane normal to the parent’s velocity vector (thus not conserving momentum). The magnitude of the velocity change for the child parcel is given as [4]:

$$\Delta v_{\text{child}} = A_1 \Lambda \Omega = V_{\text{inj}} \tan(\Theta/2) \quad (2.21)$$

This equation is simply a rearranged form of equation (2.6) which defined the parent parcels initial radial velocity components.

After a breakup event has occurred, the number of real particles in the parent parcel is reset to its original value, but the size of the real particles remains at its last calculated reduced value. Total mass of the parent and child parcels is, therefore, conserved during breakup.

A coalescence model is also included in the Reitz model, allowing for the possibility that the parent parcel *could* immediately impact its child parcel after breakup, and a coalescence could occur. This coalescence model uses the same method as the primary collision model used in LISAM, described in Section 2.3.1.2.

2.3.1.1.2 O'Brien Model

The O'Brien model, developed for LISAM, is a modified version of the Reitz model [4]. It uses the same injection and breakup modeling methods with modifications to some steps. In the O'Brien model, the initial location of the child particle after breakup is not assumed to be the same as the parent location, and the parent parcel velocity vector is adjusted after breakup to conserve momentum on a local scale. While these modifications do not constitute a major revision of the Reitz model, they do address some possible sources of error.

In the Reitz model the child parcel is initially given the same location as the parent [4]. This assumes that the child parcel was shed at the beginning of the current timestep, before the parcel position is incremented. But the child parcel could, in

reality, be shed by the parent at any moment during the timestep. To approximate this behavior in the O'Brien model, the initial position of the child parcel is adjusted a small distance from the parent's position at the beginning of the timestep. This distance is some fraction of the distance traveled by the parent parcel during the timestep. A pseudo-random number generator with a uniform deviate is used to select the location along the parent path where the parcel is shed (equation (2.22)).

$$\phi_{\text{child}} = \phi_{\text{parent}} + \left(V_{\phi_{\text{parent}}} \Delta t \right) \cdot \mathcal{R} \quad (2.22)$$

where

$\phi = x, y, \text{ or } z \text{ position [cm]},$

$V_{\phi} = \text{velocity in the } x, y, \text{ or } z \text{ direction [cm/sec]}.$

Another modification made to the Reitz model was to adjust the velocity of the parent parcel after a breakup event to account for the momentum lost to the child parcel. This adjustment is made after the breakup and possible coalescence processes are complete. The change in velocity of the parent parcel is calculated by assuming the parent's original momentum in each coordinate direction is conserved during the breakup process. With this assumption, a new parent velocity can be computed using equation (2.23).

$$V_{\phi_{\text{after}}} = \left(\frac{(m_{\text{parent}} V_{\phi})_{\text{before}} - (m_{\text{child}} V_{\phi_{\text{child}}})}{m_{\text{parent}_{\text{after}}}} \right) \quad (2.23)$$

where ϕ is $x, y, \text{ or } z$.

2.3.1.1.3 Taylor Analogy Model

The Taylor Analogy Breakup (TAB) model was used in KIVA-3 [13] to simulate liquid atomization. The basic principles of the injection method for the Taylor Analogy model are similar to those used in the Reitz model [12]. The primary difference comes in the determination of the initial velocity given to each parcel. In the TAB model, the velocity is determined by the input injection velocity and an input spray cone angle. The magnitude of the total velocity vector is equal to the input velocity. Two pseudo-random numbers are used to evenly distribute the parcels through the spray angle and in a circular spray pattern.

The breakup model used, however, is quite different. The TAB model uses “an analogy by Taylor [17], between an oscillating and distorting droplet and an oscillating spring-mass system.” [7] Surface tension corresponds to the restoring force on the spring-mass system, and gas aerodynamic forces are like the external force on the system [7]. In addition to the ‘forces’ included in the original Taylor analogy, O’Rourke et al. include liquid viscosity which acts as the damping force [7]. The primary drawback to the TAB model is that it can only account for a single mode of oscillation, the fundamental or lowest spherical zonal harmonic, on a drop [7]. This harmonic should be the most influential, because it is the longest-lived oscillation mode [7]. Other modes can be significant, especially for large Weber numbers, but computational limitations restrict the TAB model to a single mode [7].

The equation used to model the droplet distortion, a forced, damped harmonic oscillator, is given in equation (2.24) [7].

$$m\ddot{x} = F - kx - d\dot{x} \quad (2.24)$$

where x is the displacement of the droplet diameter from its equilibrium value at its

equator. Using the Taylor analogy, the terms in equation (2.24) are [7]:

$$\frac{F}{m} = C_F \frac{\rho_g V_{rel}^2}{\rho_{liq} r_{drop}} \quad (2.25a)$$

$$\frac{k}{m} = C_k \frac{\sigma}{\rho_{liq} r_{drop}^3} \quad (2.25b)$$

$$\frac{d}{m} = C_d \frac{\mu_{liq}}{\rho_{liq} r_{drop}^2} \quad (2.25c)$$

where C_F , C_k , and C_d are dimensionless constants defined later in this section. The TAB model assumes there is a critical value of the drop diameter displacement, x_{crit} , above which breakup will occur [7]. This value is taken to be proportional to the drop radius, and breakup only occurs if $x > C_b r_{drop}$, where C_b is a constant of proportionality. The next step in the development of the TAB model is to use this critical value of droplet displacement to nondimensionalize equation (2.24). This results in equation (2.26) [7].

$$\ddot{y} = \frac{C_F}{C_b} \frac{\rho_g}{\rho_{liq}} \frac{V_{rel}^2}{r_{drop}^2} - \frac{C_k \sigma}{\rho_{liq} r_{drop}^3} y - \frac{C_d \mu_{liq}}{\rho_{liq} r_{drop}^2} \dot{y} \quad (2.26)$$

where $y = x/C_b r$. In this form, a droplet would breakup when $y > 1$ [7]. Equation (2.26) is the form of the displacement equation used in both KIVA and LISAM.

If V_{rel} is assumed to be constant, equation (2.26) can be solved for y as a function of time [7].

$$y(t) = \frac{C_F}{C_k C_b} We_g + e^{-t/t_d} \left[\left(y(0) - \frac{C_F}{C_k C_b} We_g \right) \cos(\omega t) + \frac{1}{\omega} \left(\dot{y}(0) - \frac{y(0) - \frac{C_F}{C_k C_b} We_g}{t_d} \right) \sin(\omega t) \right] \quad (2.27)$$

where

$$\dot{y} = \frac{dy}{dt}$$

$$\frac{1}{t_d} = \frac{C_d}{2} \frac{\mu_{liq}}{\rho_{liq} r_{drop}^2}$$

$$\omega^2 = C_k \frac{\sigma}{\rho_{liq} r_{drop}^3} - \frac{1}{t_d^2}$$

The variable t_d is the viscous damping time and ω is the oscillation frequency [12]. The constants, C_F , C_k , and C_d , introduced previously, are given in Reference [7] as $C_k=8$, $C_d=5$, and $C_F=1/3$. Reference 2-8 also gives $C_b=1/2$. These values were determined using both theoretical and experimental results [7].

There are two possible cases for equation (2.27) that must be examined. The first is the case where $\omega^2 \leq 0$. This case only occurs for extremely small particles, therefore the TAB model sets y and \dot{y} equal to zero (since droplet distortion would be negligible), and the next parcel is examined. For the case where $\omega^2 > 0$, y and \dot{y} must be evaluated to determine if breakup will occur. Rather than actually calculate y_p^n (the value of y for parcel p , at time level n) using equation (2.27), the undamped oscillation

amplitude, A, is calculated [12].

$$A^2 = \left(y_p^n - \frac{C_F}{C_k C_b} W e_g \right)^2 + \left(\frac{\dot{y}_p^n}{\omega} \right)^2 \quad (2.28)$$

If the value of this undamped amplitude plus the driving force term add up to a value less than one,

$$A + \frac{C_F W e_g}{C_k C_b} \leq 1,$$

then y_p^n can never be greater than one and the breakup criterion will not be met [12].

If breakup does not occur, a new value for y_p^{n+1} and \dot{y}_p^{n+1} are calculated using equation (2.27) and its time derivative [12]. Written in a finite difference form, the equations for y_p^{n+1} and \dot{y}_p^{n+1} are given as:

$$y_p^{n+1} = \frac{W e_g}{12} + e^{-\Delta t/t_d} \left[\left(y_p^n - \frac{W e_g}{12} \right) \cos(\omega t) + \frac{1}{\omega} \left(\dot{y}_p^n - \frac{y_p^n - \frac{W e_g}{12}}{t_d} \right) \sin(\omega t) \right] \quad (2.29)$$

$$\dot{y}_p^{n+1} = \frac{\left(\frac{W e_g}{12} - y_p^{n+1} \right)}{t_d} + e^{-\Delta t/t_d} \left[\left(\dot{y}_p^n + \frac{y_p^n - \frac{W e_g}{12}}{t_d} \right) \cos(\omega t) - \omega \left(y_p^n - \frac{W e_g}{12} \right) \sin(\omega t) \right] \quad (2.30)$$

Once updated values for y_p^{n+1} and \dot{y}_p^{n+1} have been calculated, the code moves to the next parcel.

If the breakup criterion is met, then a breakup time must be calculated. This time, t_{bu} , assumes that the droplet oscillations for the first period would be undamped [12]. This assumption should hold for all but the smallest drops. The time, t_{bu} , is the “smallest root greater than t^n of the equation” [12]:

$$\frac{C_F}{C_k C_b} We + A \cos[\omega(t - t^n) + \Phi] = 1 \quad (2.31)$$

where

$$\cos(\theta + \phi) = \cos(\theta)\cos(\phi) - \sin(\theta)\sin(\phi)$$

$$\cos(\Phi) = \frac{y_p^n - \frac{C_F}{C_k C_b} We}{A}$$

$$\sin(\Phi) = -\frac{\dot{y}_p^n}{A\omega}$$

If the time t_{bu} is greater than the computational timestep, Δt , there is not enough time available for the breakup process to be completed, so y_p^{n+1} and \dot{y}_p^{n+1} are merely updated (using equations (2.29) and (2.30)) and the code proceeds to the next parcel [12]. If t_{bu} is less than or equal to Δt then breakup will occur and new droplet values must be calculated. New values of the instantaneous drop radius are found by first calculating a new value of Sauter Mean radius, r_{32} , and a post-breakup velocity change (normal to the current path) are calculated [12].

$$r_{32} = \frac{r_p}{\frac{7}{3} + \frac{\rho_{liq} r_p^3}{8\sigma} \dot{y}_p^2} \quad (2.32)$$

$$\Delta V = \frac{1}{2} r_p \dot{y}_p \quad (2.33)$$

The value of \dot{y}_p used in equations (2.32) and (2.33) is calculated at t_{bu} using equation (2.27) [12]. The size of the post-breakup droplets is decided by randomly selecting a radius from a χ -squared distribution using r_{32} [12]:

$$g(r) = \frac{1}{\bar{r}} e^{-\frac{r}{\bar{r}}} \quad (2.34)$$

where

$$\bar{r} = r_{32}/3$$

After the new size has been determined, the number of physical droplets in the parcel must be adjusted to conserve mass using an equation of the form of equation (2.18) [12]. Once the parcel size and velocity has been adjusted, y_p^{n+1} and \dot{y}_p^{n+1} are set to zero and the next parcel is evaluated [12]. It should be noted that unlike the Reitz method described in Section 2.3.1.1.1, the TAB model does not add new parcels to the system, it resizes the physical drop diameters in the original parcel.

2.3.1.1.4 Non-Dimensional Breakup Time Model

The Non-Dimensional Breakup Time (NDBT) model is an empirically modified version of the atomization model presented by Reitz and Diwakar [6]. The injection model presented for the Reitz method (Section 2.3.1.1.1) is used to inject particles into the system for the NDBT method. The atomization model of Reitz and Diwakar uses experimental correlations [6] to predict if and when droplet breakup will occur. The breakup criteria used are:

$$We_g = \frac{\rho_g V_{rel} r_{drop}}{\sigma} > 6.0 \quad \text{Bag Breakup} \quad (2.35a)$$

$$\frac{We_g}{\sqrt{Re_g}} > 0.5 \quad \text{Stripping Breakup} \quad (2.35b)$$

If either of these criteria are met then a droplet has the potential to breakup. As in the TAB model (Section 2.3.1.1.3), a breakup time must be calculated to ensure that the breakup process can be completed during the current timestep. Reitz and Diwakar also give equations for the breakup times for these two modes of droplet breakup.

However, the NDBT uses an experimental correlation of water spray data to give a non-dimensional breakup time [14]. This experimental correlation is in the form of a distribution function based on experimentally determined values for breakup time. The shape of this distribution function is shown in Figure 2-2. A uniform random deviate is used to select a value for the probability function along the ordinate and the corresponding non-dimensional breakup time, from the abscissa, is returned. This non-dimensional time is then multiplied by $(2r_{drop}/V_{drop})$ to give the breakup time, t_{br} , for this drop. If the breakup time is less than Δt then breakup occurs. If breakup criteria are met, the drop size and velocity must be adjusted.

The post-breakup drop size is chosen from a gaussian distribution centered around an average drop size calculated as [18]:

$$r_{drop_{avg}} = 1.81 \left(\frac{\mu_{liq}^{1.5}}{\rho_g \sigma^{0.5}} \right) \left(\frac{\dot{m}_{liq}}{\dot{m}_g} \right)^{0.4} V_{rel}^{-0.5} \quad (2.36)$$

This value is a correlation to experimental water spray data taken at the NASA Lewis Research Center [18], and is only valid for water sprays. With a new drop size

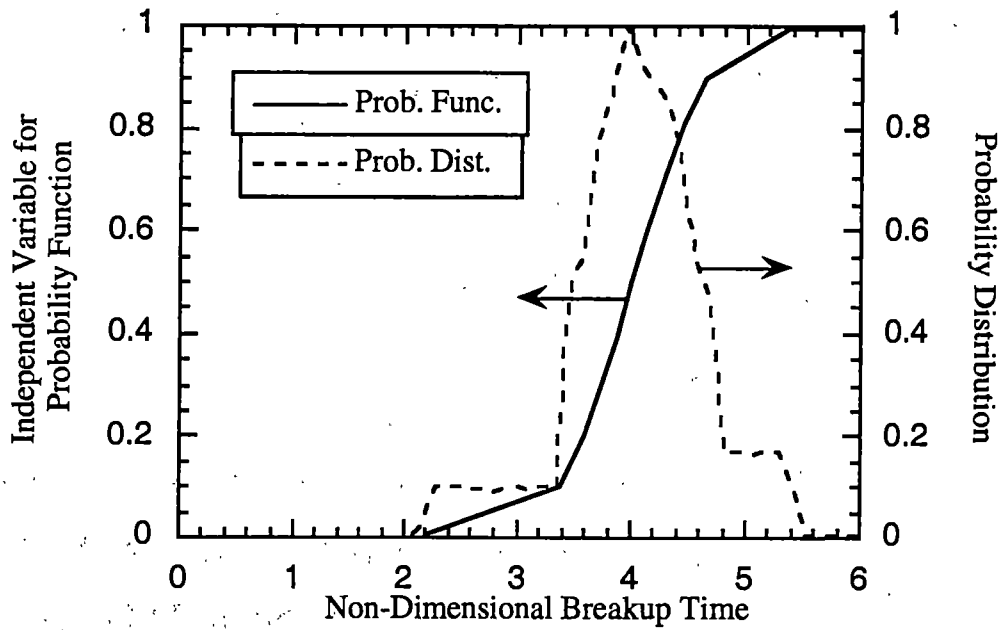


Figure 2-2. Probability Function and Distribution of the Non-Dimensional Breakup Time.

calculated, the number of real particles in the computational parcel must be adjusted to conserve mass. Once the size adjustment is complete, the velocity is adjusted. Just as in the previously discussed models the post-breakup droplet velocity is altered in the direction normal to its current path. The change in velocity for the NDBT model is also chosen from a gaussian distribution, centered on some percentage of the relative liquid/gas velocity [14]. The value currently used is 5% of the relative velocity. This value chosen using numerical experiments to find a reasonable value for velocity change. Just as in the TAB model (Section 2.3.1.1.3) no new liquid parcels are added to the system, the size and the velocity of the original are merely adjusted. Once the calculations for the droplet breakup are complete the code moves to the next parcel.

2.3.1.1.5 Andrews Model

The injection and breakup model described by Andrews [5] takes a different approach to liquid spray modeling. It not only attempts to model individual parcels of liquid, but also tries to simulate the effects a coherent core of fluid would have on liquid injection and breakup [5]. Andrews expands upon the concept presented by Reitz and others [4, 6, 7] that the liquid near the injector, which would represent a core region, can be modeled as a series of liquid fragments with a diameter equal to the nozzle diameter. Andrews presents a different "model of liquid core breakup that assumes a core breakup mechanism in which the dominant surface wavelength continuously increases from the most unstable Taylor wavelength [19] at the nozzle exit to a wavelength of the order of the core diameter at the distance at which the core breaks" [5].

Andrews makes the assumption that the liquid jet will behave as a 'self-

preserving' flow [5]. The theory of 'self-preserving' flow assumes all the features of the fluid motion, except those directly dependent on viscosity and surface tension, will have similar shapes at all times [5]. Any differences in flow features can then be described "by changes in velocity and length scales that are functions of time or position in the flow direction." [5] The primary instability mechanism present in the liquid jet is taken to be a Kelvin-Helmholtz instability [5, 20]. It is assumed that the fastest growing wavelength will be the one that becomes most prominent, and will therefore be the most likely to cause jet breakup [20]. The time before this wavelength actually appears is taken to be N times the e-folding time. The e-folding time is the time it takes the dominant wavelength of a Kelvin-Helmholtz instability to grow by a factor of e, and is given by [5]:

$$\tau_d = \frac{\lambda_d}{2\pi V_{rel}} \cdot \frac{\rho_{liq} + \rho_{gas}}{\sqrt{\rho_{liq}\rho_{gas}}} \quad (2.37)$$

where

τ_d = e-folding time [sec],

λ_d = dominant wavelength [cm].

The time, t_d , at which λ_d appears would be $N\tau_d$ [5], where N is the number of e-folding times before λ_d appears.

Now the criteria for liquid jet breakup must be specified. Andrews assumes the liquid jet core will break when the dominant wavelength reaches a specified fraction of the core diameter, $\lambda_b = \alpha D$. The time for this wavelength to appear, t_b , would then be given as [5]:

$$t_b = \frac{N\alpha D}{2\pi V_{rel}} \cdot \frac{\rho_{liq} + \rho_{gas}}{\sqrt{\rho_{liq}\rho_{gas}}} \quad (2.38)$$

The length of the liquid jet when it breaks would be

$$L_b = t_b V_{wave} = t_b \left(\frac{\rho_{gas} V_{gas} + \rho_{liq} V_{liq}}{\rho_{gas} + \rho_{liq}} \right) = B_c D \left(\frac{\rho_{gas} V_{gas} + \rho_{liq} V_{liq}}{V_{rel} \sqrt{\rho_{gas}\rho_{liq}}} \right) \quad (2.39)$$

where

L_b = liquid jet length when breakup occurs [cm],

V_{wave} = the wave speed of the fastest growing wave [cm/sec],

$B_c = N\alpha/2\pi$,

D = diameter of the jet nozzle [cm].

The values of the empirical constants, N and α , are given as 10 and 2, respectively, by Reid and Youngs [21]. $N=10$ gives an adequate time for the dominant wavelength to appear and $\alpha=2$ gives the possibility of substantial distortion of the liquid jet [5]. These values of N and α give B_c to be 3.18. However, experimental results [22] give a value of 7 for B_c , which would correspond to a value of $N=11$ and $\alpha=4$.

The core is assumed to penetrate into the gas flow at 70% of the liquid injection speed (a value typically seen experimentally) until a steady length is reached [5]. This gives a transient core length of

$$L_{core_{tr}} = 0.7 \cdot V_{inj} \cdot t \quad (2.40)$$

and a steady core length of

$$L_{\text{core}_{ss}} = B_b D \left(\frac{\rho_{\text{gas}} V_{\text{gas}} + \rho_{\text{liq}} V_{\text{liq}}}{V_{\text{rel}} \sqrt{\rho_{\text{gas}} \rho_{\text{liq}}}} \right) \quad (2.41)$$

where B_b is an empirical constant equal to 2.9 [5]. The actual length of the core at any timestep is minimum of the values from equations (2.40) and (2.41).

$$L_{\text{core}} = \min(L_{\text{core}_{tr}}, L_{\text{core}_{ss}}) \quad (2.42)$$

The intact core length, L_b , is taken as the maximum possible length an intact core could achieve. The shape of that intact core is assumed to be a cone, because liquid is being shed along its length as it is injected. The actual core is assumed to take on the shape of a truncated cone [5] (See Figure 2-3).

With the length of the core, L_{core} , calculated and the shape known, the mass contained in the core can be determined. Using geometry to calculate the volume of a truncated cone with its length and the length of the full cone known, the liquid mass in the core can be shown to be:

$$m_{\text{core}} = \rho_{\text{liq}} \frac{\pi D^2}{12} L_{\text{core}} \left(3 - 3 \frac{L_{\text{core}}}{L_b} + \left(\frac{L_{\text{core}}}{L_b} \right)^2 \right) \quad (2.43)$$

When the core is still in the transient period, liquid can be input to the system in two ways. It can be added to the core, or it can be added to the flow as mass that has been ejected from the core. The determining factor on whether any mass is ejected from the core is how much mass should be in the system at the current timestep and is it greater than the amount of mass that should be in the core. If the amount of mass available for injection is greater than that needed to fill the core to the level of m_{core} , then

this excess mass is added to the system as ejected droplets in a new computational parcel [5].

Mass is added to the core by dividing up the core region into sections (see Figure 2-3). The total available core mass is divided among the sections based on the area of each section [5]. The number of drops that are added to any one section is determined using equation (2.2). The mass per computational particle that is used, however, is only 10% of that used in equation (2.2) because the volume of each section is too small to allow injection of the standard parcel size. The droplets are randomly placed inside their respective sections and assigned an axial velocity equal to the input liquid injection velocity and a zero radial velocity [5]. Once all of the mass has been included, a new core mass is calculated and the total mass injected into the system is updated.

Any available excess mass is assumed to be ejected from the core tip [5]. The number of parcels that can be injected is calculated in the same fashion as previously described, except 30% (instead of 10%) of the calculated injected particle mass, is used for the mass per particle. It is placed along the core axis with an axial position randomly chosen from the distance $[0:V_{inj}*\Delta t]$ from the tip of the core.

Once the core has reached a steady state, liquid can be input to the system in three ways: it can be added to the core; it can be added to the flow as mass that has been ejected from the sides of the core; or it can be added as mass included in the broken tip area [5] (See Figure 2.4). The number and size of droplets added to the core region is determined for the steady case in the same manner as the transient case. The amount of mass added to the broken tip region is the amount of mass that would fill the volume of the tip region between the broken and unbroken core (See Figure 2-3), assuming there

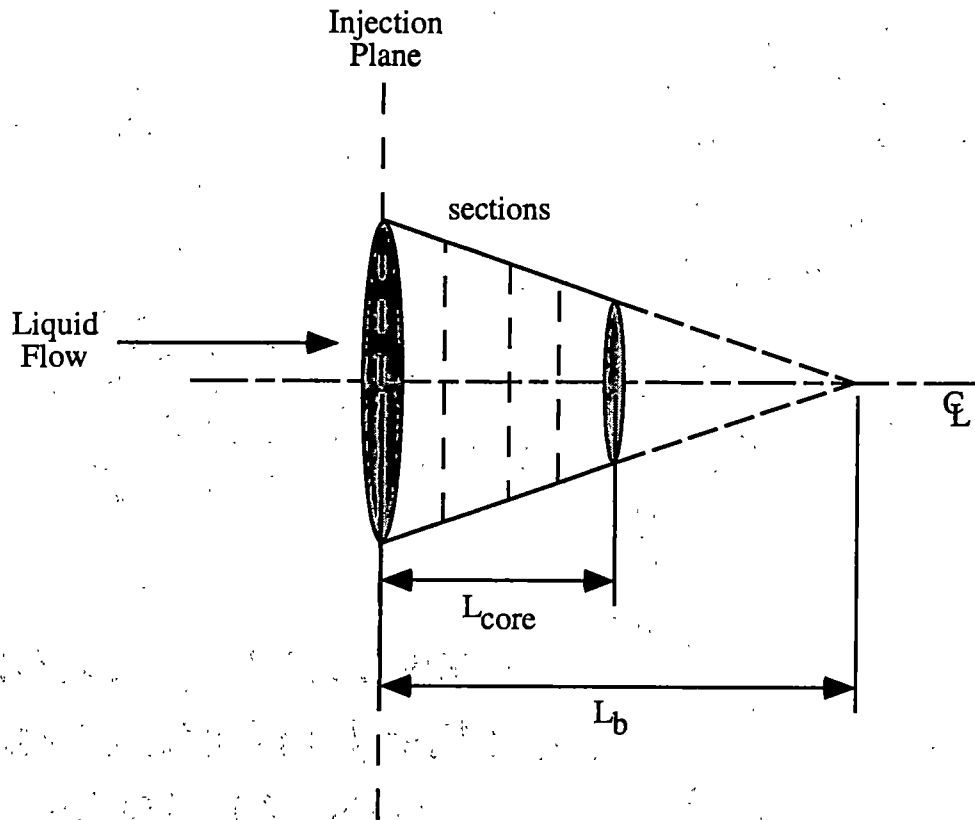


Figure 2-3. Diagram for Andrews Liquid Core Injection Model.

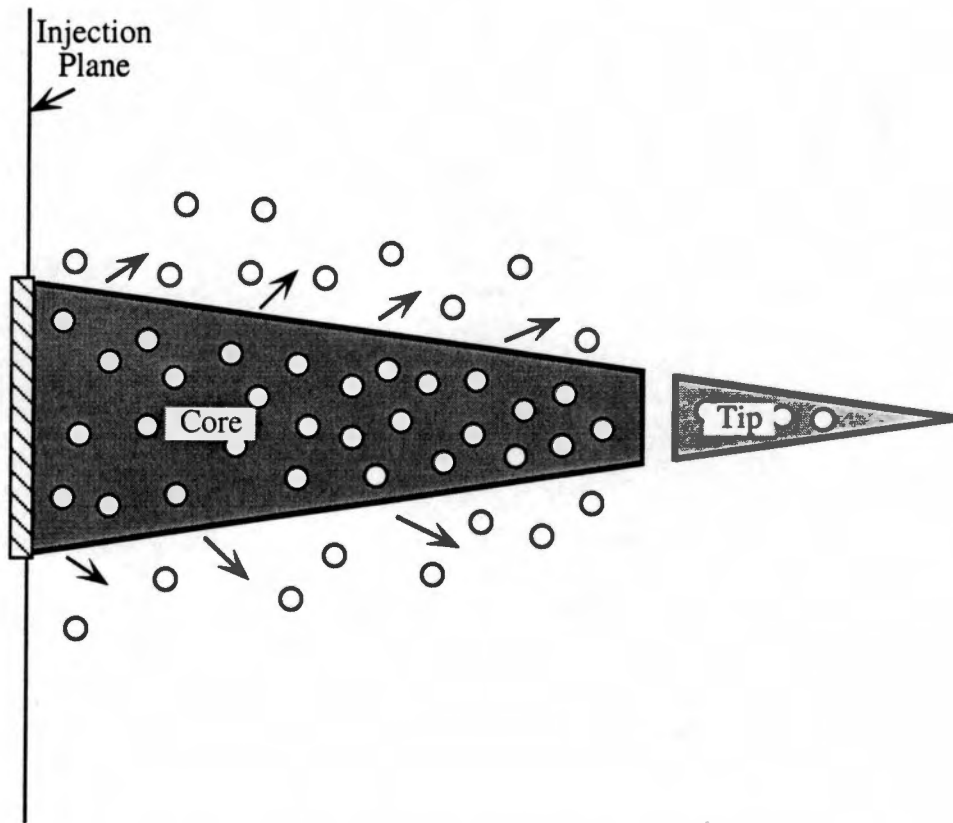


Figure 2-4. Sketch of Steady State Andrews Model Core Behavior.

is enough injected mass available during the timestep [5]. The amount of excess mass ejected from the sides of the core is any available injected mass that has not been placed in the core or tip regions. Liquid placed in the core and tip regions are assigned axial velocities equal to the liquid injection velocity and zero radial velocities. Droplets in the steady tip and core regions are assigned positions in the same manner as in the transient core. Parcels ejected from the sides of the core have a randomly selected axial position using an area weighted distribution [5]. The radial position is taken to be radius of the core at that axial position and the azimuthal angle is chosen randomly. The axial velocity given to these ejected droplets equals the injection velocity and the radial velocity is given as [5]:

$$V_{\text{rad}} = \frac{2\pi}{N} V_{\text{rel}} \sqrt{\frac{\rho_{\text{gas}}}{\rho_{\text{liq}}}} \quad (2.44)$$

With the injection process complete, Andrews uses the Reitz model of droplet breakup [5] (See Section 2.3.1.1.1) with some modification. Andrews takes the slip velocity between liquid and gas to be one half of the relative velocity between the two. Reitz uses the full relative velocity as the slip velocity, but then allows local coalescence immediately after breakup [5]. Andrews uses the factor of 0.5 to account for gas boundary layer effects without having to calculate coalescence during breakup [5].

2.3.1.2 Liquid Collision and Coalescence

A collision model has been incorporated in the LISAM code which uses the same principles as the collision model in KIVA [12]. A probability sampling procedure is used to determine whether droplets undergo a collision, and if so, whether it is a

coalescence or grazing collision. The KIVA collision model assumes that only parcels in the same computational grid cell are close enough to possibly collide [12]. If two parcels are in the same cell then they are evaluated for possible collision. This selection method is grid dependent. A parametric study of other methods for determining possible collisions, other ways of defining a parcel's Sphere of Influence (SoI), was conducted. The most satisfactory approach was found to be a method in which a collision 'cell' is defined to have a width in each coordinate direction 10 times the maximum distance parcel 1 could travel during the timestep ($V_{\phi} * \Delta t$). If the path of parcel 2 passes through parcel 1's SoI during the timestep then a collision is possible. A collision frequency for the drops in parcel 1 (containing larger drops) with drops in parcel 2 (containing smaller drops) is calculated as [12]:

$$v_1 = \frac{N_2}{Vol_{cell}} \pi (r_1 + r_2)^2 |V_1 - V_2| \quad (2.45)$$

where

v_1 = collision frequency of drops in larger radius parcel [particles/sec],

N_2 = number of droplets in parcel 2, the smaller parcel,

r_x = radius of the drops in parcel x [cm],

V_x = magnitude of the velocity of parcel x [cm/sec],

Vol_{cell} = volume of the computational cell containing both parcels [cm³]

x = 1 - parcels with larger drops,

2 - parcels with smaller drops.

A probability distribution is used to predict whether the two sets of particles will undergo a collision event. The most commonly used distribution function for

describing the number of times a rare event, such as collision between two parcels, can occur over a finite interval of space or time is a Poisson distribution [23]. A Poisson distribution is used to determine the probability that parcel 1 has a collision with parcel 2 [12]. The distribution is

$$P_n = e^{-\bar{n}} \frac{\bar{n}^n}{n!} \quad (2.46)$$

where

n = the number of collisions drops in parcel 1 have with drops in parcel 2,

\bar{n} = the mean value of n , $= v\Delta t$.

When there are no collisions, $n=0$, and $P_n=P_0$. This gives P_0 as [12]

$$P_0 = e^{-\bar{n}} \quad (2.47)$$

In LISAM, a random number, \mathcal{R} , is chosen from a uniform deviate (0,1) [12]. If this value is below P_0 , then no collisions are calculated between the two parcels and the code considers the next parcel pair [12]. If \mathcal{R} is greater than P_0 then a collision is assumed to have occurred [12].

If a collision occurs, a second random number, \mathcal{R}_2 , is chosen to determine whether the collision will be a coalescence or grazing collision [12, 4]. The collision impact parameter, b , which characterizes the type of collision that will occur is given by [12]:

$$b = \sqrt{\mathcal{R}_2} (r_1 + r_2) \quad (2.48)$$

A critical value of this impact parameter, b_{cr} , is defined, below which drops will

coalesce. b_{cr} was determined by O'Rourke and Bracco [24], based on experimental drop coalescence results from Brazier-Smith et al. [25], to be:

$$b_{cr} = (r_1 + r_2) \sqrt{\min\left(1, \frac{2.4f(\gamma)}{We_{liq}}\right)} \quad (2.49)$$

where

$$f(\gamma) = \gamma^3 - 2.4\gamma^2 + 2.7\gamma$$

$$\gamma = r_1 / r_2$$

$$We_{liq} = \rho_{liq} |V_1 - V_2| r_2 / \sigma$$

When $b < b_{cr}$, a coalescence collision is assumed to take place. In this case, the value of n , from equation (2.46), gives the number of collisions that occur [12]. n droplets are removed from the smaller parcel and their mass is added to the larger parcel. The size of the drops in the larger parcel and velocity are adjusted [12]. If there are not n droplets in the smaller parcel then the entire smaller parcel is removed from the system and the mass is added to the larger parcel [12].

When $b > b_{cr}$, then a grazing collision is assumed to occur. The velocity of each parcel is adjusted to conserve both linear and angular momentum after an energy transfer between the two parcels during the collision [24]. No other parameters are effected.

2.3.1.3 Gravitational Effects

The effects of gravity on the liquid phase are accounted for by adjusting the parcel velocities, according to:

$$V_{p_\phi} = V_{p_\phi}^{old} + g_\phi \Delta t \quad (2.50)$$

where

ϕ denotes the component direction,

g_ϕ is the gravitational acceleration in the ϕ direction [cm/sec²].

Gravitational acceleration is given in vector form. This allows the chamber to effectively be oriented in space in any manner desired. By giving LISAM a zero gravity vector, the user may chose to neglect gravitational effects on the simulation.

2.3.1.4 Droplet Drag

The drag model used in LISAM is a modified form of the model used in KIVA [12]. The drag law in KIVA represents the drag of an isolated sphere in a gas stream. The aerodynamic drag force per unit mass on a particle is given by [12]:

$$F_{D_\phi} = \frac{3}{8} \frac{\rho_g}{\rho_{liq}} \frac{|\vec{V}_{rel}|}{r_{drop}} C_D V_{rel_\phi} \quad (2.51)$$

where

C_D = drag coefficient,

$|\vec{V}_{rel}| = [(\dot{u}_p - \dot{u}_g)^2 + (\dot{v}_p - \dot{v}_g)^2 + (\dot{w}_p - \dot{w}_g)^2]^{1/2}$, the magnitude of the relative liquid/gas velocity [cm/sec],

$V_{rel_\phi} = V_{p_\phi} - V_{gas_\phi}$, the relative liquid/gas velocity in the coordinate direction ϕ [cm/sec],

where

V_{p_ϕ} = parcel velocity in the ϕ direction [cm/sec],

V_{gas_ϕ} = gas velocity in the ϕ direction of the cell containing the parcel

[cm/sec].

The C_D used in equation (2.51) is an empirical drag coefficient for flow over a sphere in the presence of other spheres (cluster drag) [8], given by

$$C_D = \begin{cases} \frac{24}{Re_{liq}} \left(\vartheta^{-2.65} + \frac{1}{6} Re_{liq}^{2/3} \vartheta^{-1.78} \right) & Re_{liq} < 1000 \\ \max \left\{ \frac{24}{Re_{liq}} \left(\vartheta^{-2.65} + \frac{1}{6} Re_{liq}^{2/3} \vartheta^{-1.78} \right), 0.424 \right\} & Re_{liq} \geq 1000 \end{cases} \quad (2.52)$$

where

$$Re_{liq} = \frac{|V_{rel}| \cdot 2 \cdot r_{drop} \cdot \rho_{gas}}{\mu_{gas}}$$

$$\vartheta \text{ is the void fraction} = \max \left(\frac{Vol_{cell} - \sum_{i=1}^{\text{particles in cell}} \frac{4}{3} \pi \rho_{n_i} r_{p_i}^3}{Vol_{cell}}, 0 \right)$$

This equation for droplet drag coefficient is based on experimental studies of fluidized beds with varying void fractions [26]. Note that as the void fraction goes to unity (a single particle present) the drag coefficient reduces to the standard equation for drag over a sphere [1]. LISAM offers the user an input choice whether to use this 'cluster' drag model or the standard single sphere drag model.

2.3.1.4.1 Velocity Adjustment Due to Drag

The droplet velocity is adjusted using a finite difference form of Newton's Second Law ($F=ma$). If $F=ma$ is solved implicitly an updated value for the parcel velocity can be found. The solution procedure is as follows for each velocity

component.

$$F_{D_\phi} \cdot m_{\text{parcel}} = m_{\text{parcel}} \cdot a_{\text{parcel}}$$

Canceling m_{parcel} and writing a_{parcel} in a finite difference, forward Euler, form gives:

$$F_{D_\phi} = \frac{(V_{p_\phi_{\text{new}}} - V_{p_\phi})}{\Delta t}$$

When the velocity terms are separated from F_D , using equation (2.51) it yields:

$$D_p (V_{\text{gas}_\phi} - V_{p_\phi_{\text{new}}}) = \frac{(V_{p_\phi_{\text{new}}} - V_{p_\phi})}{\Delta t}$$

where

$$D_p = \frac{3}{8} \frac{\rho_g}{\rho_{\text{liq}}} \frac{|\vec{V}_{\text{rel}}|}{r_{\text{drop}}} C_D$$

Solving this equation for $V_{p_\phi_{\text{new}}}$ gives the updated value for the drop velocity component to be [12]:

$$V_{p_\phi_{\text{new}}} = \frac{1}{(1 + D_p \Delta t)} (V_{p_\phi} + (D_p \Delta t) V_{\text{gas}_\phi}) \quad (2.53)$$

The velocity components for all parcels are updated in this manner, the same manner that was used in KIVA [12]. The gas velocity used in equation (2.53) is calculated for each drop based on its location within the computational grid. An inverse volumetric weighting is used to calculate an average value for the gas velocity component based on the eight gas velocity points that define its control volume. Local gas velocities for each drop were calculated so drops would see a smooth velocity profile across a grid cell, rather than an abruptly changing profile of cell based average velocities. This smooth

profile allows more realistic drop motion. It was found in early studies for this work that using cell averaged velocities tended to produce results in which the drops lined up with the gross motion of the flow rather than reflect the variations of gas movement across a cell. Figure 2-5 shows the two-dimensional version of inverse volume weighting, inverse area weighting. The area containing the parcel, bounded by the four velocity components in the direction of interest, is divided into sections based on the parcel location. A weighted average of these four velocities is then calculated by using the fraction of the total area represented by the region opposite to a point as its weighting parameter. The x velocity at the point would be given as:

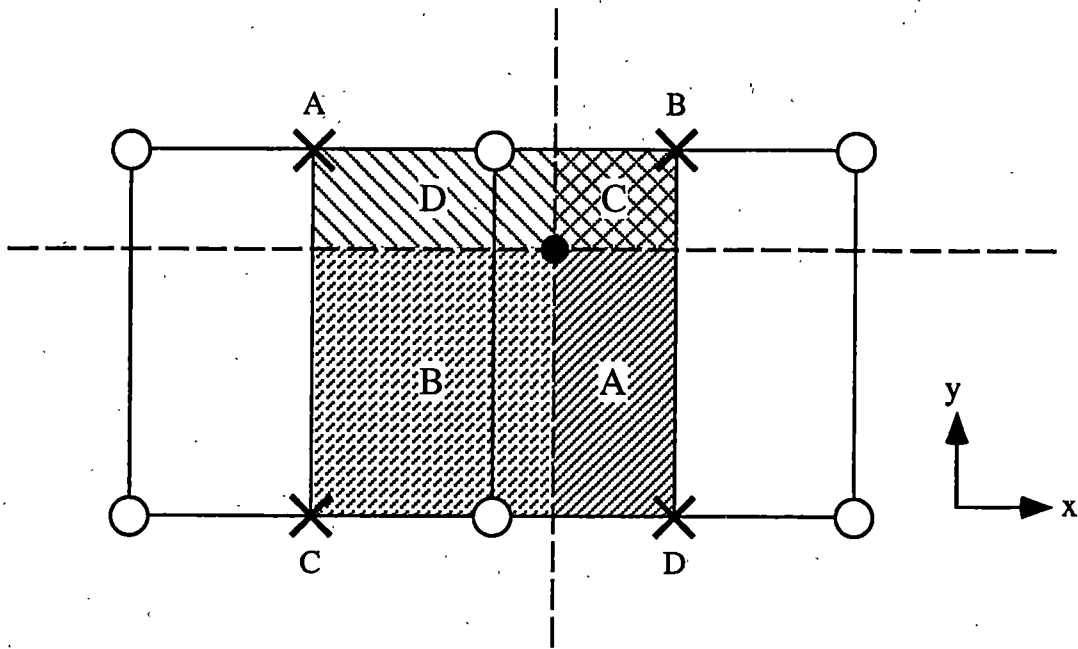
$$V_p = \frac{1}{A_{cell}} (V_A A_A + V_B A_B + V_C A_C + V_D A_D) \quad (2.54)$$

This method is extended into three dimensions by calculating volume fractions instead of area fractions.

After the liquid injection, breakup, collisions and gas interactions are computed, the gas phase is updated to account for the effects of the liquid phase on the gas.

2.3.2 Gas Phase Modeling

In LISAM, the gas flow is solved sequentially (see Figure 2-6). The momentum equation for each velocity component is solved individually (see Section 2.3.2.1); once the changes in velocity for all three components (u,v,w) have been found, their values are updated. Next, the gas density is determined from the continuity equation (see Section 2.3.2.2), and the pressure is obtained from the ideal gas equation. Once the new values of velocity, density and pressure have been computed, the magnitudes of the change in their values since the last timestep are examined. If the change in value of any



○ - Density, pressure, particle momentum points

× - x velocity points

Figure 2-5. Area Weighting of Gas Velocity.

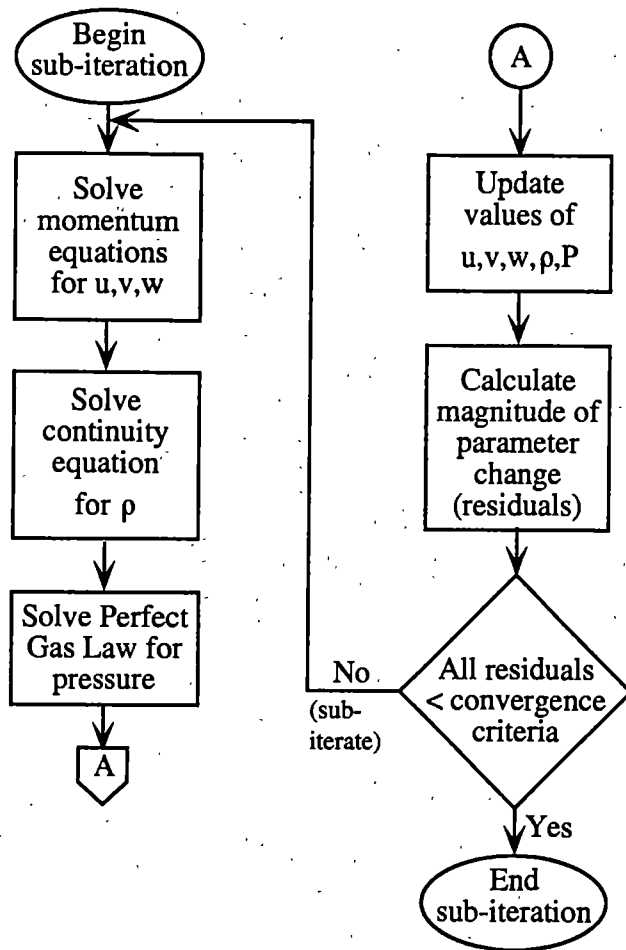


Figure 2-6. Flow Chart for Gas Solver Sub-Iteration Process.

of the parameters during this sub-iteration is higher than the input convergence criterion, then the gas calculations for the current timestep have not reached convergence and another sub-iteration must be performed. Sub-iteration continues until all variables have met the convergence criteria.

In LISAM the gas flow field is discretized using a three dimensional, uniformly spaced, cartesian grid. A staggered mesh system is used [27]. A two dimensional version of such a grid is shown in Figure 2-7. Gas density, pressure, and particle momentum source terms are calculated at the grid "points". The components of gas velocity are calculated midway between adjacent grid points in the direction of the component, the location of the normal face of the control volume for the grid point (See Figure 2-8). This technique of using a 'displaced' grid allows adjacent velocity components to be used in calculating density from the continuity equation, and the pressure at adjacent grid points to be used in the momentum equation. This will prevent physically impossible 'wavy' or 'checkerboard' solutions from being calculated [27]. While using a staggered grid does require frequent interpolations, the elimination of unreasonable solutions offsets the added computational load [27].

The momentum and continuity equations were developed in the delta formulation [11] and an Approximate Factorization method was used to solve them [11]. Sub-iterations and dual timestepping were used to speed convergence and reduce error [11]. A detailed description of these numerical techniques is given in Section 2.3.2.3.

2.3.2.1 Solving the Gas Momentum Equation

As stated previously the gas momentum equation is solved for velocity. The momentum equation that is solved for the velocity components in LISAM is

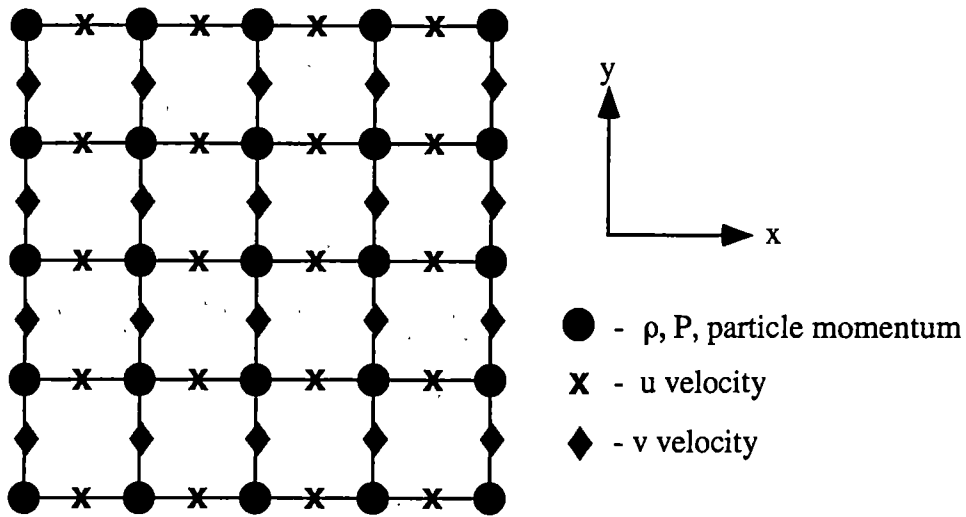


Figure 2-7. Two dimensional Staggered Grid.

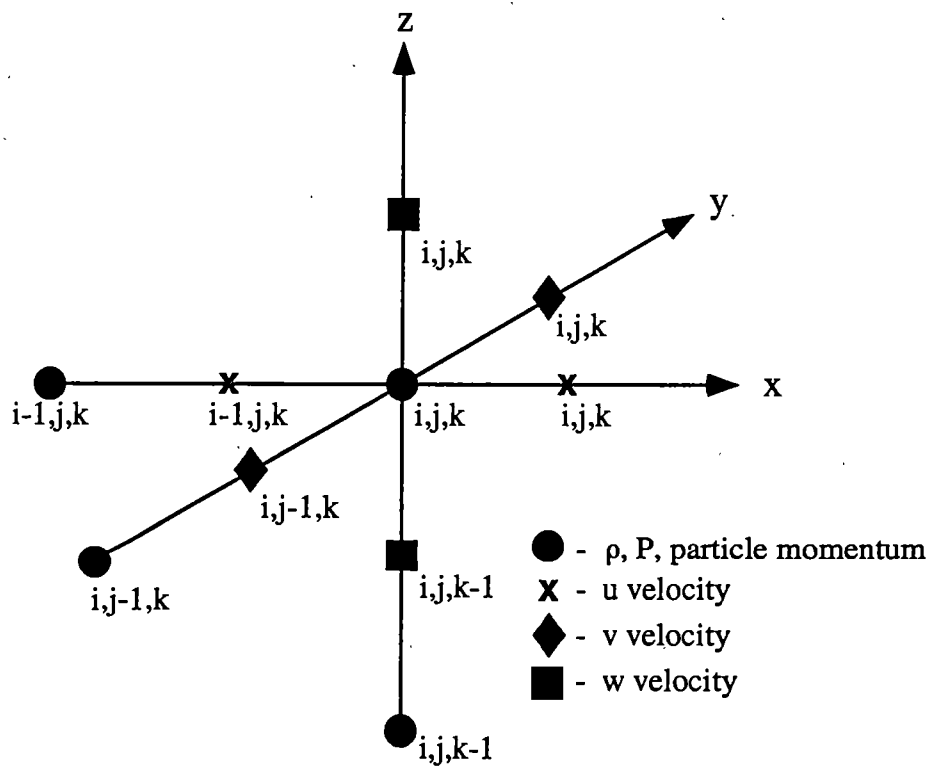


Figure 2-8. Three Dimensional Staggered Grid.

$$\begin{aligned} \frac{\partial V_\phi}{\partial t} + u \frac{\partial V_\phi}{\partial x} + v \frac{\partial V_\phi}{\partial y} + w \frac{\partial V_\phi}{\partial z} = \\ \frac{\mu_{\text{gas}}}{\rho_{\text{gas}}} \left(\frac{\partial^2 V_\phi}{\partial x^2} + \frac{\partial^2 V_\phi}{\partial y^2} + \frac{\partial^2 V_\phi}{\partial z^2} \right) + g_\phi - \frac{1}{\rho_{\text{gas}}} \frac{dP}{d\phi} + S_{\text{drop}_\phi} \end{aligned} \quad (2.55)$$

where

ϕ denotes the coordinate direction, x,y,z; i.e.: $V_x=u$, $V_y=v$, $V_z=w$,

g_ϕ is the gravitational acceleration in the ϕ direction [cm/sec^2],

P is the gas pressure [dynes/cm^2],

S_{drop_ϕ} is the source term, in the ϕ direction, for gas-liquid momentum exchange.

The gas-liquid interaction source term, S_{drop_ϕ} , is defined for each coordinate direction. It is the sum of the change in momentum in that direction (due to drag interactions, see Section 2.3.1.4) for all of the liquid droplets in each cell. These sums are then summed over all cells. The equation for this source term, taken directly from KIVA, is [12]

$$S_{\text{drop}_\phi, ic} = \left[\frac{\rho_{\text{liq}}}{\rho_{\text{gas}, ic} \cdot \text{Vol}_{ic}} \cdot \sum_{n=1}^{\text{\# of particles in cell ic}} W_n \left((\text{Vol}_p V_{p_\phi})_{ic,n}^{\text{new}} - (\text{Vol}_p V_{p_\phi})_{ic,n}^{\text{old}} \right) \right] \quad (2.56)$$

where

W_n is a weighting function,

$\text{Vol}_p = p_n \frac{4\pi}{3} r_{\text{drop}_n}^3$, volume of the drops in parcel n [cm^3].

The weighting function used in equation (2.56) is an inverse volumetric weighting based on each particle's location in the cell. This weighting scheme is similar to the method described in Section 2.3.1.4.1 for calculating local gas velocities based on droplet position.

2.3.2.1.1 Gas Momentum Equation Numerical Methods

To numerically solve the momentum equation for velocity, finite differencing was used. Equation (2.55) was solved implicitly using an Approximate Factorization method in the Delta formulation [11] to yield Equation (2.57) First order temporal differencing was used. The Delta form of the equation is written as:

$$\begin{aligned} \Delta V_{\phi_e} + \Delta t \cdot [F_x(\Delta V_{\phi_{ic}}) + G_y(\Delta V_{\phi_{ic}}) + H_z(\Delta V_{\phi_{ic}})] = \\ - \Delta t \cdot [F_x(V_{\phi_{ic}}^n) + G_y(V_{\phi_{ic}}^n) + H_z(V_{\phi_{ic}}^n)] + \Delta t \cdot g_{\phi} - \frac{\Delta t}{\rho_{g_{ic}}} \frac{dP}{d\phi} + S_{drop_{\phi,ic}} \end{aligned} \quad (2.57)$$

where

$$\begin{aligned} \Delta V_{\phi_e} &= V_{\phi_e}^{n+1} - V_{\phi_e}^n \\ F_x(\chi) &= -\frac{\mu_g}{\rho_g} \frac{\partial^2 \chi}{\partial x^2} + u \frac{\partial \chi}{\partial x} \\ G_y(\chi) &= -\frac{\mu_g}{\rho_g} \frac{\partial^2 \chi}{\partial y^2} + v \frac{\partial \chi}{\partial y} \\ H_z(\chi) &= -\frac{\mu_g}{\rho_g} \frac{\partial^2 \chi}{\partial z^2} + w \frac{\partial \chi}{\partial z} \\ \chi &= \text{dummy variable} \end{aligned}$$

n = last time level

n+1 = current time level

In an Approximate Factorization method, equation (2.57) is written as [11]:

$$\begin{aligned} (1 + \Delta t \cdot F_x(-)) (1 + \Delta t \cdot G_y(-)) (1 + \Delta t \cdot H_z(-)) \Delta V_{\phi_e} = \\ - \Delta t \cdot [F_x(V_{\phi_e}^n) + G_y(V_{\phi_e}^n) + H_z(V_{\phi_e}^n)] + \Delta t \cdot g_{\phi} \\ - \frac{\Delta t}{\rho_{g_{ic}}} \frac{dP}{d\phi} + S_{drop_{\phi,ic}} \quad \text{-(splitting error)} \end{aligned} \quad (2.58)$$

The splitting error introduced by the Approximate Factorization method can be removed by using sub-iterations to reach a converged solution at each timestep [11].

The left hand side of equation (2.57) is discretized using second order central differencing for both first and second derivatives. Details of this process are given in Appendix B. This allows a tridiagonal matrix solver to be used to solve for the change in velocity. The terms on the right hand side of the equation can be calculated from known values from the previous timestep. The derivative values can be calculated in two different manners. For the first derivatives a choice of first order accurate upwind differencing using a two point stencil or second order central differencing with a three point stencil is available. For the second derivatives second order central differencing (three point stencil) is used.

Equation (2.57) is solved sequentially for the change in each velocity component. Once all of the velocity component changes have been determined, the values of the gas phase velocities are updated using equation (2.59).

$$V_{\phi_{ic}}^{n+1} = V_{\phi_{ic}}^n + \Delta V_{\phi_{ic}} \quad (2.59)$$

Once new values for velocity have been calculated, new densities can be determined from the continuity equation.

2.3.2.1.2 Momentum Equation Boundary Conditions

The gas phase velocity boundary conditions used are: no-slip ($\vec{V}=0$) for all solid walls; constant velocity (equal to input gas injection velocity) for the gas velocity on the inflow boundary, and zero-slope ($dV/dx=0$) on the gas velocity at the outflow boundary.

2.3.2.2 Solving the Gas Continuity Equation

The continuity equation solved in LISAM is:

$$\frac{\partial \rho}{\partial t} + \nabla \cdot (\rho \bar{V}) = 0 \quad (2.60)$$

Much like the momentum equation, the continuity equation is written in the delta formulation, and an Approximate Factorization method is used to solve for the new values of density. The finite difference form of equation (2.60) is written as [11]:

$$\begin{aligned} \Delta \rho + \Delta \rho \left(\frac{\partial u^{n+1}}{\partial x} + \frac{\partial v^{n+1}}{\partial y} + \frac{\partial w^{n+1}}{\partial z} \right) \\ + \Delta t \left[u^{n+1} \frac{\partial (\Delta \rho)}{\partial x} + v^{n+1} \frac{\partial (\Delta \rho)}{\partial y} + w^{n+1} \frac{\partial (\Delta \rho)}{\partial z} \right] = -\Delta t \cdot R(\rho^n) \end{aligned} \quad (2.61)$$

where

$$R(\rho^n) = \left[\rho^n \left(\frac{\partial u^{n+1}}{\partial x} + \frac{\partial v^{n+1}}{\partial y} + \frac{\partial w^{n+1}}{\partial z} \right) + \bar{u}^{n+1} \frac{\partial \rho^n}{\partial x} + \bar{v}^{n+1} \frac{\partial \rho^n}{\partial y} + \bar{w}^{n+1} \frac{\partial \rho^n}{\partial z} \right]$$

The left hand side of equation (2.61) is discretized using second order central differencing to allow a tridiagonal matrix solver to be used. Second order, three point, central differencing was used to discretize the right hand side.

2.3.2.2.1 Continuity Equation Boundary Conditions

A constant density boundary condition, consistent with the no-slip boundary condition in the momentum equation, equal to the initial value, was assumed at all solid boundaries. Input density was held constant at the inflow boundary, and a zero slope was assumed at the outflow boundary. Other density boundary conditions were explored during this work. A zero slope condition on all boundaries was tried at

different times and at the same time, having the effect of allowing the density field to 'float' and have no ties to any base value. The final set of conditions used (those first described) were found to be the simplest, most stable and most physically reasonable set of boundary conditions for the situations modeled in this study.

2.3.2.2.2 Solving for Gas Pressure

Pressure is then solved using the ideal gas equation.

$$P_{ic} = \rho_{ic}RT \quad (2.62)$$

where

R = gas constant [erg/g-K] (input)

T = gas temperature [K] (input)

2.3.2.3 Dual Timestepping

Dual timestepping is a numerical technique used to reduce the splitting errors, and increase the speed of convergence [11]. Dual timestepping adds an additional derivative term using an intermediate time level, which goes to zero at convergence. This extra time derivative, which has no physical significance and does not effect the time accuracy of the solution, can be adjusted to give a more rapid, yet still stable, convergence [11]. The general form of a finite difference equation with dual timestepping is:

$$\frac{\Delta q^*}{\Delta \tau} + \frac{q^{n+1} - q^n}{\Delta t} + F_x(q^{n+1}) + G_y(q^{n+1}) + H_z(q^{n+1}) = 0 \quad (2.63)$$

where

Δq^* is $q^{k+1} - q^k$ (where k is an intermediate time level, $n < k < k+1 < n+1$)

$\Delta \tau$ is the 'dual' timestep (input) [sec].

When a sub-iterative approach is used, each sub-iteration advances the solution from time k to time $k+1$ ($n < k < k+1 < n+1$). When the solution converges, k equals $k+1$, and the $k+1$ value is equal to the value at the new timestep, $n+1$. Therefore, when the solution converges Δq^* goes to zero. Therefore, the addition of the 'dual' timestep has no effect on the final value of the converged solution at that timestep.

The Delta formulation with dual timestepping will have the form:

$$\left[\left(1 + \frac{\Delta t}{\Delta \tau} \right) + \Delta t \cdot F_x(_) + \Delta t \cdot G_y(_) + \Delta t \cdot H_z(_) \right] \Delta q^* = -\Delta q^{kn} - \Delta t \cdot [F_x(q^k) + G_y(q^k) + H_z(q^k)] \quad (2.64)$$

where

$\Delta q^{kn} = q^k - q^n$ (due to sub-iterations).

The addition of the dual timestepping term alters the form of the equation and affects the Approximate Factorization (AF) method introduced previously. The Delta formulation no longer has the form $(1+A+B+C)$, instead it is $(\kappa+A+B+C)$. The AF form for the new equation is

$$[\kappa + A + B + C] = (\alpha + \beta A)(\alpha + \beta B)(\alpha + \beta C) - \underbrace{\frac{1}{\kappa} (AB + BC + AC + \frac{1}{\kappa} ABC)}_{\text{splitting error}} \quad (2.65)$$

where

$$\kappa = 1 + \frac{\Delta t}{\Delta \tau}$$

$$\alpha = \kappa^{1/3}$$

$$\beta = \kappa^{-2/3}$$

When $\Delta\tau$ goes to infinity, κ goes to 1, and the dual timestepping method reduces to a standard sub-iterative method. Because κ will always be greater than 1, the term $1/\kappa$ which multiplies the splitting error serves to reduce the value of that error for each sub-iteration versus that seen with no dual timestepping.

2.3.3 Particle Mover

Once the gas field has been updated, the particles are moved to their new position for the start of the next time step, using the same method as employed by KIVA [12]. The computational parcels are assumed to move in a straight line along the direction of their total velocity vector between timesteps. The equation used to update their position is

$$\phi_p = \phi_p^{\text{old}} + V_{\phi_p} \Delta t \quad (2.66)$$

where

ϕ_p is one component of the parcel position (x_p , y_p , or z_p) [cm],

V_{ϕ_p} is the parcel's velocity component in the ϕ_p direction [cm/sec] as calculated

in Section 2.3.1.4.1, based on gas velocities from the previous timestep.

Once the new particle positions have been calculated, selected output is written and the computational time is updated. If the new time is less than the input maximum time then

a new iteration begins. If the new time is greater than or equal to the input maximum time the code stops and final output is written.

2.4 LISAM Summary

The LISAM computer program models a three dimensional, transient, two-phase liquid/gas injection problem. Physical dimensions of the injection chamber and nozzle can be altered, and the physical properties of both the liquid and gas can be changed to simulate different media. A variety of liquid injection/breakup models are incorporated into LISAM and are available to address various types of liquid injection problems. Droplet collision/coalescence can also be modeled. An Approximate Factorization (AF) method, using sub-iterations and dual timestepping, is used to solve the momentum equation for velocities and the continuity equation for density. Pressure is found using the perfect gas law, with temperature held constant.

Chapter 3

Spray Characterization and LISAM Data Analysis Techniques

3.1 Introduction

Liquid spray experiments are conducted, and computational simulations are performed, to evaluate the performance of a liquid injection system. In order to objectively assess the effect of changes to an injector setup, spray characteristics that adequately describe the behavior and performance of a system must be defined. Characteristics typically of interest in combustion applications include: mean drop sizes, drop size distributions, spray patternation, and spray penetration rates [28]. These characteristics can, with varying degrees of success, be measured experimentally. Computer simulations can also be used to predict these basic flow characteristics. Computational models have the added advantage of also being able to predict other flow properties, such as gas velocity vectors, gas pressure distributions, drop size distribution in the interior of the spray, etc.; values which can not be readily measured experimentally.

Whether data is gathered experimentally or calculated by computer simulation, it is important to know how values are determined and how error is accounted for, in order to understand how the spray is characterized.

3.2 Experimental Techniques

There are certain basic requirements for any experimental spray measurement technique: be able to measure drop sizes without disturbing the spray, be able to detect a

wide range of drop sizes, make measurements quickly, and be able to handle a large sample count [1]. It can be quite difficult to meet all of these requirements at once and still make accurate measurements. The difficulty in making accurate measurements arises from the large number of drops that must be measured, the intermittent nature of many spray processes, and the very nature of the liquid itself [29]. The high, variable drop velocities that are seen, the wide range of sizes that must be measured, and the changes in drop size due to evaporation and coalescence, over time, also make it very difficult to obtain accurate spray measurements [1]. There are three categories of experimental methods for measuring spray characteristics: mechanical, electrical, and optical [1]. Each method has advantages and disadvantages. Each technique offers some method of measuring drop sizes and many offer ways of measuring spray densities and drop velocities.

Mechanical systems (such as collecting drops on slides or in suspension cells, molten wax techniques, and drop freezing) are relatively simple [1], but suffer from limitations. Limitations and problems include: restrictions on the types of fluids that can be tested (molten wax, suspension cells); corrections for disturbance by the measurement device, such as flattening on slides, drop shattering on impact with collection cells; droplet overlap on slides; and corrections for size changes due to freezing can be required [1]. In general, mechanical methods can provide a general description of drop sizes in the measurement plane, but cannot provide a time history of drop sizes or an axially resolved distribution of drop sizes [1].

Electrical systems (such as Wicks-Dukler technique, charged wire, and hot wire techniques [1]) require intrusive measurements, although often with minimal disturbance. The primary disadvantage to electrical techniques is that the measurement instrument can cause large drops to shatter because of high velocity impact on the

device, so these techniques cannot be used in high speed flows. In charged wire measurements, low conductivity liquids create long electrical pulses, which can lead to impingement overlap (signals from more than one drop being sent at the same time); therefore this technique is limited to dilute, high-conductivity sprays [1]. Electrical techniques are also limited to fluids which do not deposit residue on the wires or needles. The Wicks-Dukler technique, which uses two sharp needles to measure the change in electric potential when a drop passes between them, cannot distinguish between changes due to variations in drop size or drop velocity. The signal-to-noise ratio for these devices can also be low, so that signals from small drop measurements are often lost in noise [1]. These techniques can provide a radial profile of drop sizes, and a temporal history of drop sizes, but are limited in the fluids which can be tested and also to relatively dilute sprays [1].

Optical measurement techniques offer the most advanced and accurate measurement methods available today [1]. These techniques include: high speed photography, holography, single-particle counters, Malvern particle sizers, and other interference and diffraction methods [1]. All of these techniques are non-intrusive and can provide a high level of measurement accuracy. They are, however, limited to fairly dilute sprays, and require careful alignment and calibration for reliable results [1]. Imaging techniques, such as photography and holography, require a great deal of human involvement, which introduces the risk of human error [1]. Even when image analyzer software is utilized, human interaction is still required [1]. Non-imaging techniques are susceptible to multiple scatter (light hitting more than one drop prior to detection), vignetting (scattered light measured from drops too far from the detector), and beam steering (refraction of the laser beam due to thermal gradients) [1]. These techniques are also limited by beam extinction (how deeply into the spray light can

penetrate) which is a function of the number density of the spray.

In general, experimental techniques can only provide drop size and velocity measurements for a small, dilute region of a spray. To study other variables of interest, such as gas pressure distributions, and spray behavior in the dense core region, and to study the overall development process of a liquid spray, computational methods must be used.

3.3 Spray Characterization

Computer simulations often use experimentally obtained data to make comparisons and for validation. Since most experimental data sets consist of mean drop sizes, drop velocities and spray tip penetration rate, these quantities are usually calculated in numerical simulations. Additionally, because any of the variables used in a computer program is available for study, many other flow characteristics can also be predicted and analyzed. The effect of a liquid spray on the surrounding gas can be observed. Also, computer simulation allows the temporal development of the spray, and the gas/spray interaction, to be studied. The primary variables of interest are still, however, the size of the spray droplets and their trajectories. A simulation can provide both a spatially and a temporally resolved distribution of drop sizes and velocities.

3.3.1 Drop Size Measurements

Typically, spray drop sizes are measured at discrete points in space to create a local droplet size distribution. From this size distribution, mean drop sizes can be calculated both at a particular point in space over time, and over a region of space and

over a period of time. These mean values allow a spray's general behavior for a period of time and through a region of space to be described. The same averaging process can be used to define mean drop sizes, both spatially and temporally, in the computational domain of a liquid spray simulation. The mean size used in this work is the Sauter mean diameter (SMD), also denoted as D_{32} . The Sauter mean diameter is often used as a representative quantity in combustion processes, because the surface area and volume of fuel drops are extremely significant in evaporation and combustion processes [29]. Also, only the SMD can provide a measure of the "fineness", or atomization quality of a spray [1]. The Sauter mean diameter is defined as the "diameter of the drop whose ratio of volume to surface area is the same as that of the entire spray" [1]. The Sauter mean diameter is calculated using Equation (3.1) [1].

$$D_{32} = \frac{\sum_i N_i D_i^3}{\sum_i N_i D_i^2} \quad (3.1)$$

where

D_{32} = Sauter mean diameter [cm],

i = a given range of drop diameters,

N_i = number of drops in the range i , and

D_i = is the middle diameter of the range i [cm].

In the LISAM computational model, SMD's are calculated at various axial and transverse locations throughout the spray by counting all parcels that pass through a given volume. By storing the accumulated value of the total volume and area of all drops in all parcels that have passed through the volume, a time-averaged SMD is calculated.

$$D_{32_{comp}} = \frac{\sum_{k=1}^t \left(\sum_{i=1}^{N_k} (p_{n_i} D_i^3) \right)}{\sum_{k=1}^t \left(\sum_{i=1}^{N_k} (p_{n_i} D_i^2) \right)} \quad (3.2)$$

where

k = a given time level ($k \leq t$),

t = the current time level,

i = a parcel which passed through the volume of interest during time level k ,

N_k = number of parcels which passed through the volume of interest during time level k .

D_i = the diameter of drops in parcel i [cm].

A second mean drop diameter that can be used to characterize a liquid spray is the Mean Volumetric Diameter (D_{mv}) or D_{30} [1]. This value provides the diameter of a drop whose volume would be equal to the average drop volume in the spray.

$$D_{30} = \left(\frac{\sum_i N_i D_i^3}{\sum_i N_i} \right)^{1/3} \quad (3.3)$$

An additional mean diameter that is sometimes used is the Mean Length Diameter or D_{10} [1]. This value is the average of all of the drop diameters with no other weighting.

$$D_{10} = \frac{\sum_i N_i D_i}{\sum_i N_i} \quad (3.4)$$

3.3.2 Spray Penetration Rate

Another parameter of interest in many combustion processes is the rate at which the liquid spray penetrates the gas. Over-penetration of the spray could lead to wall impingement of fuel, where it would not properly combust, make soot, and would be wasted [1]. If the spray does not penetrate far enough into the combustion chamber, there may not be adequate liquid/gas mixing for optimum combustion [1].

Experimentally, the penetration rate is measured using high-speed photography to image the spray, and then taking spray tip position measurements from the photo images.

Because the location of the spray tip cannot be precisely defined, there is always error associated with these measurements [6]. Similarly, the location of the spray tip in a computational model can be defined in many ways [4, 6, 7, 30]. Some researchers take a cutoff percentage of the maximum drop velocity to be the tip location [6, 30], while others take the axial position behind which a certain percentage of the total liquid mass is located [7]. Reitz [4] simply defines the spray tip to be the location of the computational parcel farthest downstream, and this definition was initially used in the LISAM model.

While comparisons between experimental and computational tip penetration rates are of interest, it is well known that spray tip penetration is relatively insensitive to variation in modeling parameters of the liquid spray [6, 7], particularly those affecting the gas interactions, and the correlation, good or poor, between experimental and computational results should not be used to judge the performance of a computational model [7].

3.3.3 Particle Locations and Distributions

The position and size distribution of the liquid drops, and the spatial concentrations of the liquid mass fractions in the spray called the spray patternations, are also of interest. The development of areas of either low or high fuel concentrations during a combustion process can lead to undesirable increases in pollutants and areas of increased temperature [28]. The distribution of drop sizes is of great interest, because it is the small drops that vaporize and facilitate the ignition and combustion processes. For many liquid sprays, the outer edges of the spray will be populated with small droplets, while the interior regions will contain large drops [31]. In other sprays, the opposite is true, which makes nozzle characterization, not presently incorporated in LISAM, extremely important. Nozzle characterization can provide a dominant influence on the resulting spray characteristics and droplet parameters, in many sprays of practical interest. Nozzle characterization, as an input parameter, is therefore an important area of future work for improving LISAM, but is beyond the scope of the present study.

3.3.4 Flow Field Quantities

Both gas and droplet velocity vector fields are predicted to study the effects of gas/spray interactions. The effects of recirculation on the spray evolution in the test region can be studied. Gas pressure distributions provide additional insight into the gas/liquid interactions.

3.4 Evaluating Simulation Results

In the next chapter, results from the LISAM simulation will be compared to the results of comparable calculations by other authors, as well as to experimental data obtained from the literature. An analysis for LISAM's performance will be made using the spray characteristics described in this chapter and comparing them to reported simulation and experimental results.

Chapter 4

LISAM Simulation Results and Comparisons

4.1 Introduction

This chapter will provide a detailed description of computational studies performed using the LISAM computer program. Parametric studies, as well as comparisons with experimental data, were performed. It is of great importance that a well designed set of cases be chosen to characterize and assess the performance of a computer program used to model real world systems. It is accepted that there will be some deviation from reality and a reliable method of quantifying this deviation allows the code to be used with confidence. It is also important to have reliable experimental data for use in assessing the performance of the computer code, to know how it was obtained and any anomalies involved in the recording or presentation of the data.

The data used for comparison with the LISAM code includes water spray data taken by the NASA Lewis Research Center [18], and tetradecane spray data taken by Hiroyasu and Kadota [29], which is a classic data set used in diesel fuel computations. In addition, comparisons are also made with computational data obtained using KIVA by Reitz [4]. This allows LISAM's performance to be compared to another spray modeling code.

4.2 Experimental Data

Results from experiments using two different liquid/gas combinations were used. Steady-state coaxial liquid water and jet air results from the NASA Lewis Research Center [18] and the transient tetradecane liquid jet into nitrogen results from

Hiroyasu and Kadota [29] were used. The water/air spray data was selected for comparison because it matches conditions that LISAM was designed to simulate, and it also provided detailed information on drop sizes and velocities. Other experimental data of water sprays typically modeled more complex situations (i.e. cross-flow, swirl injectors), or did not offer detailed quantitative results for comparison. The transient tetradecane liquid jet injection experimental data was chosen because it is the standard data used in the literature for comparison of experimental results in diesel fuel type atomization modeling. The injector configurations for the experiments are given in Table 4-1. A sketch of the experimental configurations is given in Figure 4-1. Figure 4-1(a) refers to the coaxial air/water experiments [18], and figure 4-1(b) refers to the tetradecane experiments [29].

4.2.1 Water Spray Data

The water spray data used were obtained using an unconfined single coaxial injector, sprayed into ambient air. The water was injected as a liquid core with an annular air jet surrounding it, with dimensions given in Table 4-1. Liquid and gas velocities were varied, as shown in Table 4-2. Zaller reports that the water flow rate uncertainty was $\pm 2\%$, and the air flow rate uncertainty was $\pm 5\%$ [18]. Drop size and one component of drop velocity were simultaneously measured using a phase/Doppler interferometer (PDI). The PDI was calibrated so that variation in measurements made of two different monodisperse drop streams were within $\pm 2\%$ [18]. The experimental setup allowed for measuring drop sizes in the range of 2-230 μm [18]. Drop velocities from 0-250 m/sec could be measured. Sample sizes were increased in the experiments until the standard deviation of mean measured drop size no longer changed. A sample

Table 4-1. Configurations for Experimental Studies.

	Water/air	Diesel fuel /nitrogen
Liquid nozzle diameter [cm]	0.132	0.03
Post thickness [cm]	0.093	none
Gas nozzle diameter [cm]	0.556	none
Liquid injection velocity [cm/sec]	234.4-732.6	10200.0
Gas injection velocity [cm/sec]	14161.7-28854.0	0.0
Liquid density [g/cm ³]	0.9974	0.77
Liquid viscosity [dynes-sec/cm ²]	0.008966	0.01925
Liquid Reynold's number	3442-10757	12240
Gas density [g/cm ³]	0.0011667	0.0122564
Gas viscosity [dynes-sec/cm ²]	1.811e-4	1.77268e-4
Gas (annulus) Reynold's number	10857-22121	none
Reference	4-1	4-2

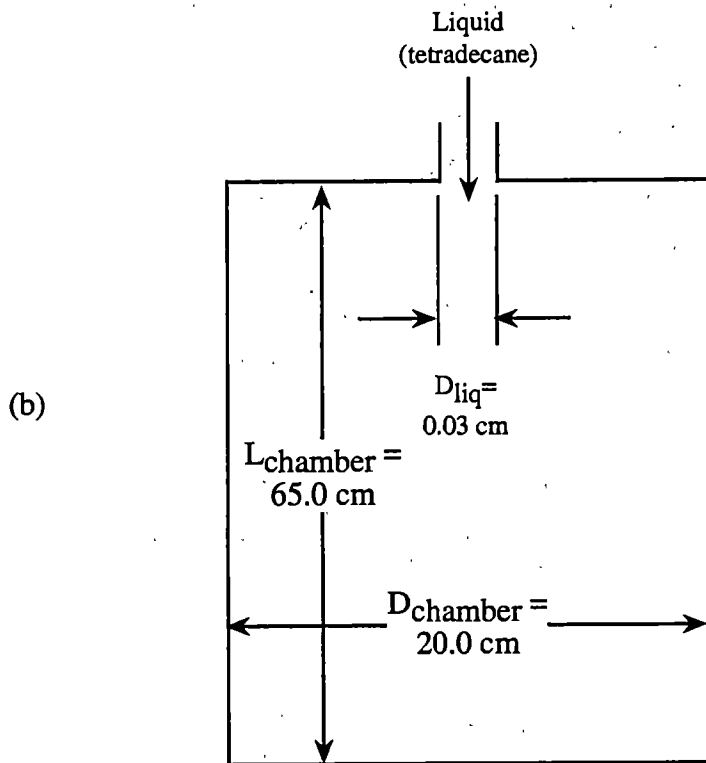
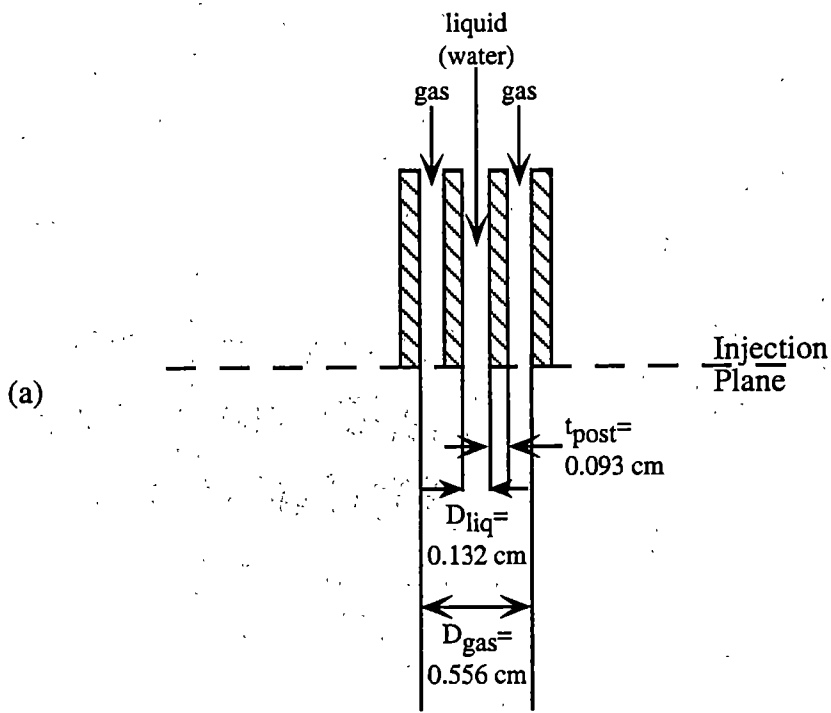


Figure 4-1. Diagrams of Experimental Configurations.

Table 4-2. Water/Air Injection Experiments Modeled using LISAM.

Case Designation	Liquid (water) injection data		Gas (air) injection data	
	[g/sec]	[cm/sec]	[g/sec]	[cm/sec]
	w1	3.2	234.4	2.7
w2	3.2	234.4	4.1	21509.4
w3	3.2	234.4	5.5	28854.0
w4	5.0	366.3	4.1	21509.4
w5	7.3	534.8	2.7	14164.7
w6	7.3	534.8	4.1	21509.4
w7	7.3	534.8	5.5	28854.0
w8	10.0	732.6	4.1	21509.4

size of 6000 valid drops, per sample location, was used [18]. Drop size and velocity measurements were made at 5.08 cm (2 in) downstream of the injector. Results were taken along four different radii to ensure axial symmetry. Variation in results between tests were attributed to experimental repeatability [18]. The repeatability was found to be affected by the photomultiplier tube (PMT) gain [18]. Drop sizes decreased as PMT gain increased. No correlation to an “appropriate” gain value was found and the gain was selected to provide a maximum valid data rate [18]. Results from these experiments are shown in comparison with results from LISAM in a following section.

4.2.2 Diesel Spray Data

The Hiroyasu and Kadota experiment [29] was of a transient high pressure diesel spray. Because of visibility and access limitations in making measurements inside of a pressure vessel, the available measurement techniques were limited [29]. The liquid immersion method [1] was chosen because of its minimal equipment needs. Because of this measurement technique, the data available are more limited [29]. An average drop size at one location and the rate at which the spray penetrated the gas were all that was provided. A circular orifice nozzle, pointed down, was positioned at the top of the pressure vessel. The immersion liquid was positioned 6.5 cm downstream of the injection. The position of the immersion fluid is important to insure that the spray velocity is sufficiently low so that large drops do not shatter when they contact the immersion cell and that small drops are not entrained in the air flow around the cell [29]. A photograph of the illuminated immersion cell was taken for analysis. Images at 100x magnification were analyzed. Drop sizes were correlated in 10 μm intervals, the results plotted on a histogram and a characteristic size then calculated [29]. At least 3000 valid

drop counts were required for a valid measurement [29]. Results from this experiment are compared with LISAM results later in this chapter.

4.3 Computational Studies

A well chosen set of parametric studies can reveal both the strengths and the limitations of a computer model. For the LISAM code, parametric studies were run on a wide range of computational parameters. The complete list of parametric studies is given in Table 4-3. Studies were run to determine: maximum reasonable primary timestep and dual timestep; sensitivity of computational results to grid spacing; sensitivity of computational results to overall grid dimensions; sensitivity of computational results to rate of computational particle injection; results of using different atomization models; effects of variation of atomization modeling constants on computed results; and the impact of convergence criteria on computed results. Also, the effects of physical sub-models were studied: both collision (or drop coalescence) modeling and gravity were evaluated. The different grids used in these studies are shown in Table 4-4.

4.3.1 Results of Parametric Studies

There are several methods for quantifying differences between computational results. To see the effects of changes on the computational models, the most convenient quantities to study are Sauter mean diameter (SMD) distributions, spray penetration rates, and also the spray pattern itself. The parametric studies carried out in this work show that SMD results are most greatly effected by changes to the atomization model, or

Table 4-3. Lisam Parametric Studies Using Tetradecane/Nitrogen.

Parameter	Baseline	Variation		
Atomization model	Reitz	Andrews, O'Brien, TAB, NDBT		
Atomization constant, B_1	$B_1=20$	$B_1=5, 10, 50$		
Computational particle injection rate, P_{inj} , [part/sec]	$P_{inj}=10^5$	$P_{inj}=10^4, 10^6, 10^7$		
Grid spacing, [cm]	$\Delta x=0.05$ $\Delta y=0.05$ $\Delta z=0.5$	Δx	Δy	Δz
		0.1	0.1	0.5
		0.025	0.025	0.25
		0.05	0.05	0.25
		0.025	0.025	0.5
Grid dimensions [cm]	$R=0.5$ $L=10.0$	$R=0.5, L=5.0$ $R=1.0, L=10.0$		
Primary timestep, [sec]	$\Delta t=10^{-6}$	$\Delta t=5 \times 10^{-6}, 10^{-7}$		
Dual timestep	$\Delta \tau=10^{-6}$	$\Delta \tau=10^{-7}$		
Convergence criteria	$V_{err}=10^{-4}$ $\rho_{err}=10^{-2}$	$V_{err}=10^{-9}$ $\rho_{err}=10^{-9}$		
Gravitational forces [cm/sec ²]	$g_x=0.0$ $g_y=0.0$ $g_z=0.0$	$g_x=0.0$ $g_y=0.0$ $g_z=981.0 \text{ cm/sec}^2$		
Collision model	off	SoI=5V·Δt radii SoI=20V·Δt radii SoI=10V·Δt·Zp radii SoI=one grid cell		

Table 4-4. Grid Configurations for Parametric Studies.

Grid designation	Length [cm]	Width [cm]	Δx	Δy	Δz
A-A	10	1	0.1	0.1	0.5
B-A	10	1	0.05	0.05	0.5
C-A	10	1	0.025	0.025	0.5
B-B	10	1	0.05	0.05	0.25
C-B	10	1	0.025	0.025	0.25

other quantities that directly impact the particle model (atomization constant, particle injection rate, collision modeling); on the other hand, spray tip penetration is primarily affected by the gas/particle drag interaction and is therefore highly influenced by variation in gas phase modeling parameters (drag law, grid spacing, timestep, etc). This is not to say that changes to the gas phase modeling did not affect the drop sizes calculated, or that tip penetration was not effected by changes to the particle modeling, merely that the effects stated previously were more pronounced.

4.3.1.1 Comparison of Baseline Results with Experiment

The diesel fuel spray experimental data [29] used in this study consisted of a single circular orifice nozzle with diesel fuel being injected into a pressure vessel. The pressure in the chamber was 1.1 MPa, and the liquid was injected at a bulk velocity of 102 m/sec. LISAM was used to predict the transient behavior of the diesel fuel spray. The LISAM computation used as a baseline comparison with this experimental data used the Reitz injection and breakup model with an atomization constant, $B_1=20$. Appendix A contains the input file for this baseline LISAM case. Figure 4-2 shows the values calculated by LISAM for an axial distribution of time-averaged SMDs along with the computational results reported by Reitz [4] and the experimental data point [29]. This figure shows that LISAM underpredicts the average drop sizes predicted by Reitz at all locations. LISAM also underpredicts the experimental data point. One possible explanation for this discrepancy is that the baseline computation shown in Figure 4-2 does not include the effects of collision modeling, which is included in the calculation reported by Reitz[4]. The collision model would allow for droplet coalescence and recombination, which could increase drop sizes at downstream locations. The effects of

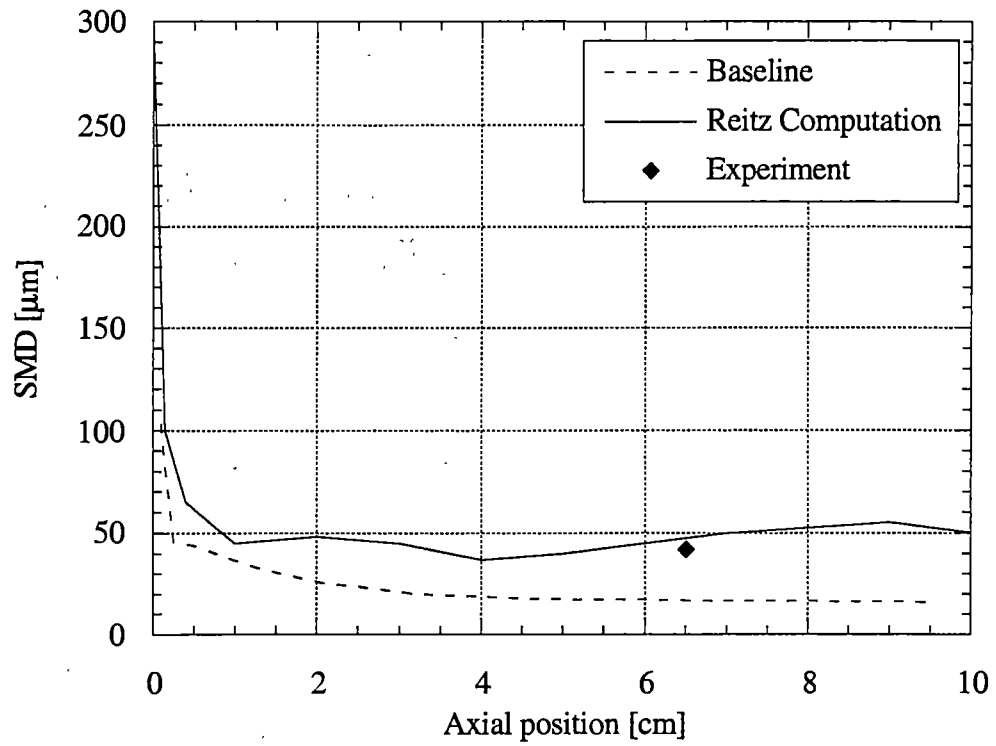


Figure 4-2. Comparison of Computational and Experimental Time Averaged Sauter Mean Diameters.

collision modeling are investigated later in this chapter. Also omitted from the LISAM model is turbulence modeling, which is included in the KIVA program used by Reitz. Turbulence would tend to slow the liquid drops and reduce the relative gas/liquid velocity which would slow the rate of droplet breakup. These turbulence effects could increase predicted drop sizes. No turbulence model was included in LISAM. Figure 4-3 shows a drop size population and mass distribution for all of the drops that passed the 6.6 cm measurement station during the 4.5 msec run time of the LISAM prediction. The largest population of is below 20 μm . The mass is also primarily concentrated in the small drops, but the very large drops constitute a significant portion of the mass, even though they are not a significant portion of the drop population. Figure 4-4 shows the rate at which the spray penetrates the gas field. The LISAM calculation predicts a faster penetrating spray than either the experimental results or the computations made by Reitz [4]. Possible explanations for this are the lack of a collision and turbulence models and also, as will be shown in the parametric studies, the tip penetration rate is very sensitive to changes in the gas field, therefore any parameters which affect the gas field, such as grid spacing, will also affect penetration rates.

Also, the LISAM calculations show a non-smooth or 'wavy' penetration curve. Later simulations showed that this behavior was directly related to the definition used to identify the leading tip of the liquid spray. Further discussion of this behavior is included in a later section.

Effects of varying these parameters are investigated later in this chapter. Figures 4-5 and 4-6 show two side views of the liquid spray at 4.5 msec of simulation time. Figure 4-5 shows a side view looking at the x-z plane, with a one-to-one aspect ratio for the axes. Figure 4-6 shows the same view, with the transverse x-scale reduced to enlarge the image for easier viewing of detail. The drop sizes shown reflect three size

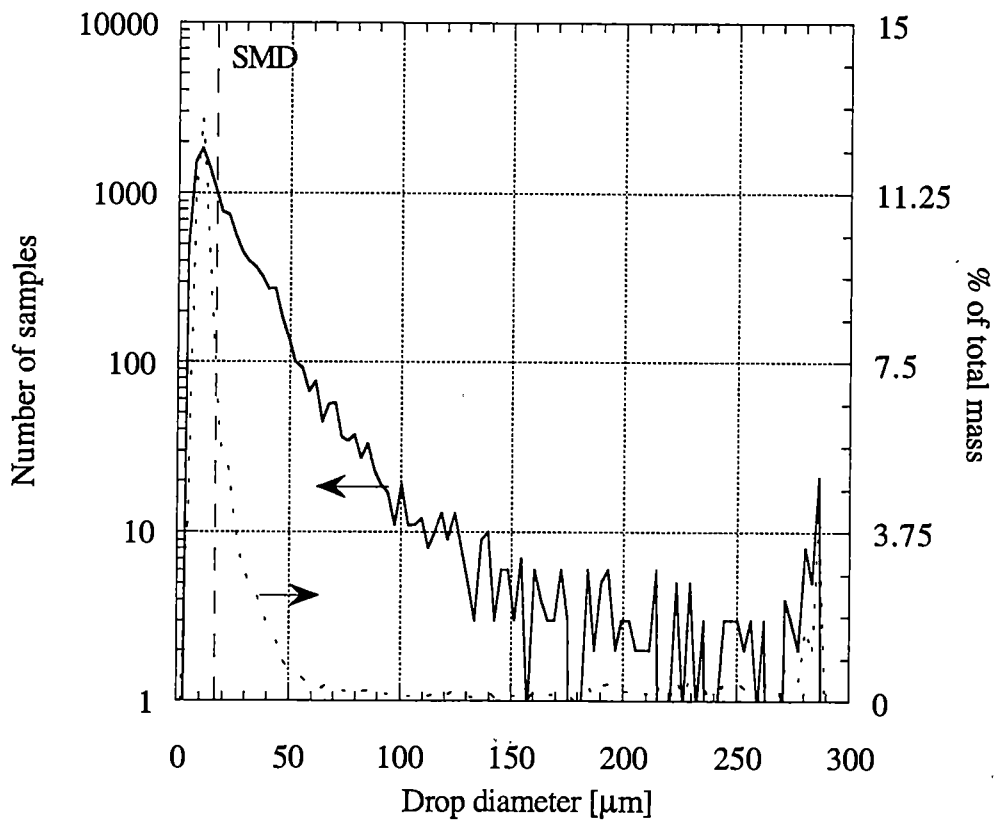


Figure 4-3. Drop Size Population and Percent Mass Distributions at 6.6 cm for Baseline LISAM Prediction.

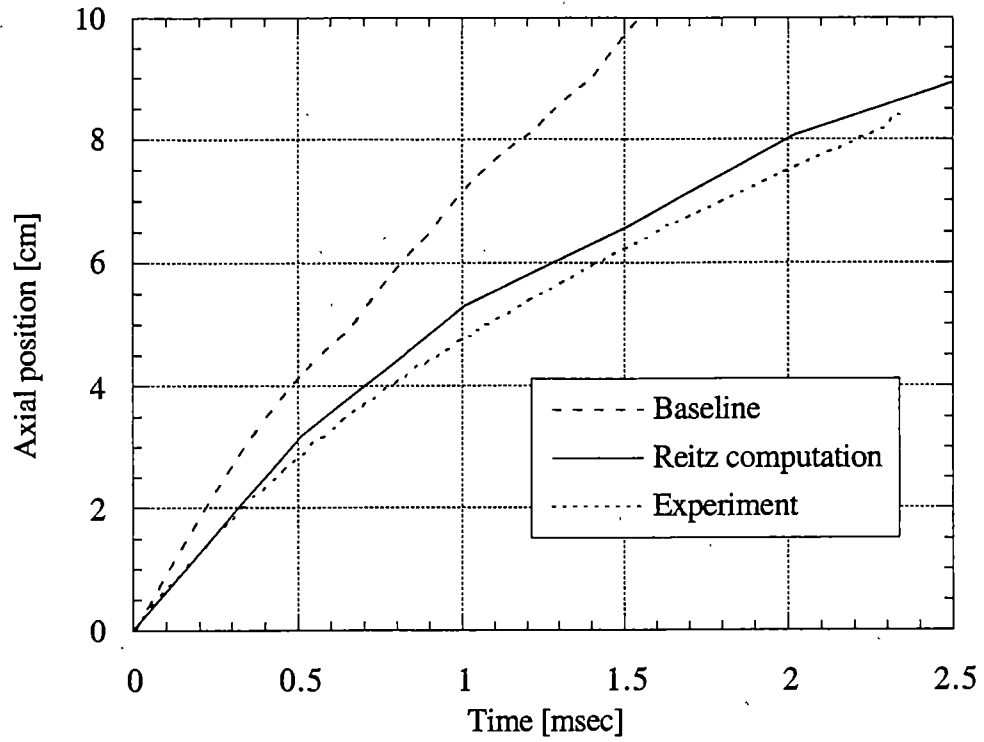


Figure 4-4. Comparison of Computational and Experimental Tip Penetration Histories.

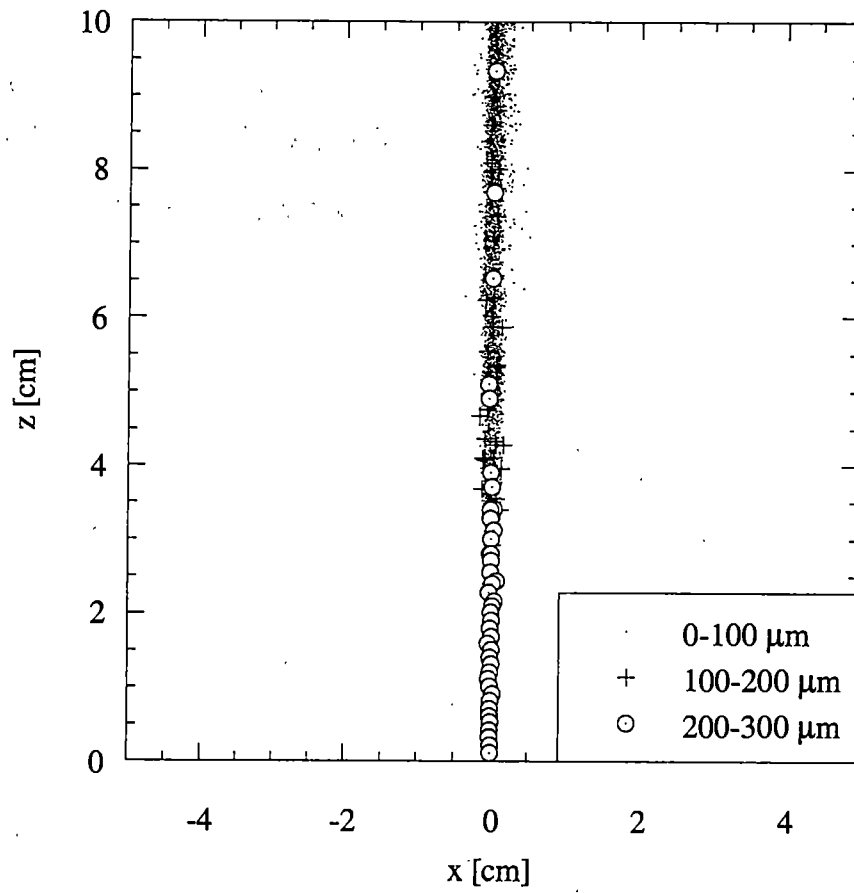


Figure 4-5. Baseline Spray Pattern at 4.5 msec.

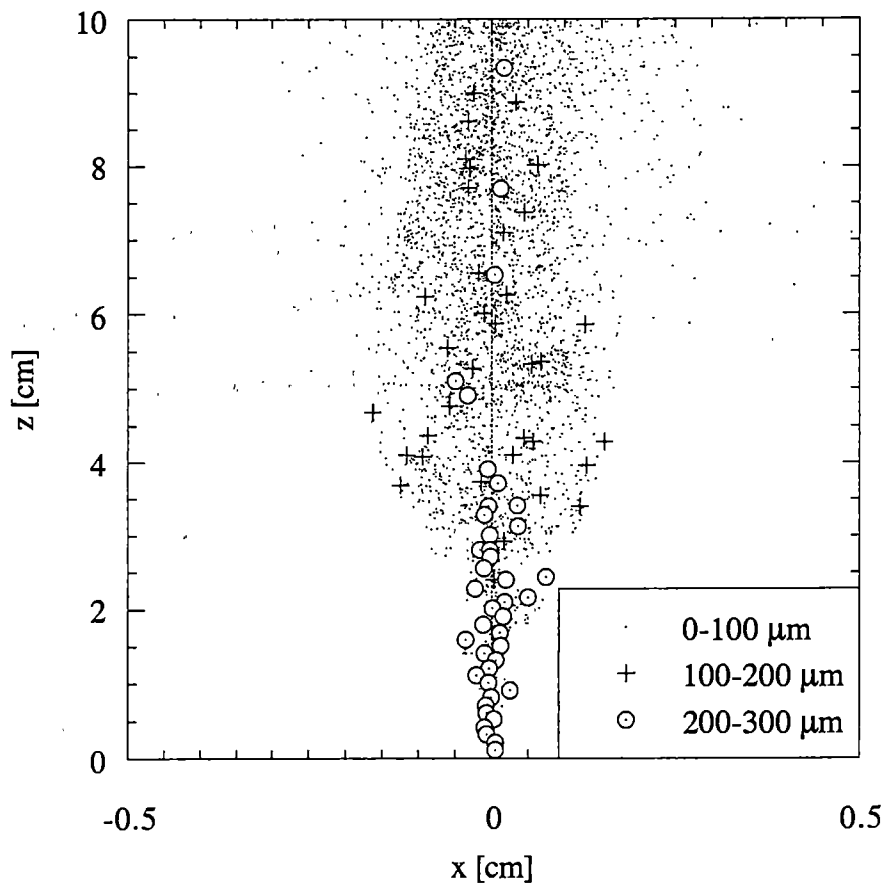


Figure 4-6. Enlarged View of Baseline Spray Pattern at 4.5 msec.

regimes, represented by different symbols. The largest drops (200-300 μm) are concentrated near the injector, and disappear after approximately 4 cm. Drops in the 100-200 μm range persist in the flow until about 9 cm downstream of the injector. Figure 4-7 shows the flow in the x-y transverse plane, with the flow coming directly out of the page. This view serves primarily to verify that the liquid spray is symmetric around the axial (z) axis. Note, however, that the spray does not exhibit perfect symmetry. This is a result of the statistical or stochastic, three dimensional nature of the computation. Later results will show that when more computational parcels are used in the calculation the spray becomes more symmetric.

4.3.1.2 Impact of Statistics on LISAM Predictions

The ability to use representative computational parcels to model an actual spray is vital to the computational modeling of sprays. If a spray had to be modeled using a realistic number of droplets, the computational requirements would be onerous. Therefore, a computer model must be able to represent the 'average' behavior of a large number of drops with a relatively small number of computational parcels. The primary parameters that affect the statistical results of LISAM are the computational particle injection rate, P_{inj} and the grid spacing of the computational domain. If there are not enough particles in the system, the statistics of the model will be poor. The third factor in this study that must be considered is the assumption of negligible liquid density in a grid cell, the assumption is made in LISAM that any effect on the gas flow caused by the volume of liquid present in a grid cell has been neglected. Because this assumption of negligible liquid volume was made, the 'cluster' drag model that is available in LISAM was not used for the studies presented here. The impact of the variation of

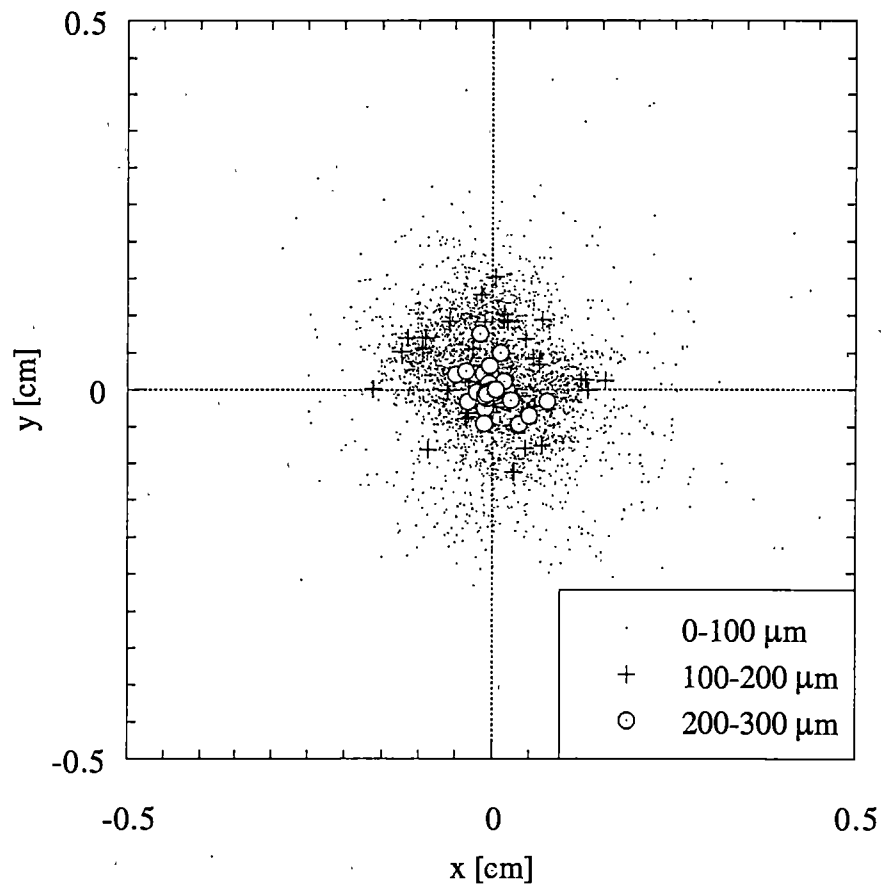


Figure 4-7. Baseline Spray Pattern at 4.5 msec 'X-Y' view.

these statistical parameters must be examined and trade-offs must be made. Of course, the larger the number of parcels used to represent the flow, the more accurate the statistical model will be, but this increases the burden on the computer model and can greatly degrade code performance. This requires a modeler to decide at what level the statistics of a problem are adequate, do not violate model assumptions, and still allow the program to run at a reasonable rate.

Figure 4-8 through 4-11 show the same liquid spray modeled with 4 different computational parcel injection rates. It can be clearly seen that when a greater number of computational parcels is used to model a flow, the physical characteristics of the spray are more clearly defined. This does not, however, mean that predicted spray properties change for each case. It will be shown in the following sections that the results shown in Figure 4-9, 10, and 11 all given very similar results for both drop size measurements and spray tip penetration rates, but the spray in Figure 4-8 gives different, poorer, results. For this lower particle release rate (10^4 particles/sec) there are not enough computational parcels in the system to adequately define a spray. The physical appearance of the spray is poorly defined, and the spraytip penetration and SMD calculations do not correlate with experimental data. Experimental bench mark data including the number of droplets passing through a measurement volume during a given time would provide valuable data for use in model validation. This data could provide a critical correlation feature for spray models to simulate.

4.3.1.3 Time-Averaged Sauter Mean Diameter Measurements

The parameters found to have the greatest impact on Sauter Mean Diameter distributions were: atomization model, the atomization constant (B_1), and collision

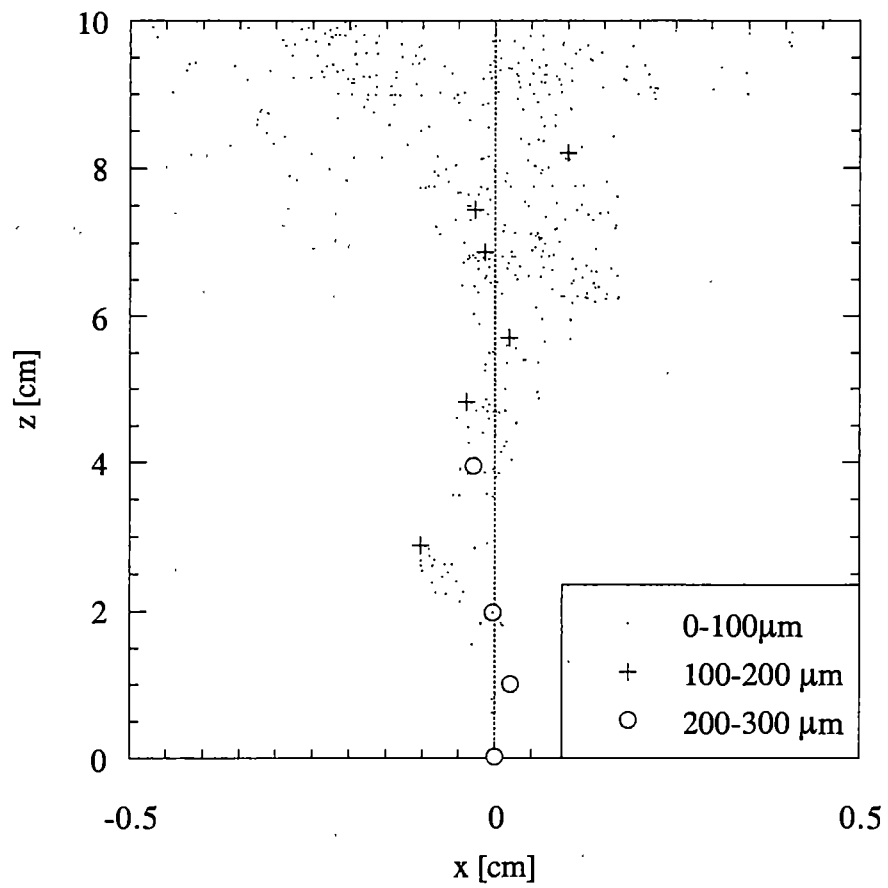


Figure 4-8. Spray Pattern for $P_{inj}=10^4$.

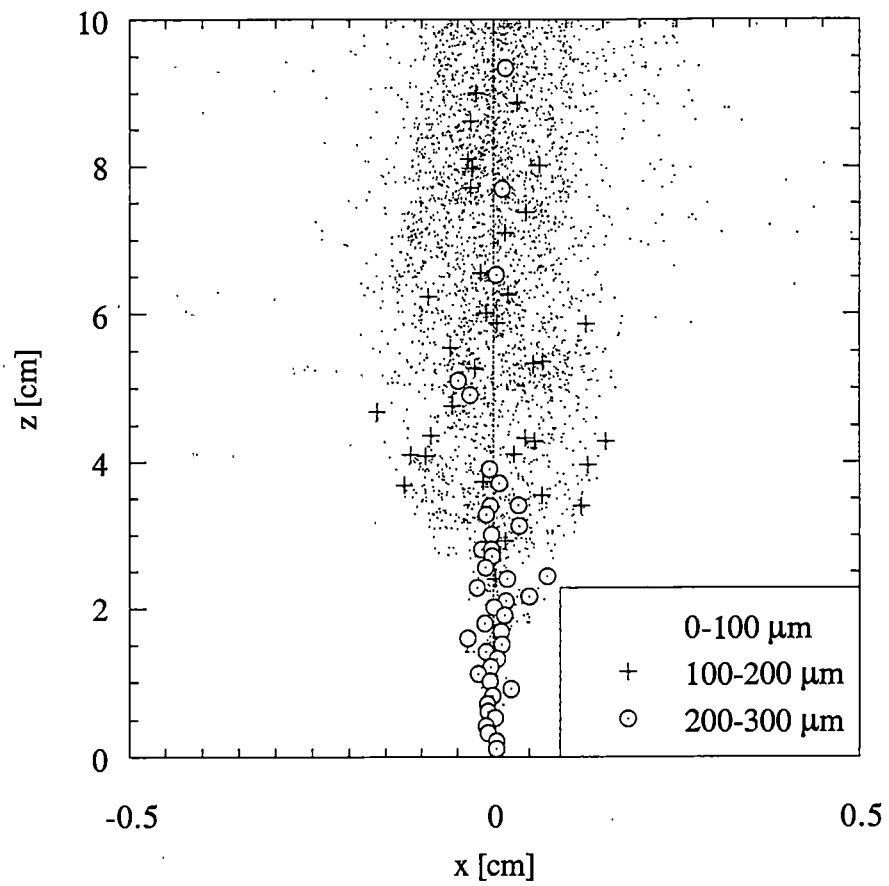


Figure 4-9. Spray Pattern for $P_{inj}=10^5$ (Baseline).

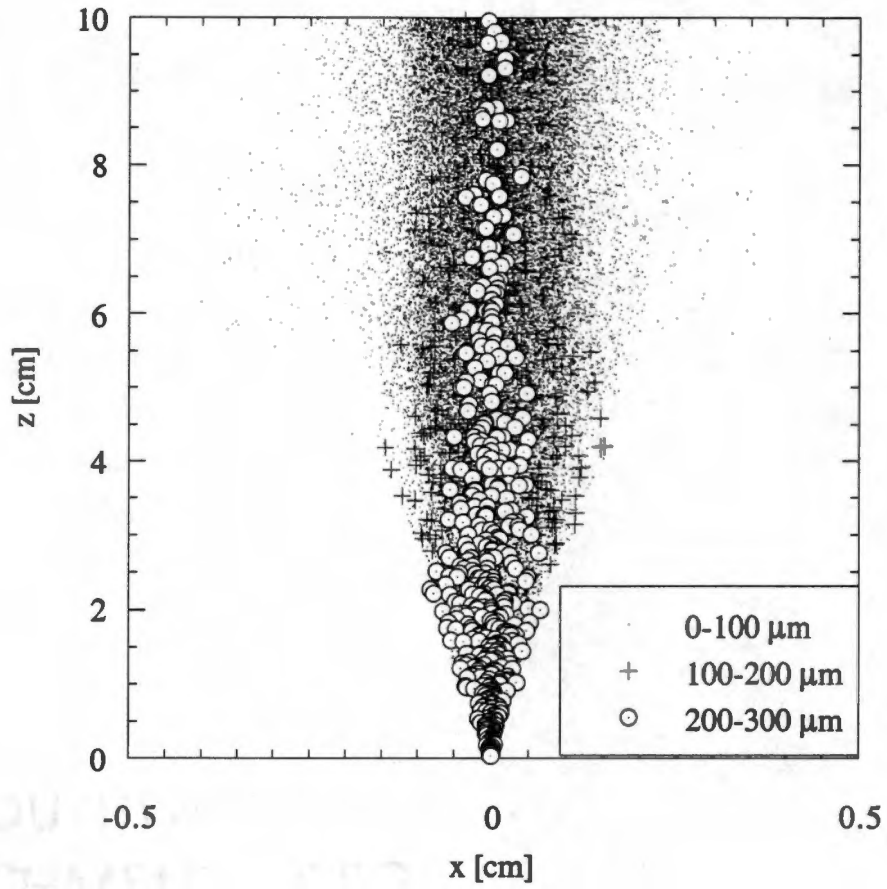


Figure 4-10. Spray Pattern for $P_{inj}=10^6$.

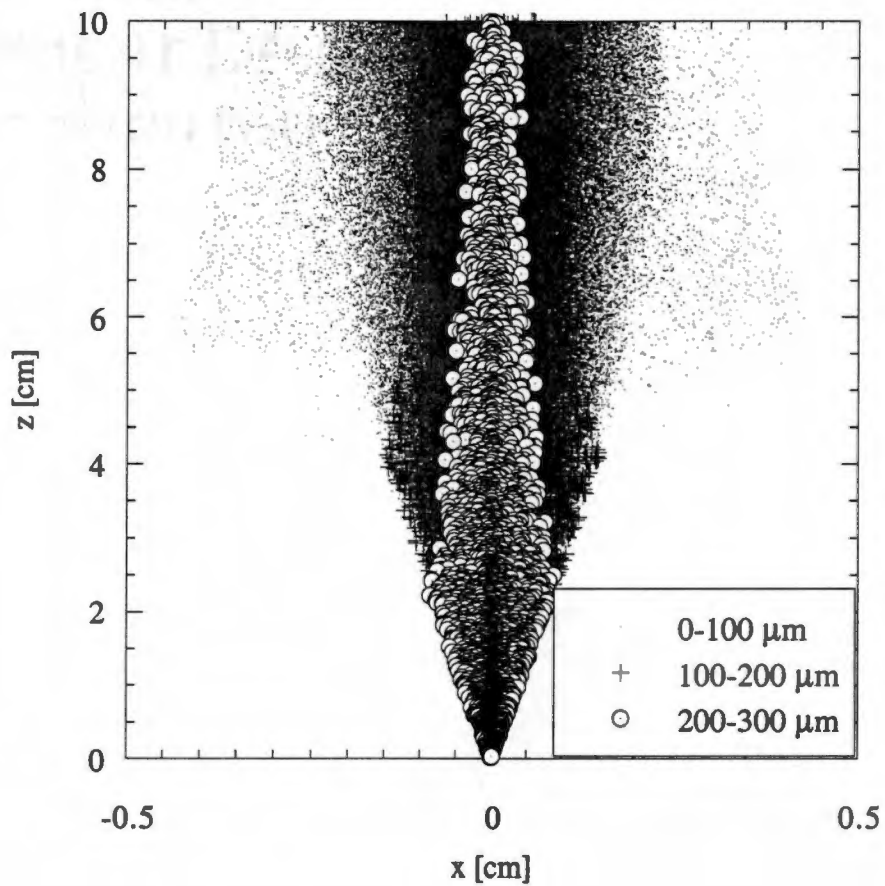


Figure 4-11. Spray Pattern for $P_{inj}=107$.

modeling(see Figure 4-12 through 4-15). Figure 4-12 shows the axial distribution of time-averaged SMDs as a function of jet/droplet breakup models, at a computational time of 4.5 msec. The SMD distributions for all of the atomization models available in LISAM, as well as the tetradecane experimental data point and computational values reported by Reitz using KIVA [4] are shown. As can be seen, there a substantial variation in computed drop sizes for the different atomization models. Most significantly, the Andrews model predicts substantially less droplet breakup than any other model and overpredicts, by about 250%, the SMD value at the location of the experimental data. The LISAM calculations made using the Reitz and O'Brien atomization models are indistinguishable, which is not surprising since they have only small differences in modeling technique. They both predict drop sizes about half of that predicted by Reitz's computations [4]. The TAB and NDBT models calculate an extremely rapid breakup process and then very small drop sizes downstream. These results tend to favor the Reitz/O'Brien modeling technique as the superior method for modeling droplet breakup for this experiment. While LISAM's predicted drop sizes are smaller than the single experimental data point and the computational data from Reitz, the shape of the predicted curves are similar and the predicted drop sizes near the injector are much closer to the Reitz calculation. Figure 4-13 shows the SMD distributions calculated using the Reitz model, for various values of the atomization constant B_1 . A baseline value of $B_1=20$, in the Reitz breakup model, was used. Variations of B_1 from 5 to 50 were made, and for these cases a $B_1=20$ best matched Reitz's own computations in the near nozzle region. Farther downstream all of the computations predicted values were below those calculated by Reitz and the experiment data point. Reitz tried several values and chose the value $B_1=10$ to be the best for his calculations, but he included a droplet collision model in computing his KIVA-based

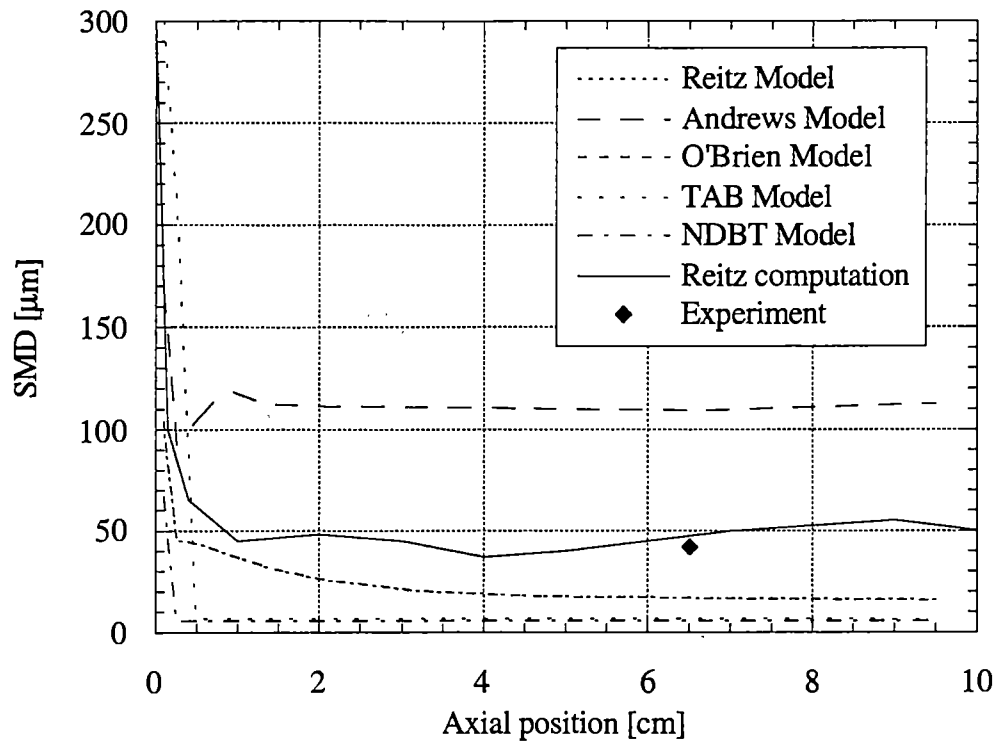


Figure 4-12. Axial Distribution of SMD for Various Breakup Models.

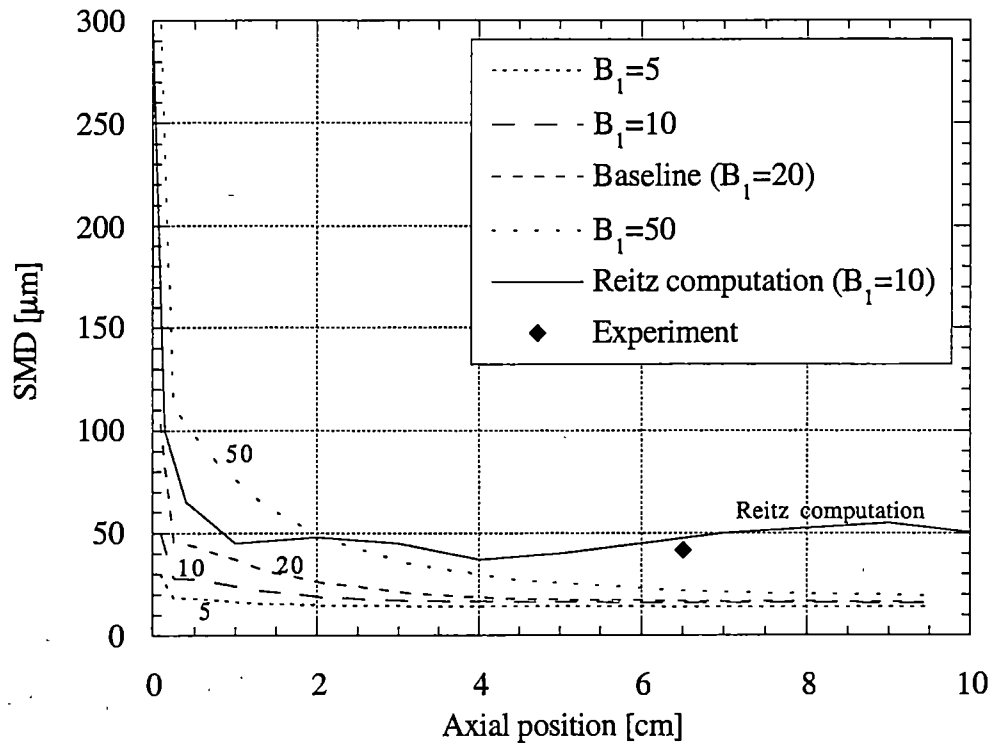


Figure 4-13. Axial Distribution of SMD for Various Values of B_1 in Reitz Model..

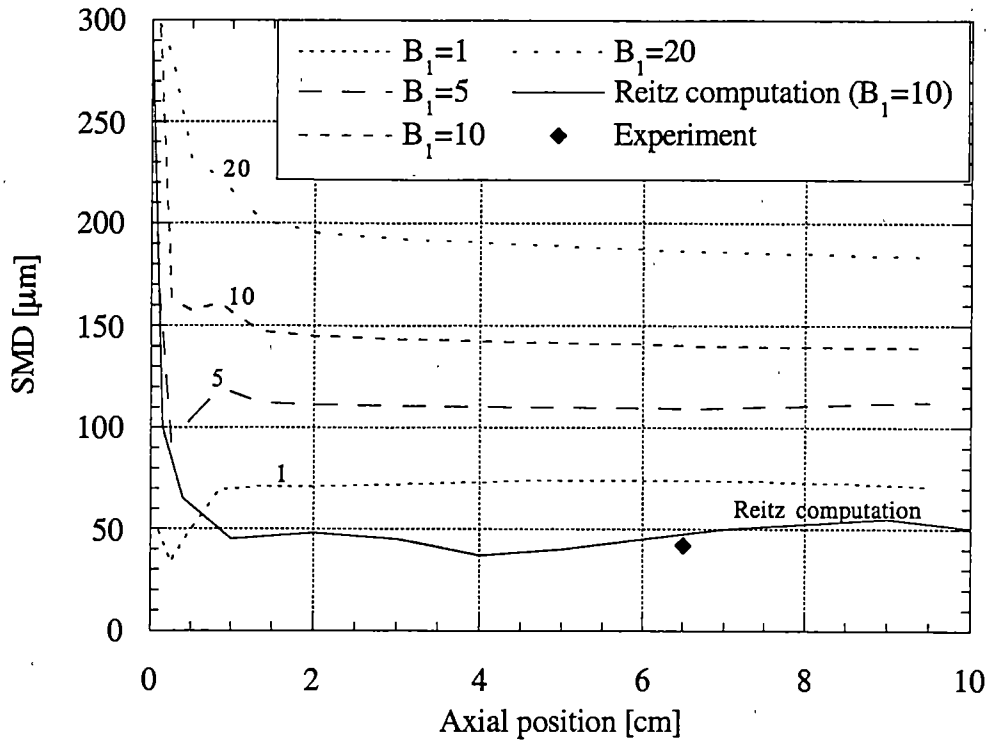


Figure 4-14. Axial Distribution of SMD with Variation of B_1 in Andrews Model.

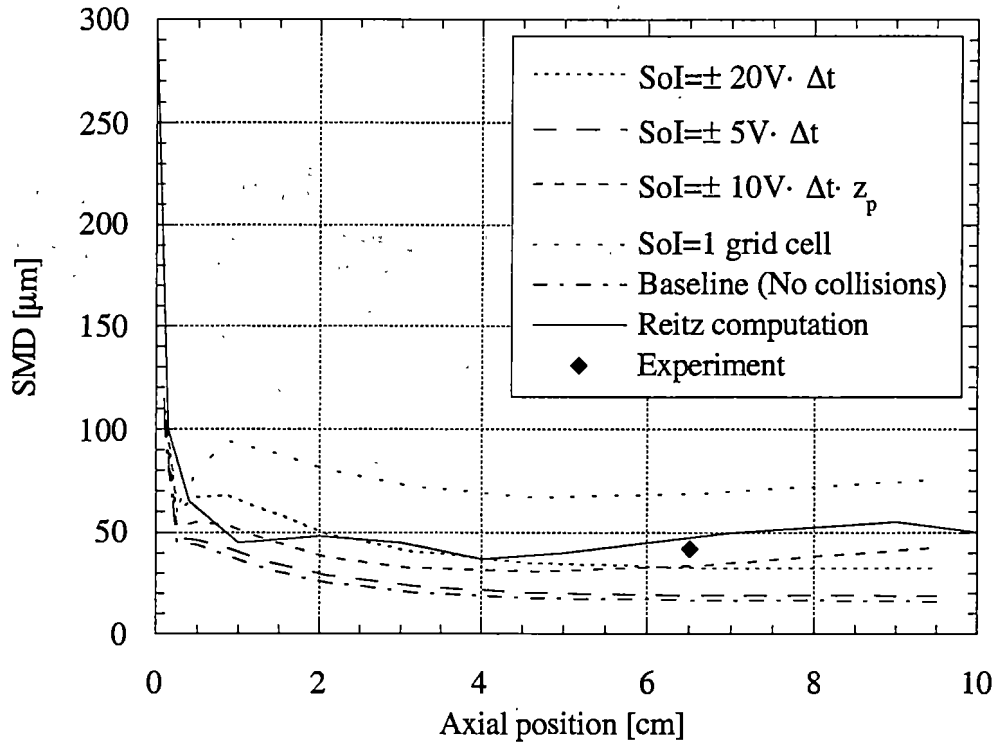


Figure 4-15. Axial Distribution of SMD With and Without Collisions.

results [4]. This discrepancy between the LISAM results and the Reitz computation and the experimental results can be, at least partially, attributed to the lack of the collision/coalescence model in the LISAM calculations. Figure 4-14 shows the SMD distributions calculated using the Andrews model, for various values of the atomization constant B_1 . A value of $B_1=5$ was found to give the best match with Reitz's computation while still maintaining a similar shape to the distribution curve. A $B_1=1$ reduces the predicted SMDs further but also predicts drastic droplet breakup near the injector resulting in drop sizes much smaller than those predicted by Reitz. Figure 4-15 shows the SMD distributions when collision modeling was included. These results clearly indicate that the process of collision and coalescence plays a vital role in establishing the SMD drop size of a spray. The various results shown in Figure 4-15 show that the collision model is affected by how large a parcel's sphere of influence (SoI) is. Reitz used the KIVA method of determining the SoI, one grid cell. This method is highly grid dependent and if a variable grid is used (as in the Reitz paper [4]) the SoI can change within a calculation based on the parcel location in the computational domain. As discussed previously, an alternate form was developed by the author for LISAM (See Section 2.3.1.2), where the parcel's SoI is determined by its velocity and the computational timestep; this offers a grid-independent solution to this problem. However, this technique is significantly more computationally intensive. A SoI of $\pm 10V \cdot \Delta t \cdot z_p$ (where z_p is the parcel's axial location) was found to best match the results from the Reitz paper. This method of calculating SoI mimics a variable grid single cell SoI, like that used by Reitz. The variation in results based on how the SoI is calculated highlights the significance of the choice of the SoI. The best match results show SMDs rising in value near the chamber exit much like the Reitz paper results. Further study into the choice of SoI should be conducted to better determine an optimum method. The

drop population and mass distribution for the $SoI = \pm 20 \cdot V \cdot dt$ are shown in Figure 4-16. Similar to the baseline distribution (Figure 4-3) the largest population of drops are below $30 \mu m$. The mass distribution is almost equally weighted to the smallest and largest drops. If the coupling between particle drag and gas momentum is severed so that the gas causes drag on the droplets but the particle drag no longer induces a momentum change in the gas, some interesting behavior is predicted. Figure 4-17 shows the SMD distribution for this 'one-way' drag coupling. Drop sizes near the injector are larger than the baseline computation, but approach the baseline 'two-way' coupled results farther downstream. The last data point calculated on the 'one-way' coupled curve was very much larger because very few drop parcels penetrated the gas to that point and is not shown on the figure. It will be shown later that the spray never fully penetrates the gas field when gas motion is not induced by the spray.

Other parametric variations had little effect on the SMD distributions. Particle injection rates of 10^5 , 10^6 and 10^7 provided effectively identical results, while a $P_{inj} = 10^4$ gave slightly larger average drop sizes. This effect can be attributed to a reduction in statistical accuracy. Grid spacing had minimal effects on average drop size. Grid dimensions had no effect on average drop size, showing that there are no side wall, or edge effects altering the results. This allows a smaller chamber to be modeled to better focus on the areas of interest. However care must be taken to make the chamber large enough that edge effects from the solid wall, i.e. unrealistic recirculation effects, are not induced. A small computational domain allows a denser grid to be used without raising computational run times to unreasonable levels. Variation of the primary timestep showed no difference between average drop sizes calculated using Δt from 5×10^{-6} to 10^{-7} , however, the overall stability of the computation degraded for primary

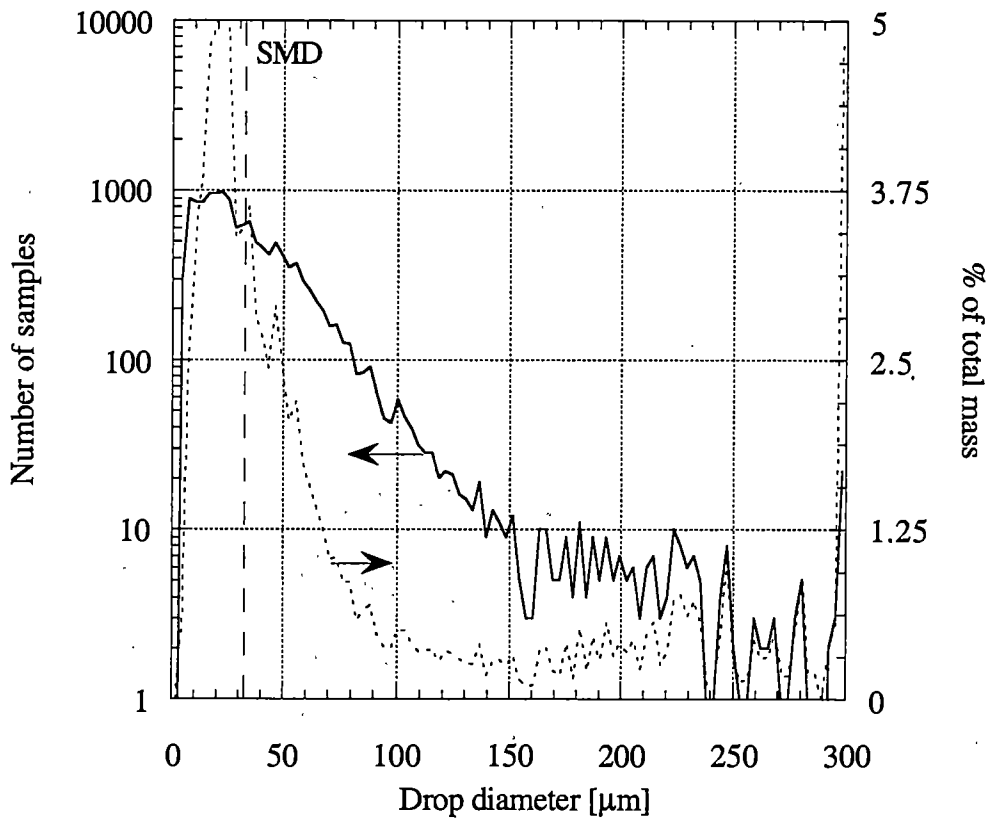


Figure 4-16. Drop Size Population and Percent Mass Distribution at 6.6 cm for LISAM Simulation with Collisions.

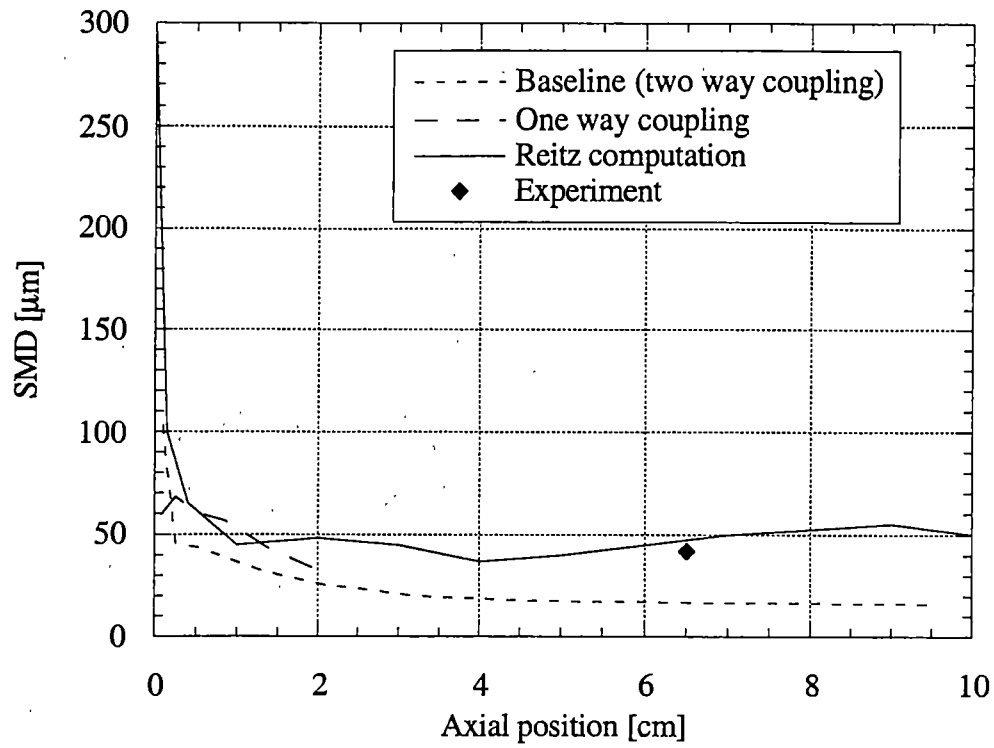


Figure 4-17. Sauter Mean Diameter Distributions with Variation in Drag Routine.

timesteps above 5×10^{-6} . So 5×10^{-6} sec is taken as an upper limit for these computations. The change in dual timestep, $\Delta\tau$, also had no noticeable effect on the average drop size. It did however have a dramatic effect on actual run time of the LISAM program. By decreasing $\Delta\tau$ from 10^{-6} to 10^{-7} the number of inner iterations per timestep needed to converge on a solution for the gas phase model doubled and run time increased by 68%. Relaxation of convergence criteria from $V_{err}=10^{-9}$, $\rho_{err}=10^{-9}$, to $V_{err}=10^{-4}$, $\rho_{err}=10^{-2}$ had no effect on drop size distributions, but did have an effect on run time. This relaxation of convergence criteria allowed for fewer inner iterations and therefore a 70% reduction in run time, from 258 minutes to 74 minutes. The inclusion of gravity as a body force on the droplets had no effect on drop size distributions.

4.3.1.4 Spraytip Penetration Rates

As mentioned previously the calculated rate at which the spray penetrates the gas is greatly influenced by changes to the gas field computed by LISAM. Figure 4-18 illustrates this point (See Table 4-4 for grid designation descriptions). It shows the calculated tip penetration rate calculated for the same spray using five different grid spacing setups. The range of computed penetration rates is caused by changes in the gas field. Figure 4-19 shows the centerline axial gas velocity profile at 1 msec. As the transverse grid becomes denser the predicted gas velocity rises. Denser transverse grids predict profiles that have propagated farther downstream. Denser axial grids lower the predicted gas velocities. Clearly, the importance of accurately predicting the gas field

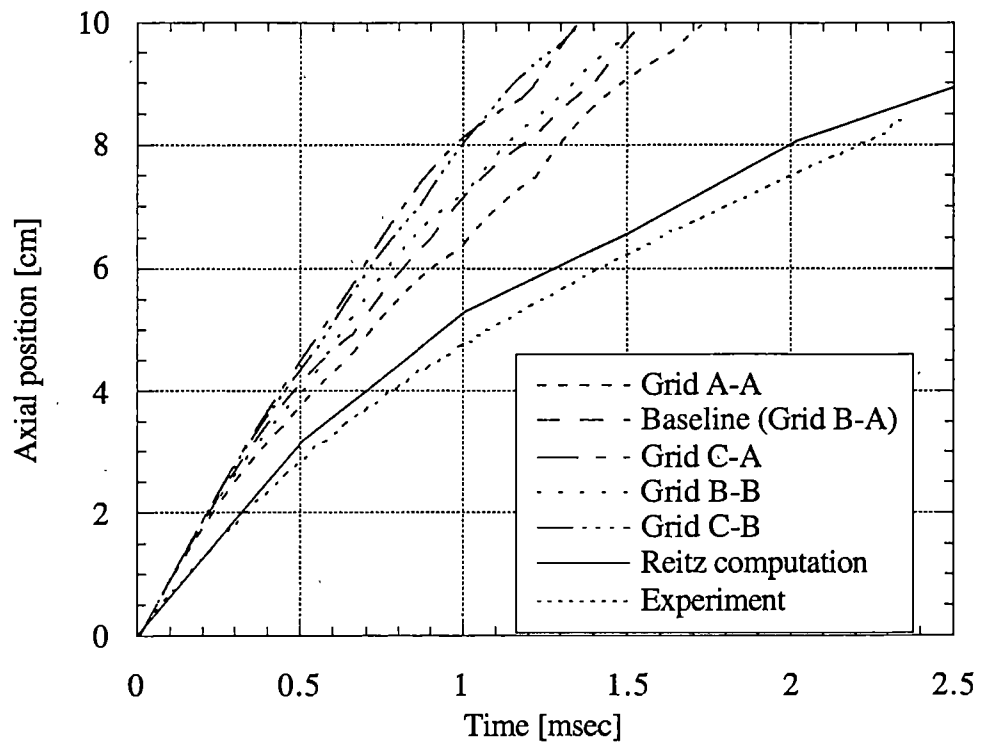


Figure 4-18. Spray Penetration for Different Grid Spacings.

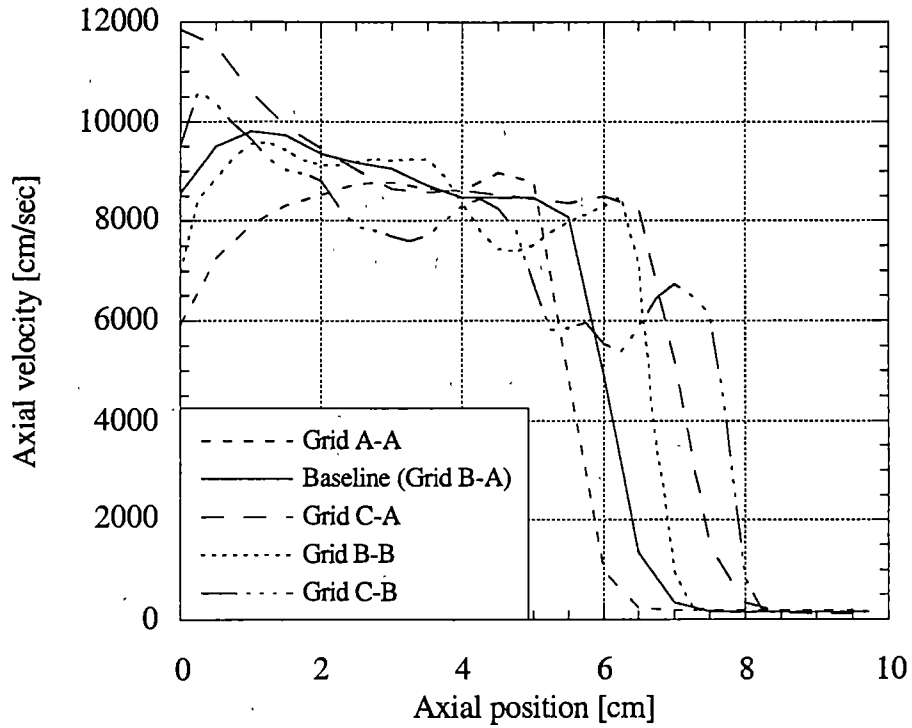


Figure 4-19. Centerline Gas Axial Velocity Profiles for Different Grid Spacings after 1 msec.

resulting from spray interaction can not be underestimated. In combustion situations the ability to predict where the spray is, as well as the drop size constituency, is of great importance. The breakup method used also affected spray penetration rate (see Figure 4-20). Clearly the effects of breakup also impact the rate at which the spray penetrates the gas. Faster droplet breakup rates result in smaller drops, which are more strongly affected by gas drag effects and thus more significantly retard the spray tip penetration rate. The Andrews model predicts that the spray will penetrate the gas more rapidly than the other models, because the Andrews model also predicted, in Figure 4-12, larger drops farther downstream than the other models. This reinforces the concept that the large drops injected at the nozzle are less affected by drag influences from the gas than small drops resulting from droplet breakup. The O'Brien model, the TAB model, and the NDBT model show an intermediate value between that of the Reitz and Andrews model. None of the results predict the tailing off seen in the experiment. Figure 4-21 shows the variation of tip penetration rate with the atomization constant B_1 , using the Reitz breakup model. Clearly this parameter has a nonlinear effect on penetration rate. The results do not vary greatly from each other however, indicating that B_1 does not have a strong influence on the tip penetration rate. B_1 's primary function is to control the rate of droplet breakup, so its influence on tip penetration is through control of the size of the leading drop parcel. These results indicate that all of the values of B_1 used in this study predicted droplet breakup that was fast enough for all cases to create leading drop parcels of about the same size. Similar studies of B_1 variation using the Andrews model showed little effect on tip penetration. Variation of computational particle injection rate, P_{inj} , also leads to the changes in the tip penetration rate, Figure 4-22. Values of $P_{inj}=10^6$ and 10^7 gave very similar results; the results for $P_{inj}=10^5$ predict a

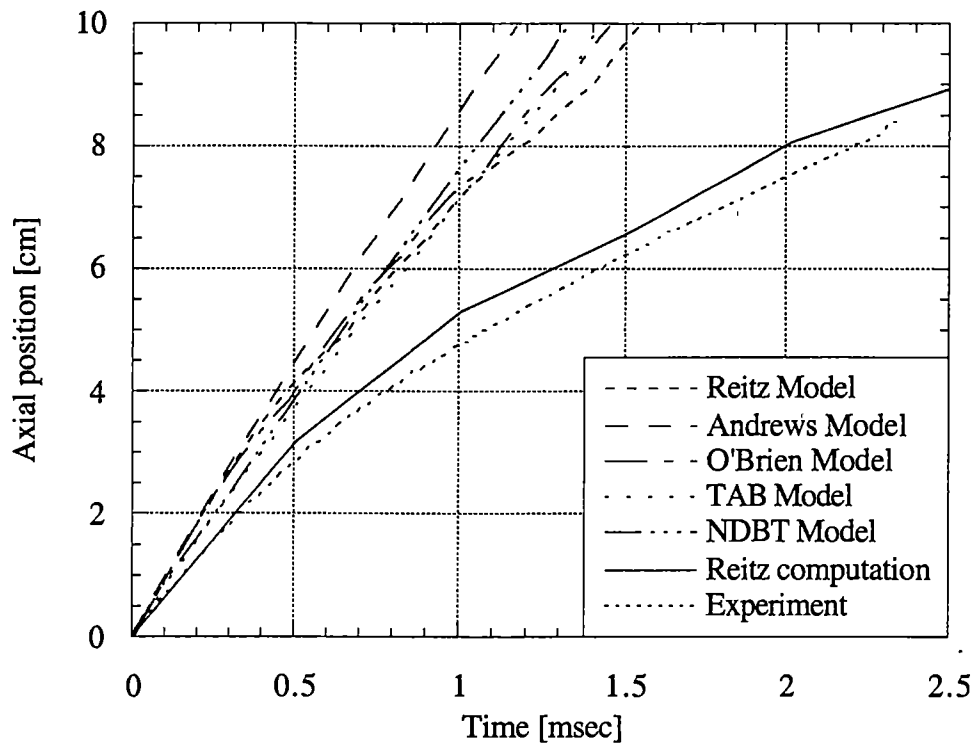


Figure 4-20. Spray Penetration Variation Due to Breakup Model.

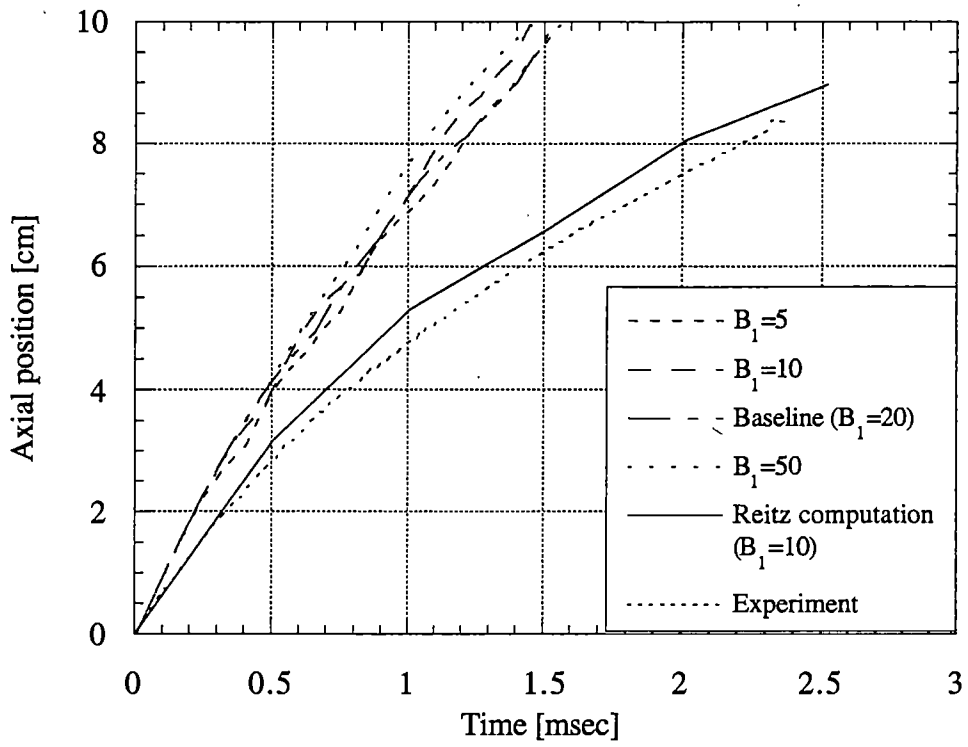


Figure 4-21. Spray Penetration for Various Values of B_1 Using Reitz Model.

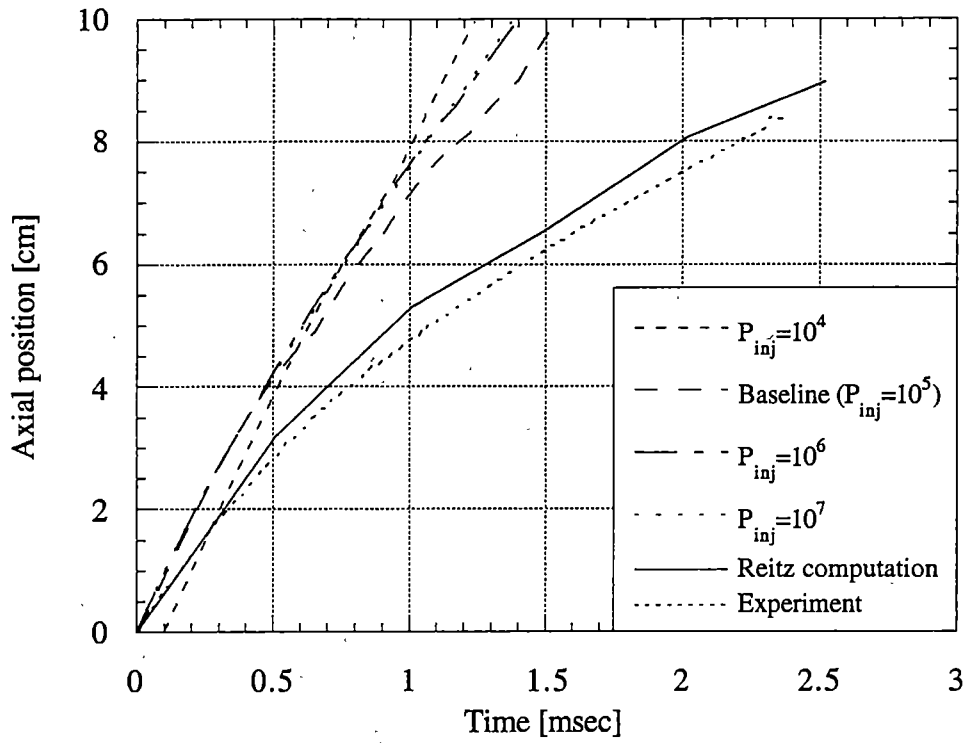


Figure 4-22. Spray Penetration for Various Particle Injection Rates.

slower tip penetration, and $P_{inj}=10^4$ results predict a faster penetration. This nonlinear $P_{inj}=10^4$ result strengthens the argument that this low particle injection rate does not provide adequate droplet representation to maintain statistical quality, or to adequately represent spray interaction with the gas field. A reduction in the dual timestep resulted in a slightly slower penetration rate (See Figure 4-23), again resulting from changes in the gas flow field. Figure 4-24 shows the centerline axial gas velocity profiles at 1 msec for both values of $\Delta\tau$. The faster spray penetration of the $\Delta\tau=10^{-6}$ case predicts a faster gas velocity profile.

The author also investigated the use of upwind differencing of the velocity derivatives in the momentum equation (See Section 2.3.2.1.1). Upwind differencing resulted in a slower predicted tip penetration than central differencing, Figure 4-25. Figure 4-26 gives the centerline axial gas velocity profile for both differencing schemes. Central differencing predicts a slightly faster gas field, but the profile becomes very choppy near the downstream end of the gas flow. A stricter convergence criteria increased the penetration rate (See Figure 4-27). Figure 4-28 shows a correlation similar to those seen previously between penetration rate and gas velocity. The gas velocity is faster when the tip penetrates the gas more quickly. The 'one-way' drag coupling (Figure 4-29) retards the spray penetration so much that it does not traverse the entire chamber during the modeling time. As the drops pass through the chamber the gas continues to create drag on the parcels but the gas velocity never increases, so that the relative liquid/gas velocity remains large and the drops eventually become almost stationary. Other parametric studies conducted (collision modeling, timestep variation, chamber dimensions, and gravity) had minimal effect on the penetration rate. Most of the variation of spray penetration rate seen in Figures 4-18, 4-20-4-23, 4-25, 4-27, and

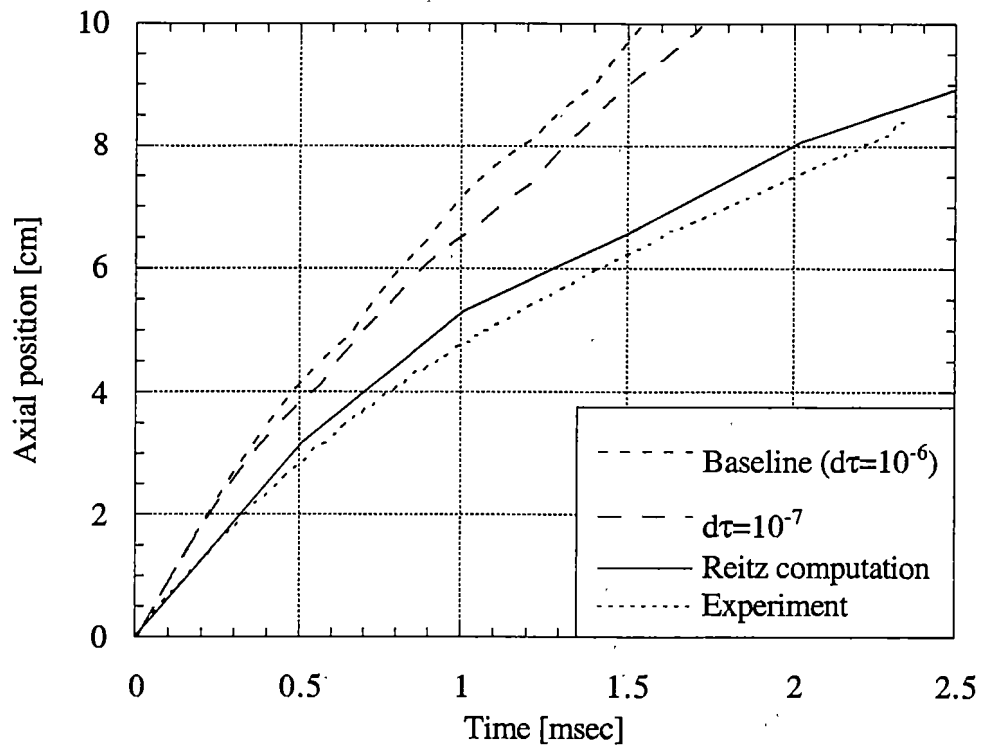


Figure 4-23. Spray Penetration for Different $\Delta\tau$.

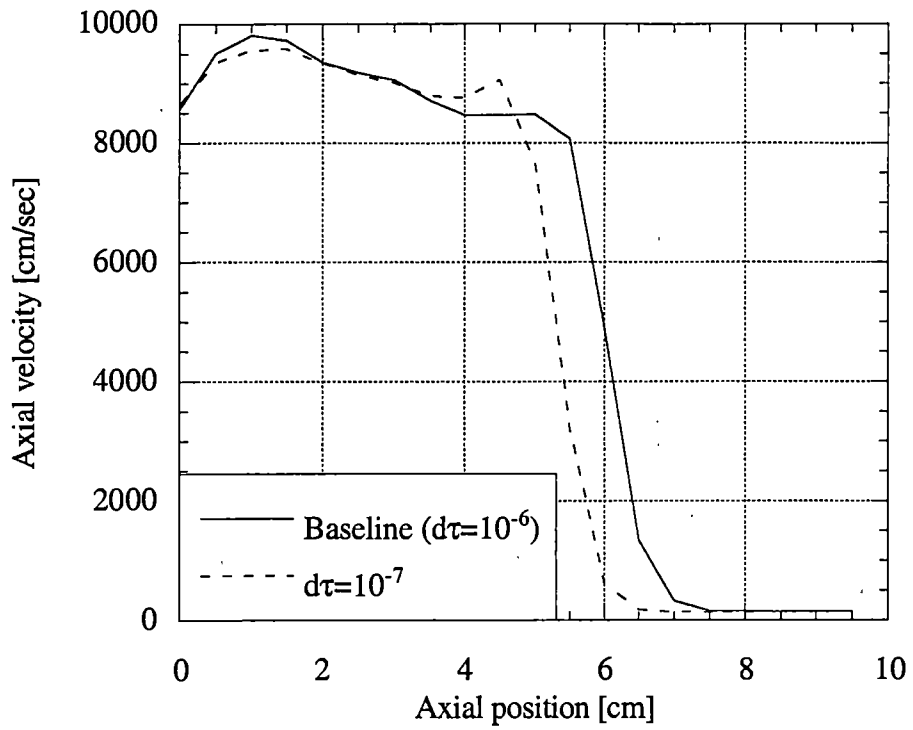


Figure 4-24. Centerline Gas Axial Velocity Profiles for Different $\Delta\tau$ at 1 msec.

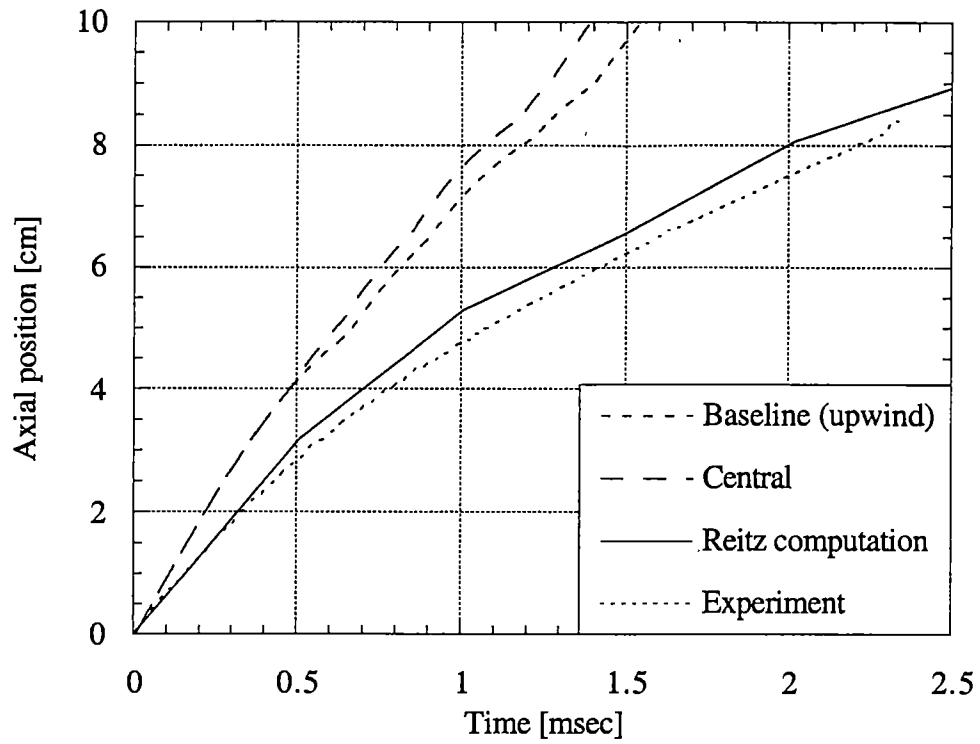


Figure 4-25. Spray Penetration for Various Differencing Schemes.

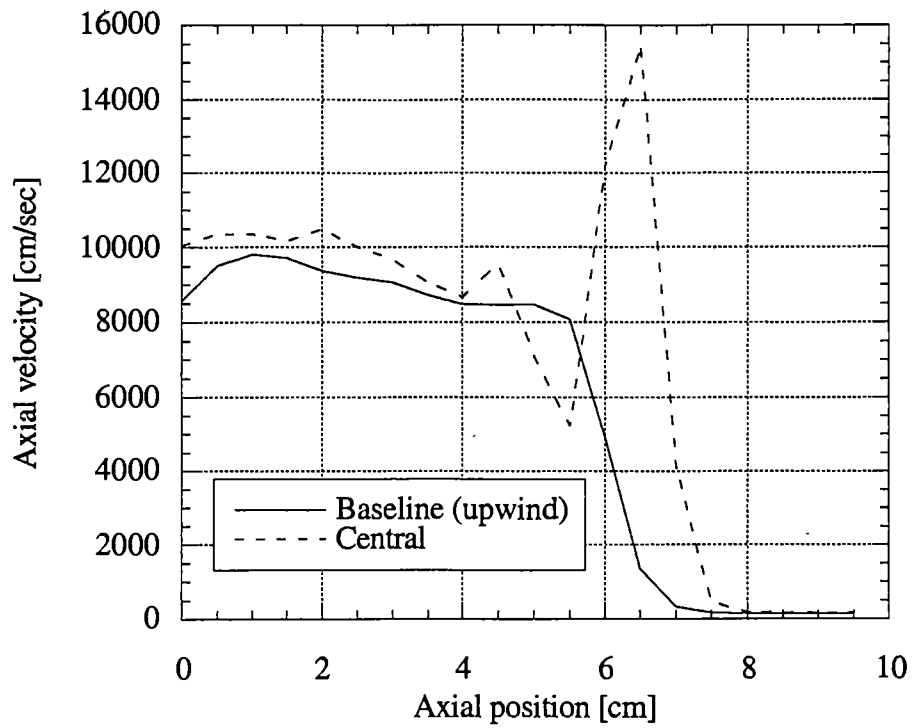


Figure 4-26. Centerline Gas Axial Velocity Profiles for Different Differencing Schemes at 1 msec:

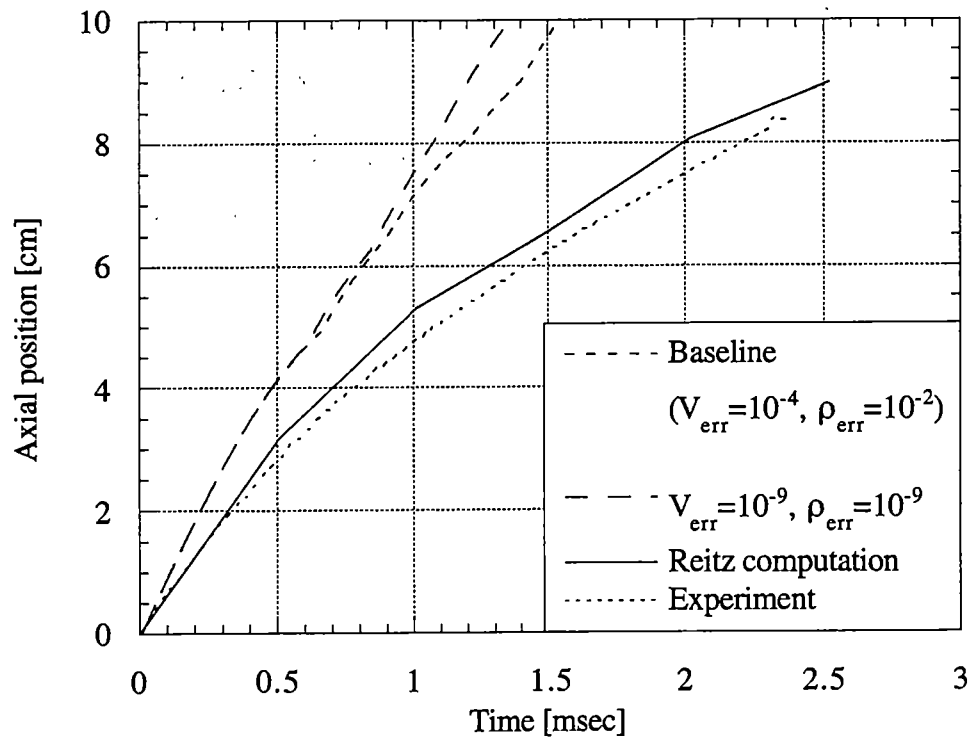


Figure 4-27. Convergence Criteria Effect on Spray Penetration.

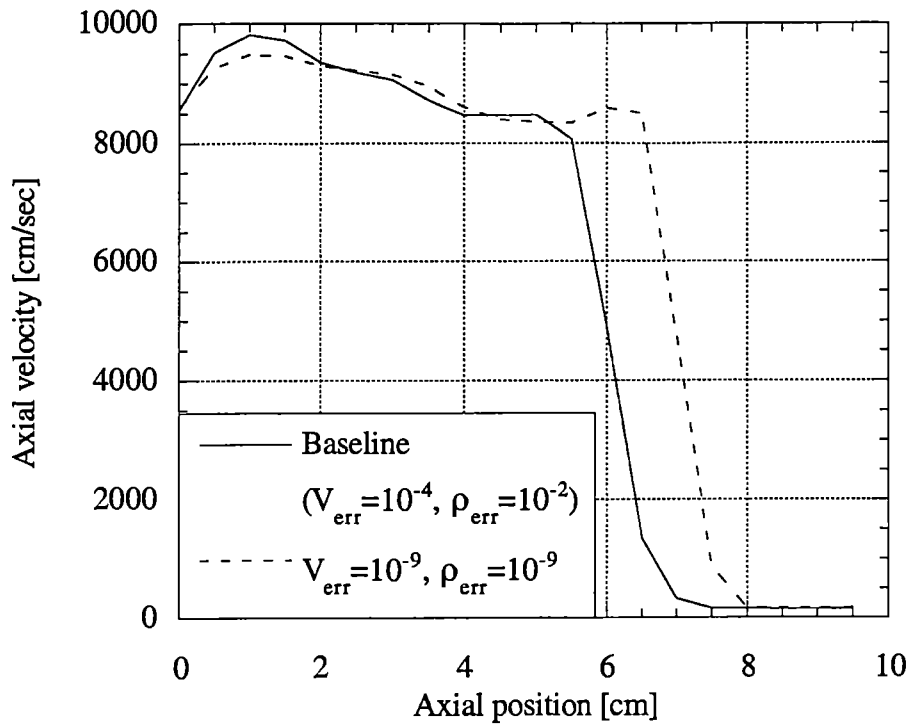


Figure 4-28. Centerline Gas Axial Velocity Profiles for Different Convergence Criteria at 1 msec.

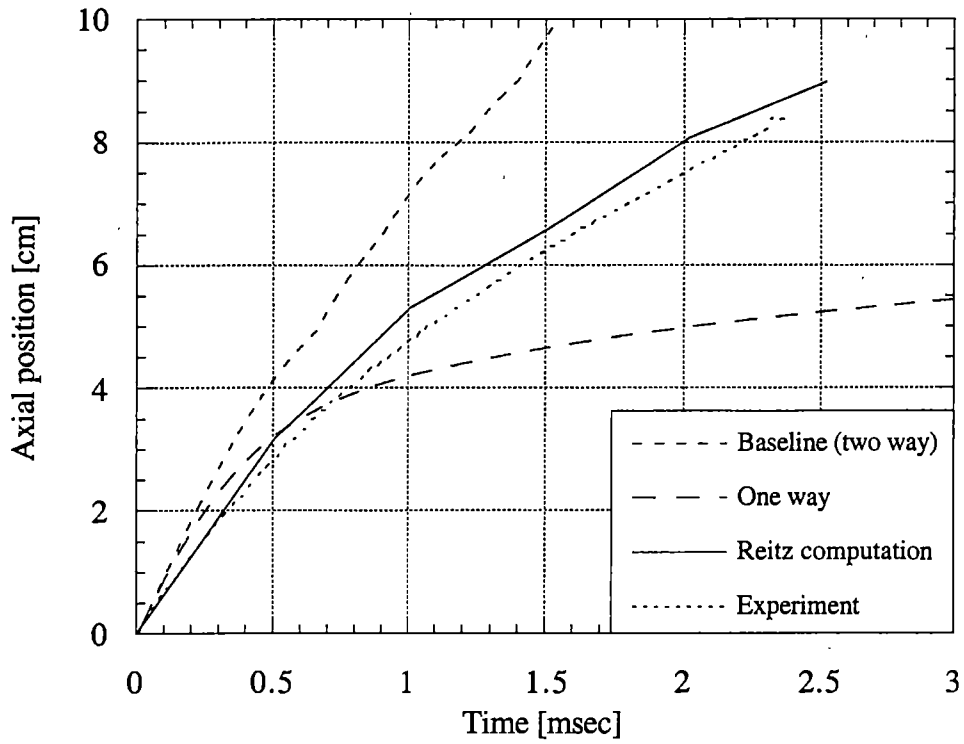


Figure 4-29. Spray Penetration Variation for Different Drag Routines.

4-29 is due to differences in the calculated gas flow. None of the results, however, accurately predict the experimental results.

As mentioned previously, an interesting feature common to almost all of the LISAM calculated spray penetration rates is the 'wavy' or non-smooth features seen in the curves. This waviness occurs when the parcel that is defined as the 'spray tip' changes, when the lead parcel slows and another parcel overtakes it. This leads to an important point of discussion of the definition of the spray tip. Reitz defines his tip to be "the location of the leading spray parcel." [4]. If this definition is taken to mean the first parcel injected into the system, rather than the parcel that is closest to the chamber exit, the spray tip penetration rate changes considerably. Figure 4-30 shows how significant the spray tip definition can be, also note that the waviness discussed previously is no longer present. If the tip is defined to be the first parcel that enters the system, the tip penetration rate shows the tailing off seen in the experiment [29] and predicted by Reitz's computation [4].

Finally, Figure 4-31 shows a LISAM simulation where the initial liquid injection velocity was reduced (60% of V_{inj}) until the spray penetration curve matched the experimental results. This simulates a 'ramp up' time at startup, the time it takes for the liquid velocity to reach its maximum injection value. By adjusting the initial conditions the LISAM prediction more closely matches the experimental results. LISAM neglects any effects due to evaporation and the subsequent increase in gas density would directly affect drop drag and therefore spray penetration. Additional research needs to be done to more completely evaluate the necessity of the inclusion of this phenomenon and appropriate methods to model the behavior.

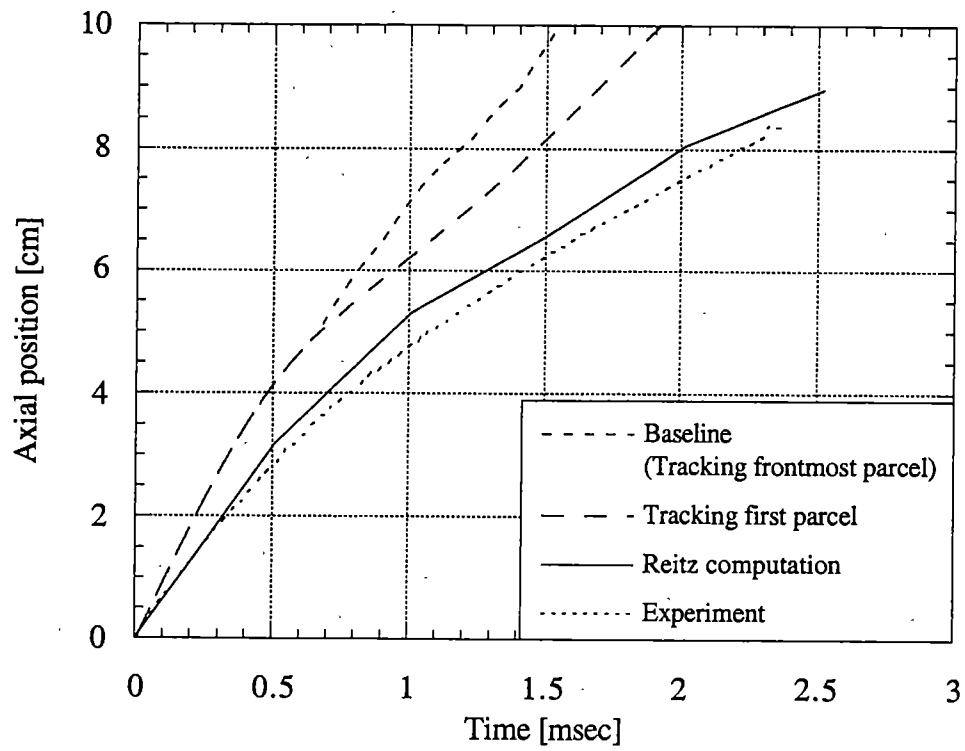


Figure 4-30. Variation in Spray Penetration with Various Definitions of Tip Location.

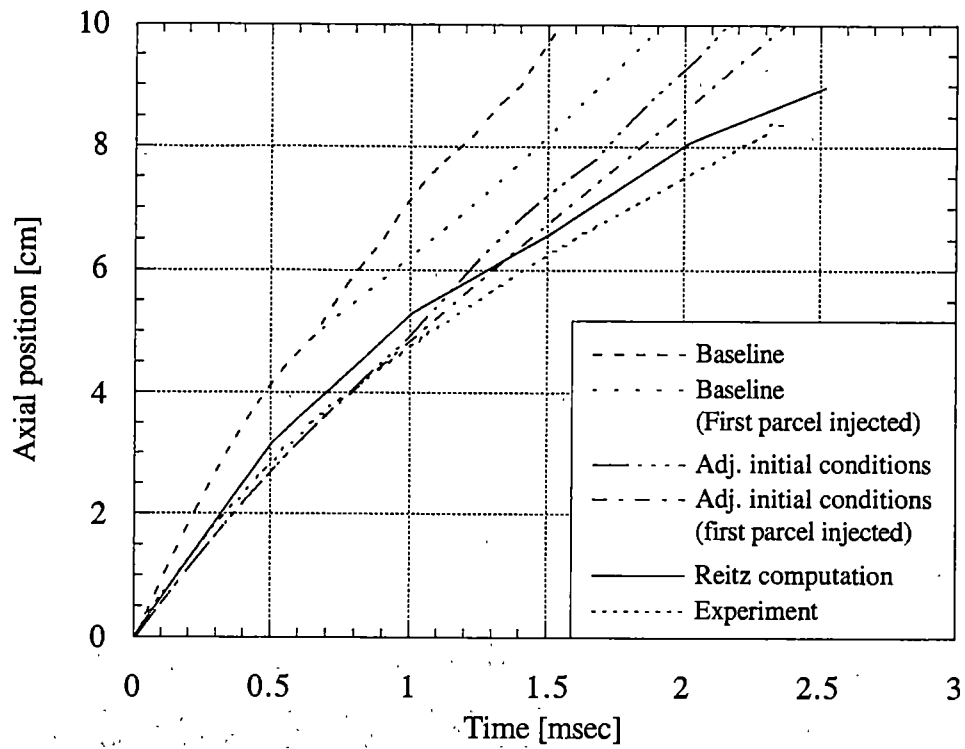


Figure 4-31. Spray Penetration Rate with Adjusted Initial Velocity.

4.3.1.5 Conclusions from Parametric Studies

From these parametric studies several conclusions were drawn about the basic behavior of the LISAM code. Variation in P_{inj} shows that great care needs to be taken to ensure that an appropriate level of computational parcels is maintained throughout the simulation; for these studies a value of $P_{inj}=10^5$ was found to provide adequate global measurements. The Reitz atomization model used in LISAM gave the best correspondence to the shape of the curve of the calculated drop sizes reported by Reitz [4], although it does not correspond well to the actual experimental values or those reported by Reitz using KIVA. This correspondence improves with the addition of collision modeling and when the tip is defined to be the first parcel injected into the system. A value of $B_1=20$ provided the best correspondence to the values calculated by Reitz [4] near the injector and B_1 had little impact on down-stream SMD values. The steady state LISAM predictions should improve somewhat with the addition of turbulence modeling. Some preliminary calculations based on arbitrarily increasing gas viscosity showed an increase in the LISAM-predicted SMD. This suggests that spray generated turbulence should be included in future versions of LISAM. The variations in the predicted results due to grid size and timestep variations were shown to be small enough to declare the results both timestep and grid independent for this case. With these studies complete, LISAM was applied to study another liquid/gas flow from a different injector. Simulations of the water/air experiments from the NASA Lewis Research Center [18] were conducted and are discussed in the following sections.

4.3.2 Comparison of LISAM results to Water/Air Experiment

The eight experimental cases described in Table 4-2, were modeled using LISAM. Simulations were run for long enough periods to achieve steady state results. Steady state was defined to be when the computed SMD at all axial stations stop changing. The water/air simulations were run for 10 msec. These cases used a coaxial injector and therefore both liquid and gas injection velocities were varied. The experimental results provided were limited to radial distributions of SMDs and mean axial velocities at 5.08 cm downstream of the injector. Computational results were measured at 5.1 cm downstream of the injector. A computational domain 6 cm in diameter and 6 cm in length was used. The chamber was made wide enough to minimize edge effects and to model the conditions of the unconfined spray in the experiment. Solid wall boundary conditions were used for these calculations, which may induce some unrealistic gas-phase recirculation to the system. 120 transverse grid cells (0.05 cm/cell) and 6 axial grid cells (1 cm/cell) were used to discretize the domain. The results of the parametric studies show that simulation results were greatly effected by radial grid density, and less so by axial grid density. A coarse axial grid density was used to reduce computational run time. A primary timestep of $\Delta t=2 \times 10^{-6}$ sec was used for cases w1 through w6, and $\Delta t=1 \times 10^{-6}$ sec was needed for cases w7 and w8. A tighter grid and smaller timestep were not found to significantly impact the qualitative or quantitative features of the predicted spray, but did greatly increased run times. Therefore, the calculations reported here used the coarse mesh and larger timestep.

4.3.2.1 Comparison of Experimental and Numerical Results

Figures 4-32 and 4-33 show the comparison of experimental and simulation SMD distributions for case w1. Figure 4-33 shows an enlarged view of the area near the centerline. These figures show three curves: the experimental results, the SMD predicted by LISAM, and the SMD curve predicted by LISAM with only those drops below 230 μm included in the prediction, because the experimental results came only from measured drops below 230 μm in diameter. The figures also includes the number of droplets that were measured for each data point in the LISAM computation. The predicted drop sizes near the centerline show good correlation with experimental results. Away from the centerline, the computational results begin to deviate from experiment. Extremely large drop sizes were predicted beyond the largest experimentally measured radius. At large radii, the number of drops measured for each average drop diameter declines rapidly and by 1.2 cm radius falls below the experimental level of statistical significance (6000 drops). Some of the large drop sizes predicted can be attributed to the lack of statistical accuracy. Figure 4-34 shows the comparison of experimental and simulation axial droplet velocity results. LISAM overpredicts the centerline velocity and crosses the experimental curve at about 0.75 cm radius and correlates well with the experimental results at larger radii. Also, the LISAM predicted particle velocity profile peaks off centerline, while the experimental curve peaks on the centerline. The velocity profile predicted by LISAM is what would be expected from a coaxial injector with gas velocities higher than the liquid core, and one would expect the same profile to occur experimentally. Zaller and Klem [18] noted this feature but had no explanation for its occurrence.

Results for cases w2 and w3 are presented in Figures 4-35 through 4-38.

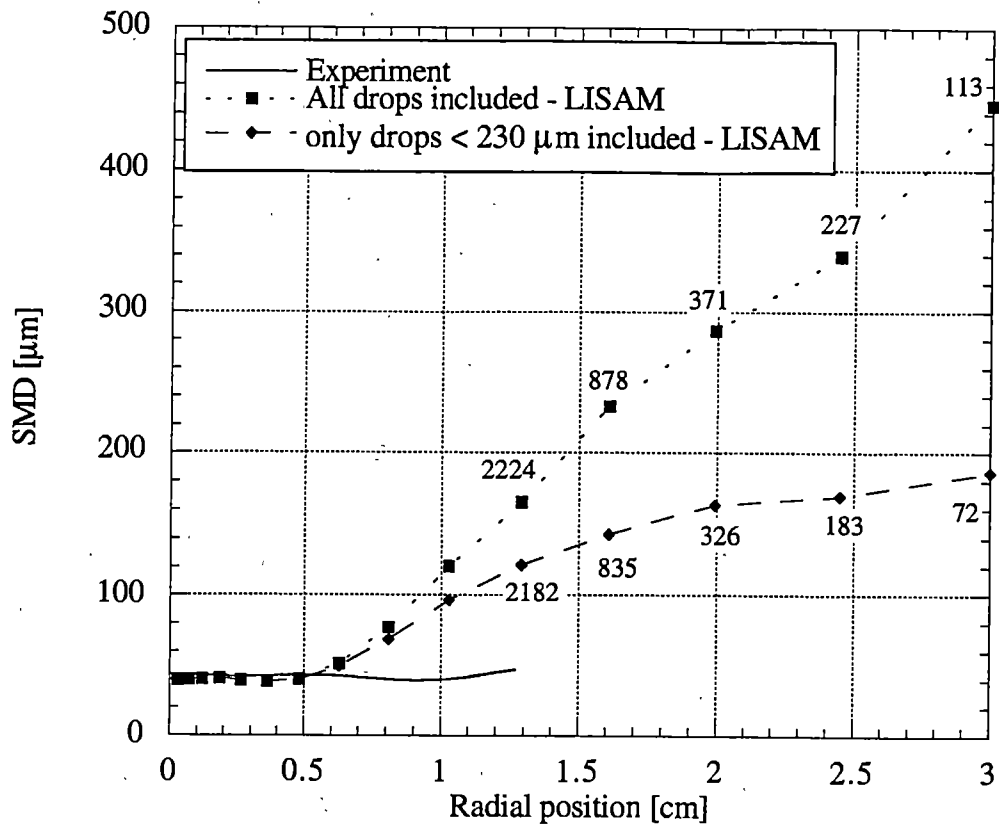


Figure 4-32. Comparison of Numerical and Experimental Drop Sizes for Case w1.

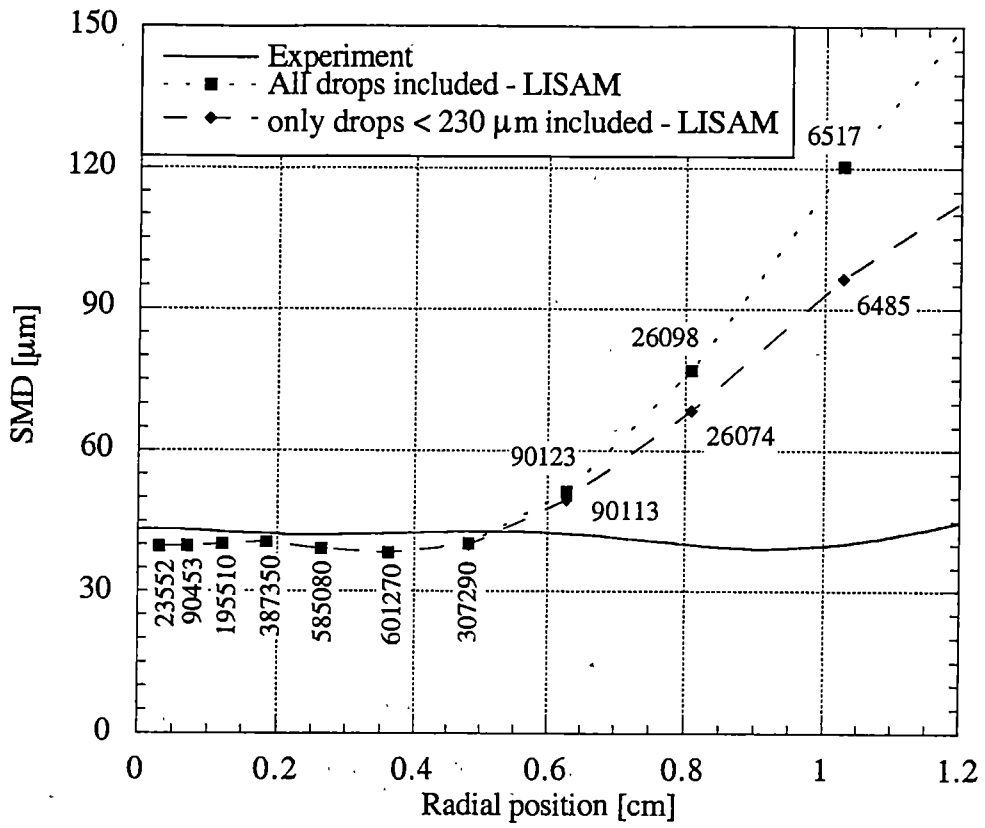


Figure 4-33. Comparison of Numerical and Experimental Drop Sizes for Case w1 (Enlarged View).

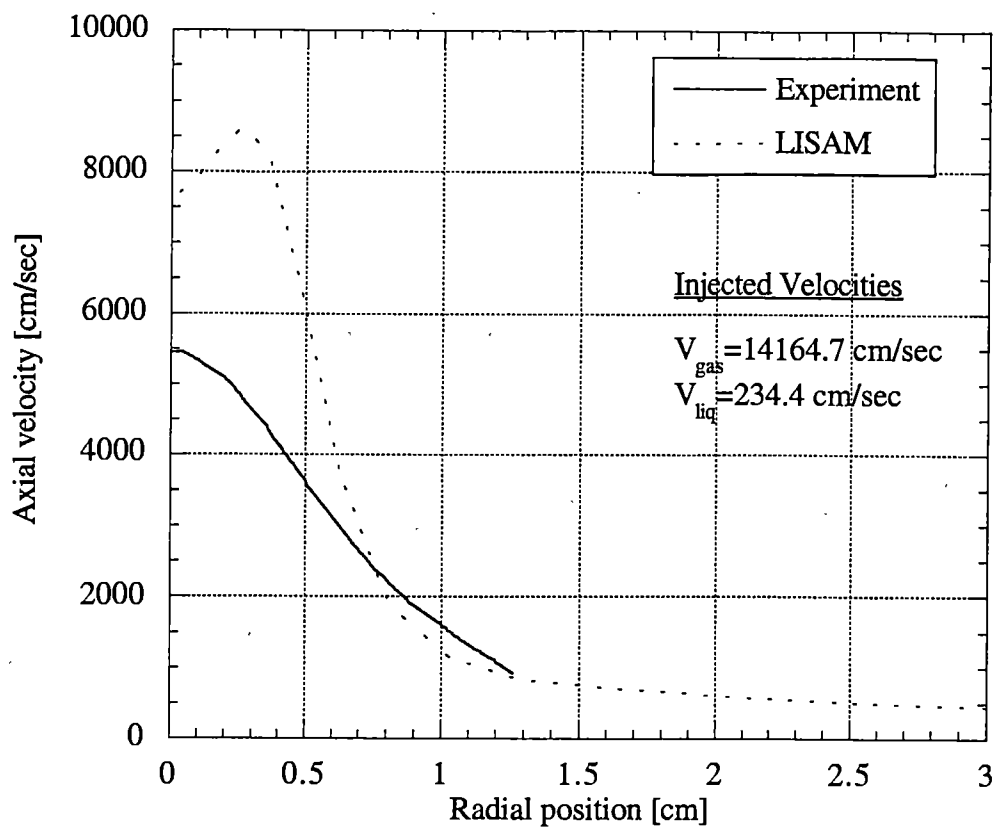


Figure 4-34. Comparison of Numerical and Experimental Axial Velocities for Case w1.

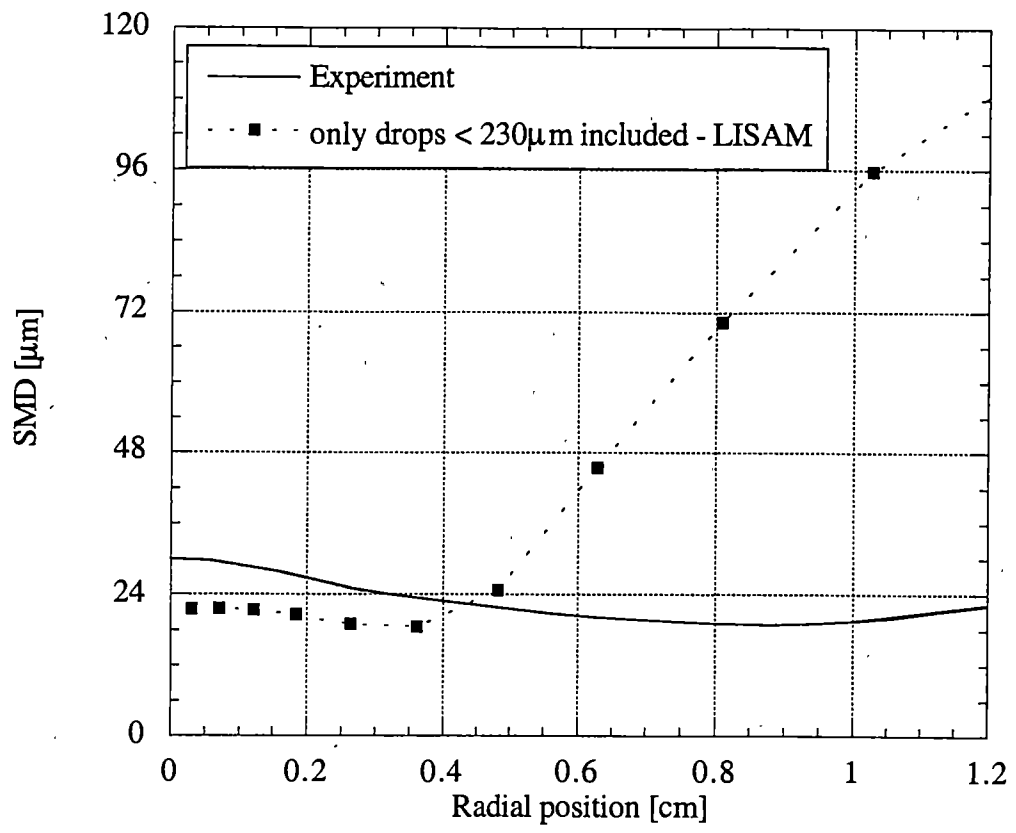


Figure 4-35. Comparison of Numerical and Experimental Drop Sizes for Case w2.

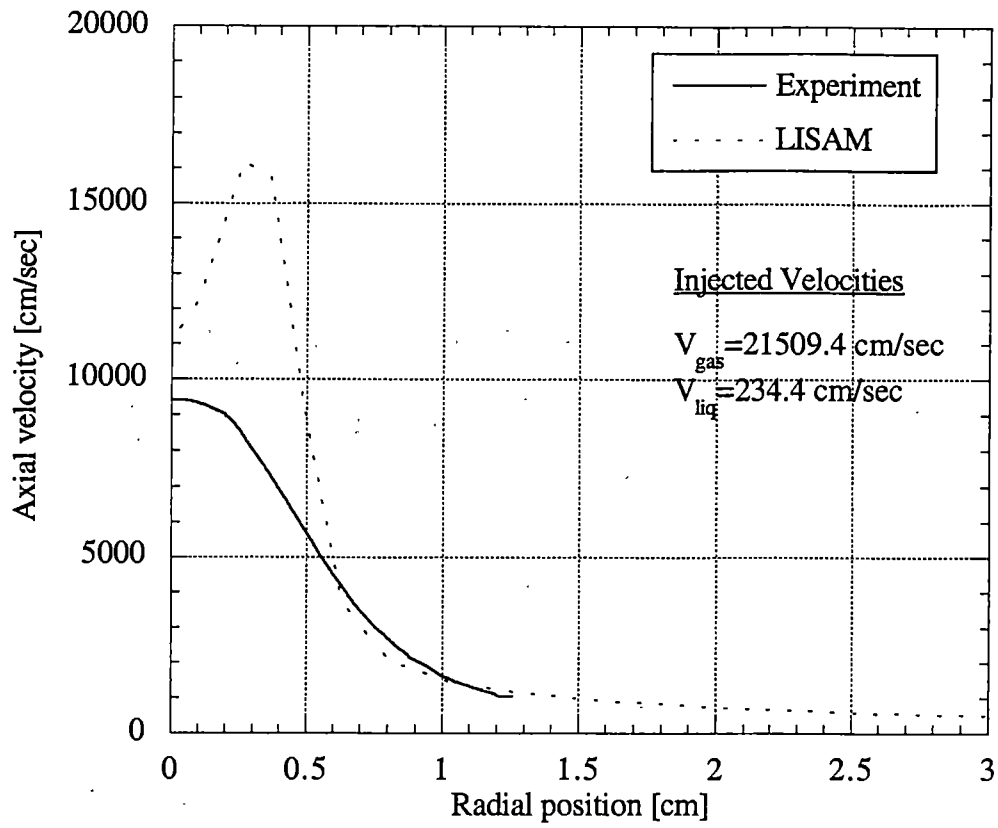


Figure 4-36. Comparison of Numerical and Experimental Axial Velocities for Case w2.

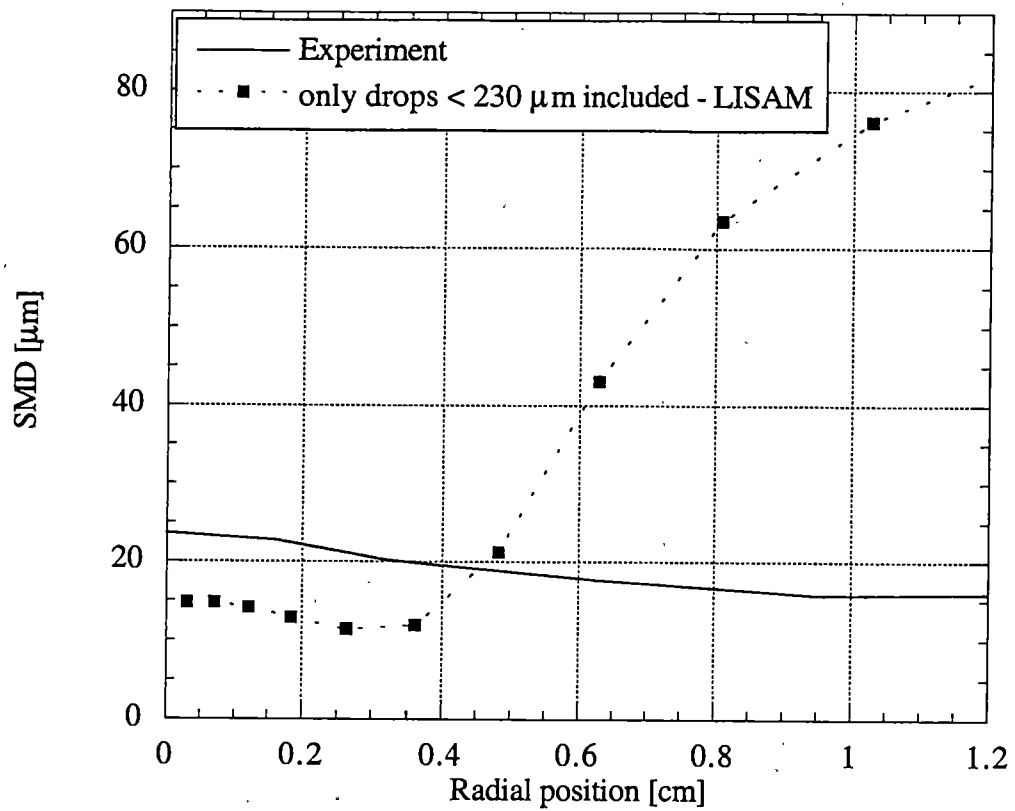


Figure 4-37. Comparison of Numerical and Experimental Drop Sizes for Case w3.

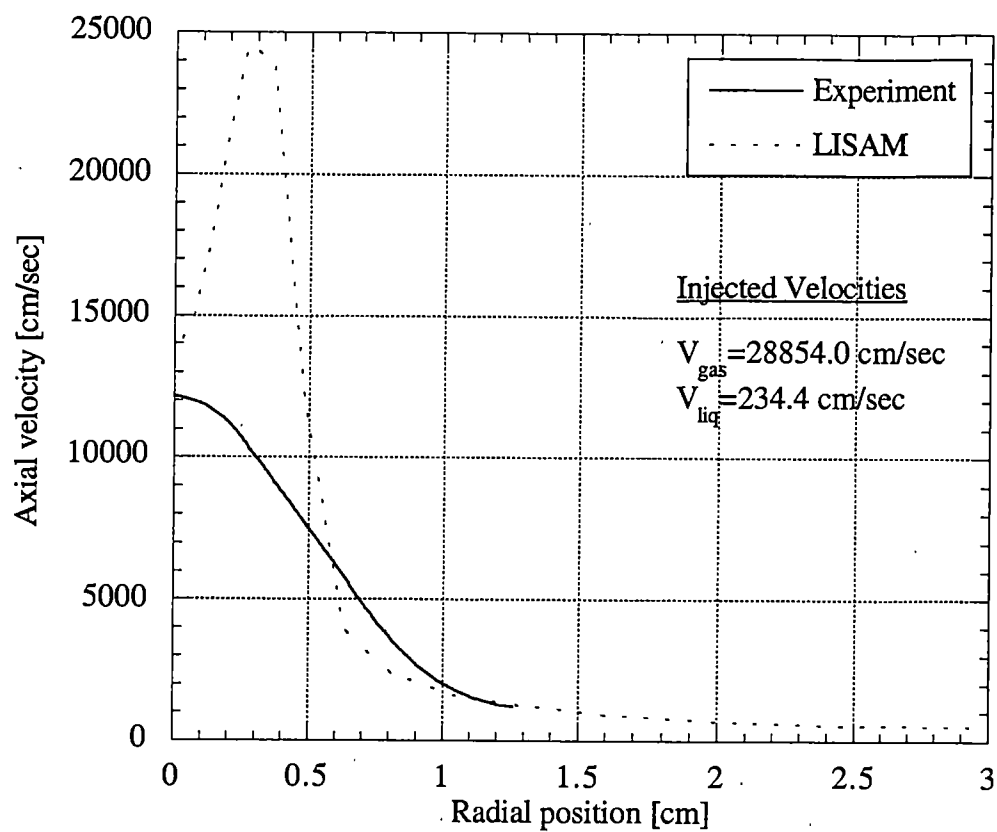


Figure 4-38. Comparison of Numerical and Experimental Axial Velocities for Case w3.

Results were similar to those seen in case w1. Figure 4-39 and 4-40 show drop size population distributions at two different radial locations in the 5.1 cm axial plane. Drops near the centerline, at 0.035 cm, have the highest population below 20 μm and no drops above 125 μm . At a larger radius (1.0 cm), the highest population still occurs below 20 μm , but there are drops with sizes above 600 μm . Figure 4-41 and 4-42 show the results from the simulations of case w4. This case differs from those shown previously; predicted drop sizes are very similar to the experimental values for the entire region of experimental data. The drop sizes beyond this region still increase to extremely large values beyond 1.2 cm as seen before, but as before, the statistical significance of these numerical data are questionable. The velocity profile (Figure 4-42) is also different from those seen previously. The centerline value predicted by LISAM is much smaller than seen experimentally, but the predicted value rises to match the experimental value at 0.3 cm radius, but does not tail off as fast as the experimental results. The case w5 results (Figures 4-43 and 4-44) are similar to those for w4, especially for drop sizes. The velocities predicted by LISAM underpredict the experimental values at all points. For case w6, LISAM underpredicts the experimental SMDs, but the predicted SMDs again rise at larger radii (See Figure 4-45). The average velocities predicted underestimate the experimental values for the majority of the experimental values, but overestimate the experimental values at a radial location beyond 1 cm (See Figure 4-46). The results for cases w7 and w8 (Figure 4-47 through 4-50) are similar to those of w5 and w6. LISAM underpredicts the experimental drop sizes, but predicts large drops at larger radii. The velocity profiles underestimate the experiment near the centerline and overestimate the experiment at larger radii.

In addition to the poor statistics seen on the outer edges of the simulated spray,

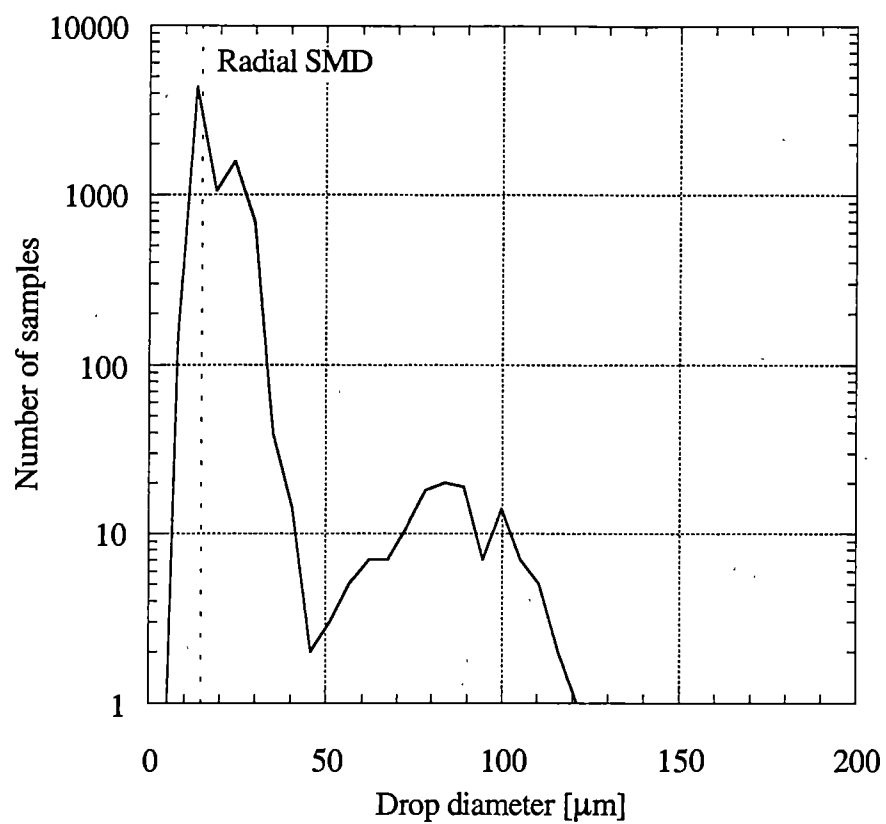


Figure 4-39. Drop Size Population Distribution at a Radius of 0.035 cm and an Axial Location of 5.1 cm for Case w3.

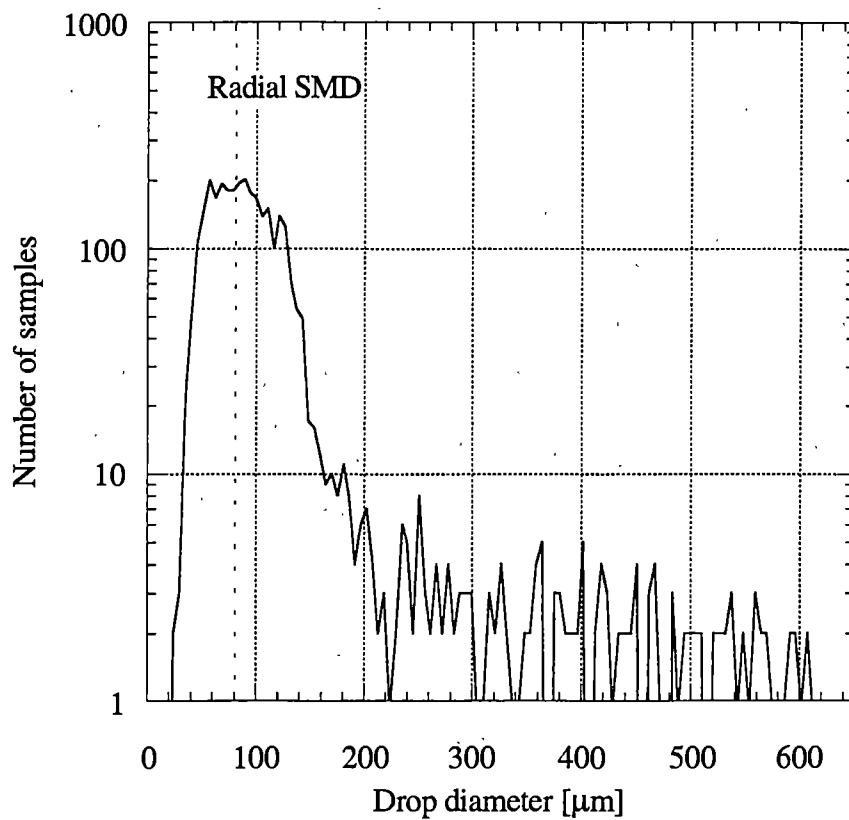


Figure 4-40. Drop Size Population Distribution at a Radius of 1.0 cm and an Axial Location of 5.1 cm for Case w3.

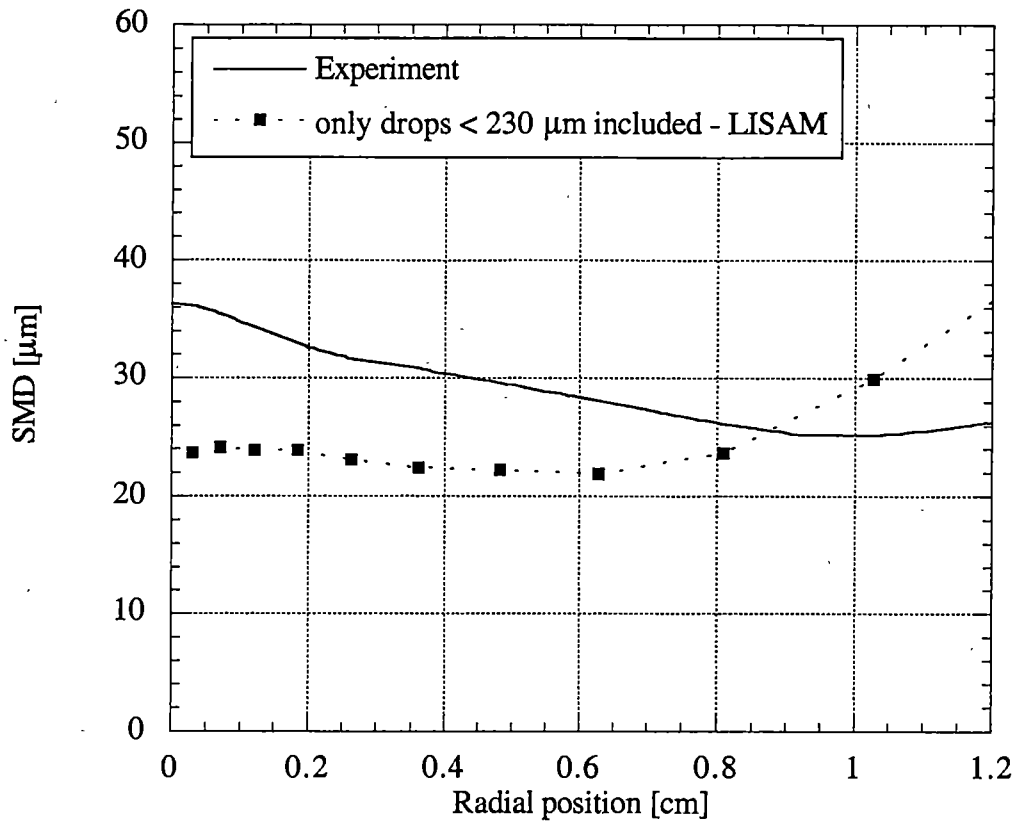


Figure 4-41. Comparison of Numerical and Experimental Drop Sizes for Case w4.

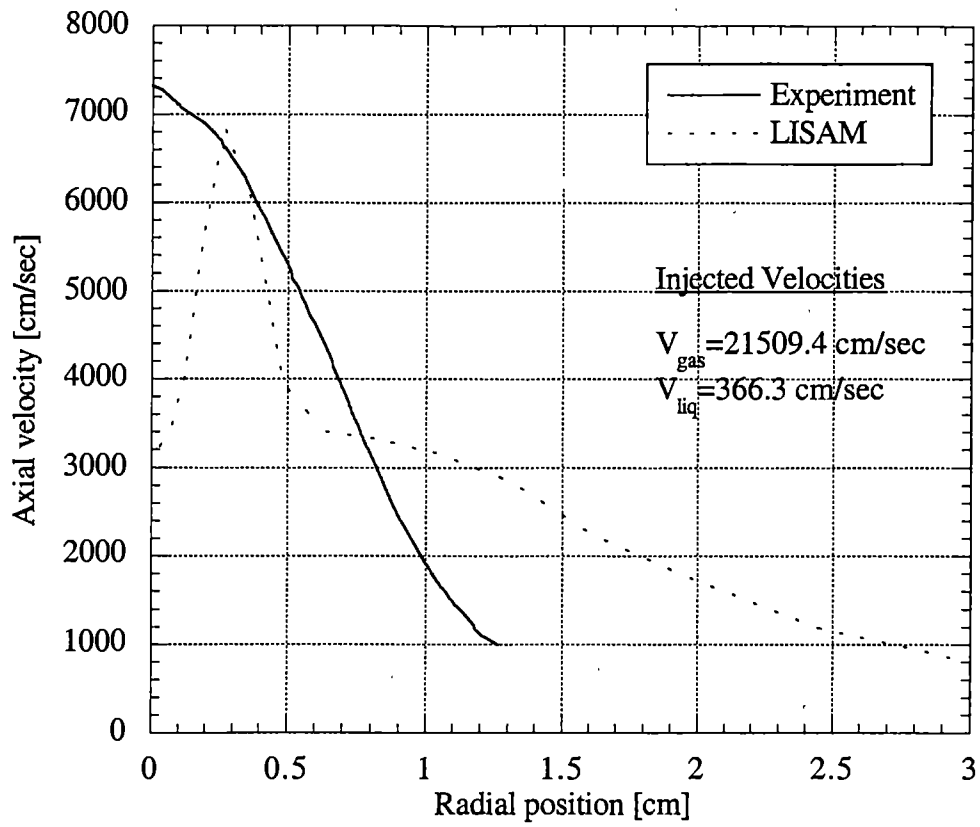


Figure 4-42. Comparison of Numerical and Experimental Axial Velocities for Case w4.

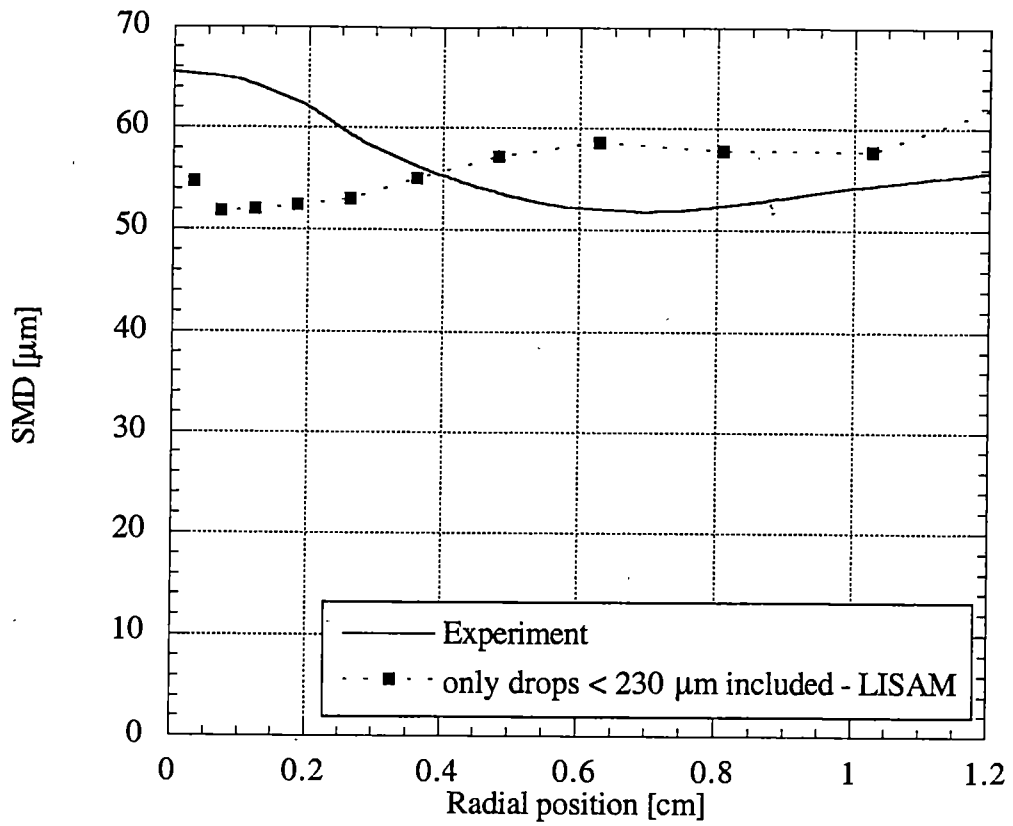


Figure 4-43. Comparison of Numerical and Experimental Drop Sizes for Case w5.

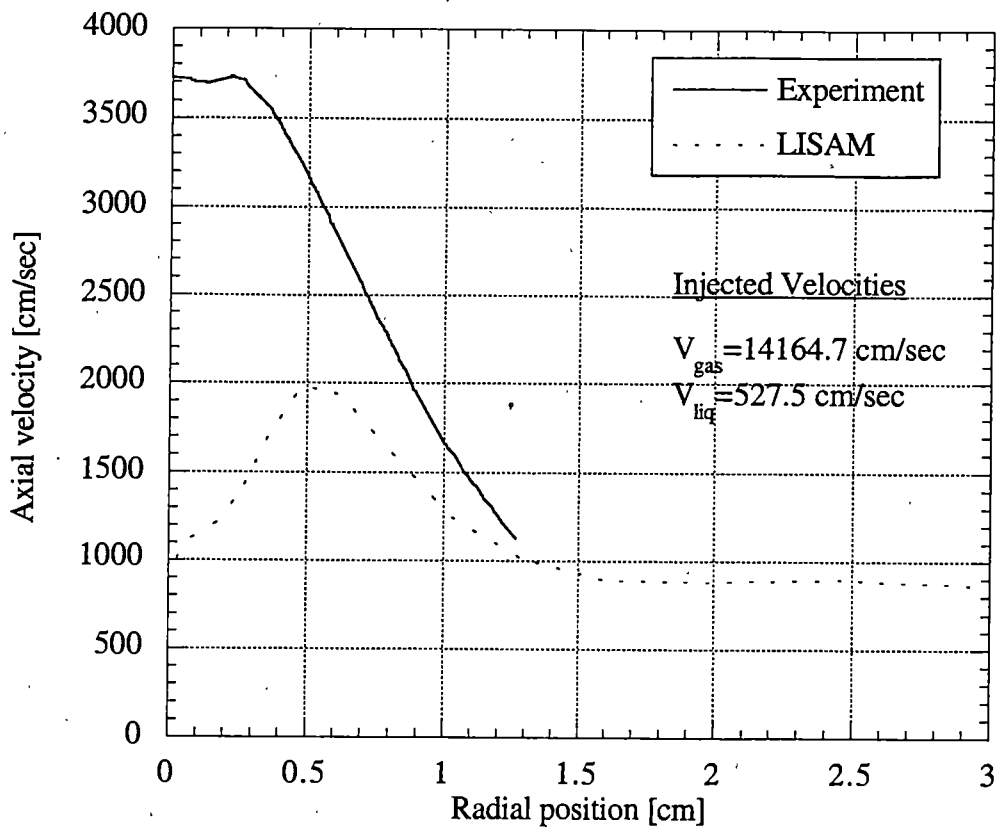


Figure 4-44. Comparison of Numerical and Experimental Axial Velocities for Case w5.

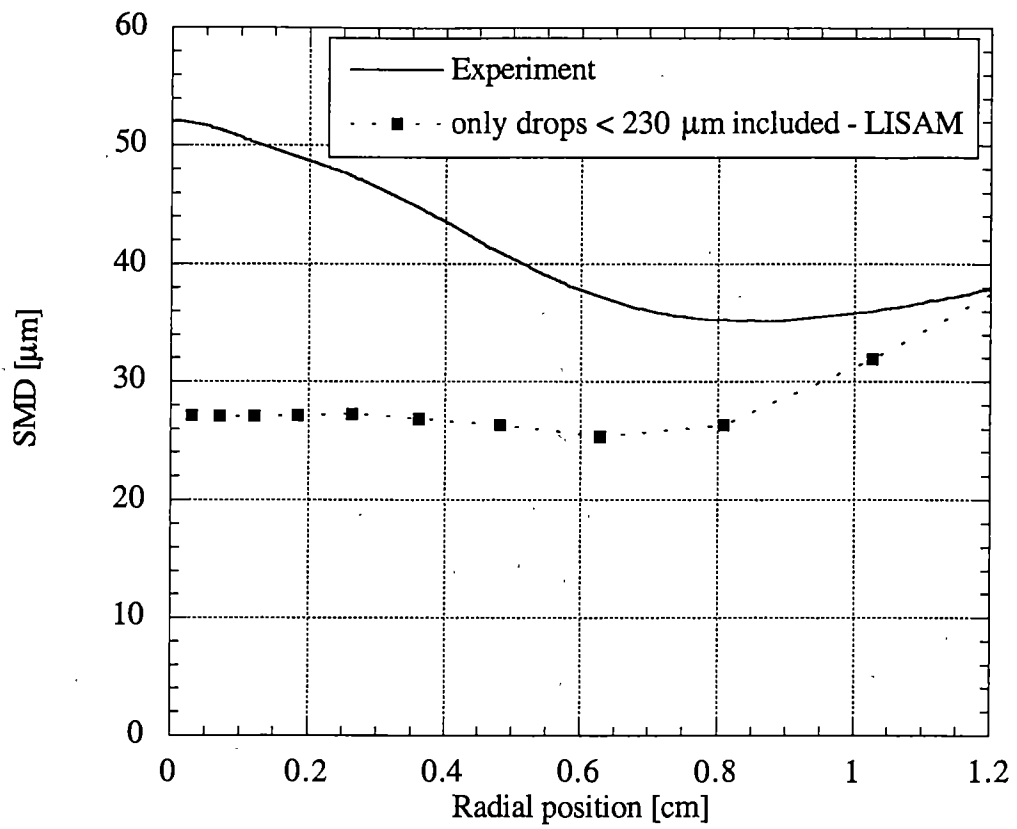


Figure 4-45. Comparison of Numerical and Experimental Drop Sizes for Case w6.

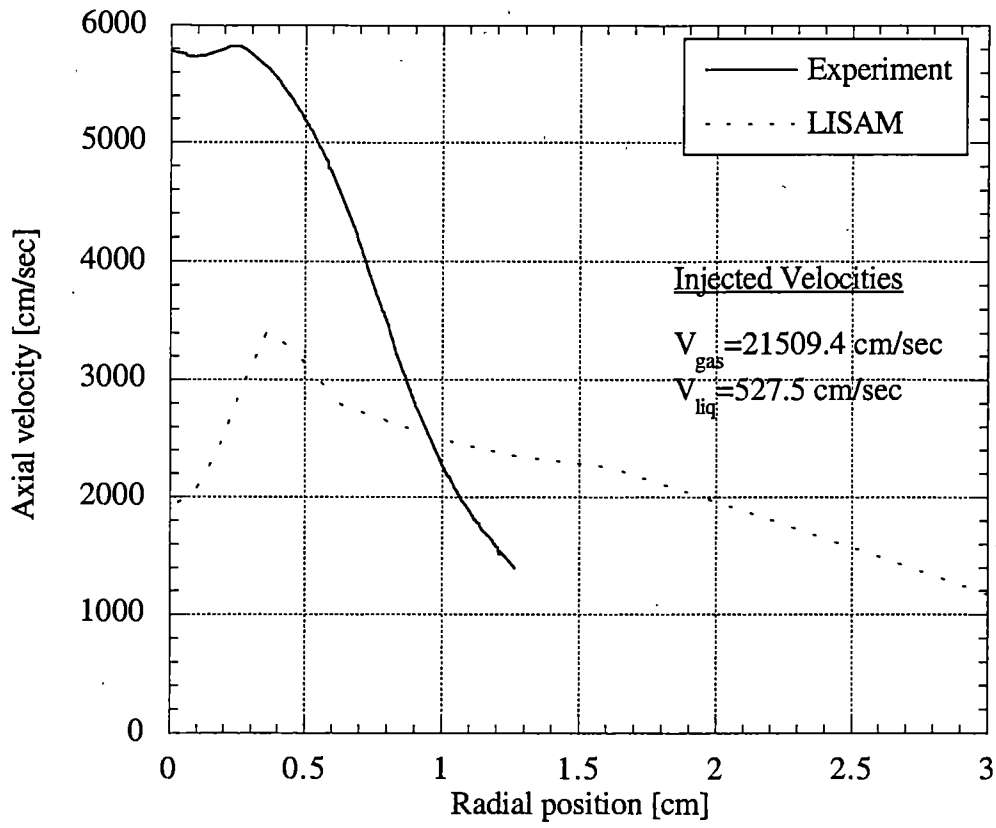


Figure 4-46. Comparison of Numerical and Experimental Axial Velocities for Case w6.

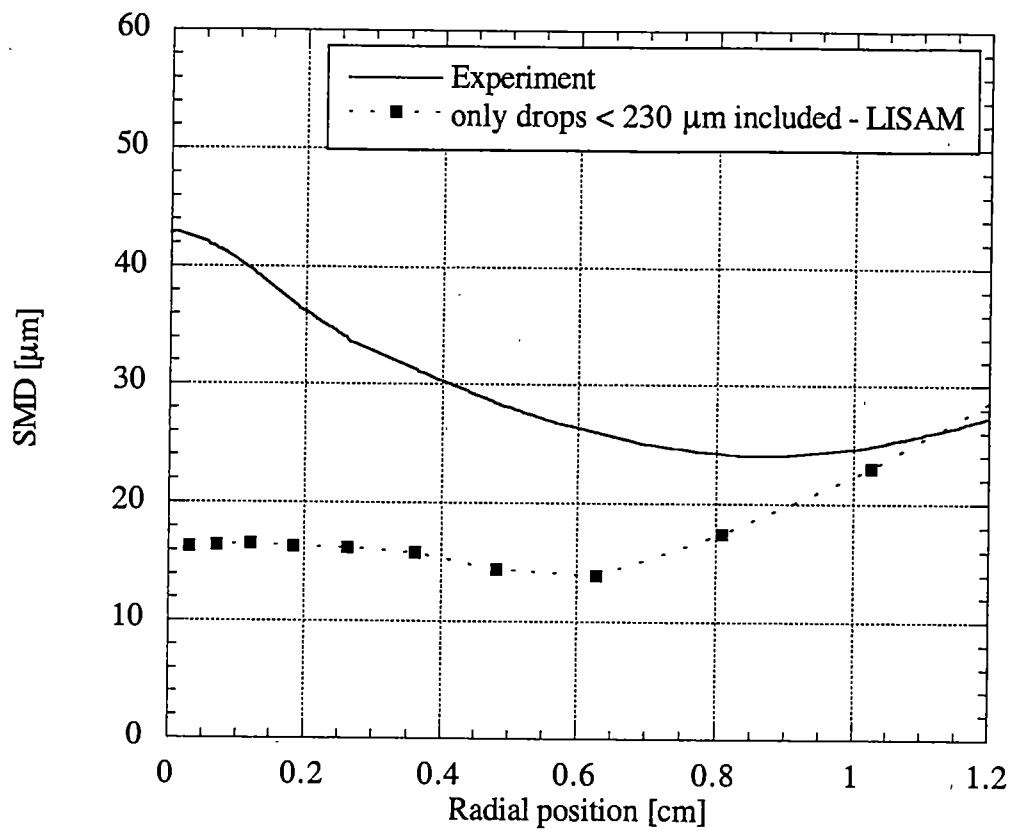


Figure 4-47. Comparison of Numerical and Experimental Drop Sizes for Case w7.

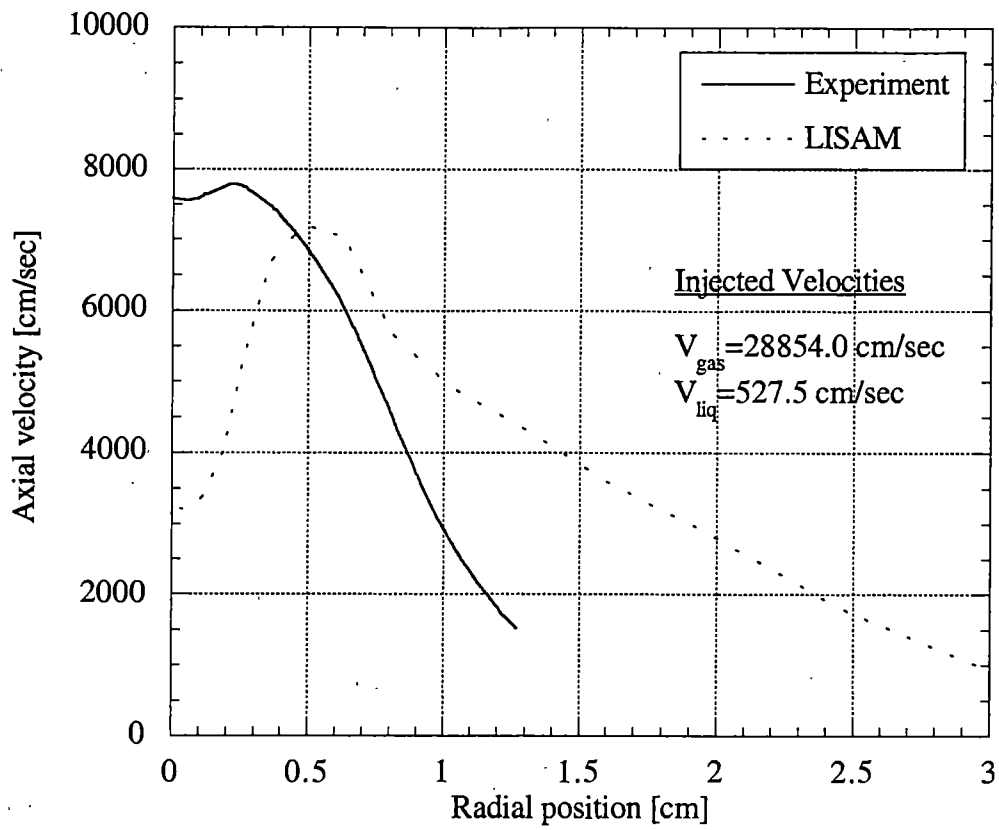


Figure 4-48. Comparison of Numerical and Experimental Axial Velocities for Case w7.

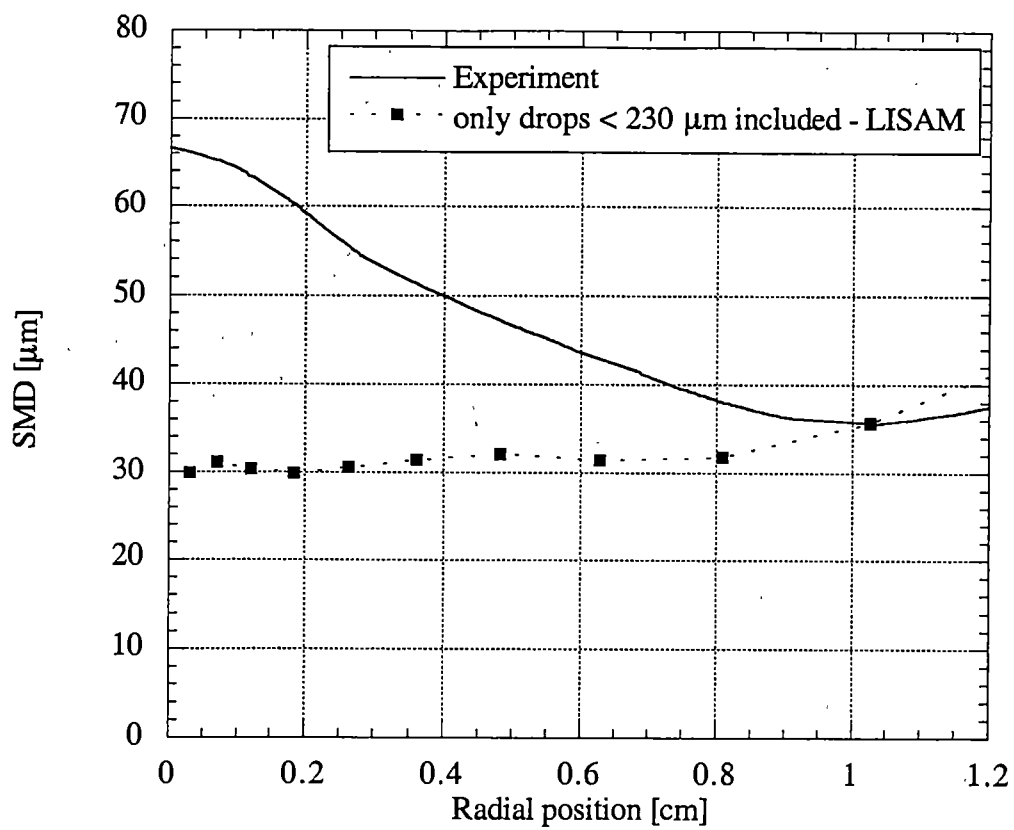


Figure 4-49. Comparison of Numerical and Experimental Drop Sizes for Case w8.

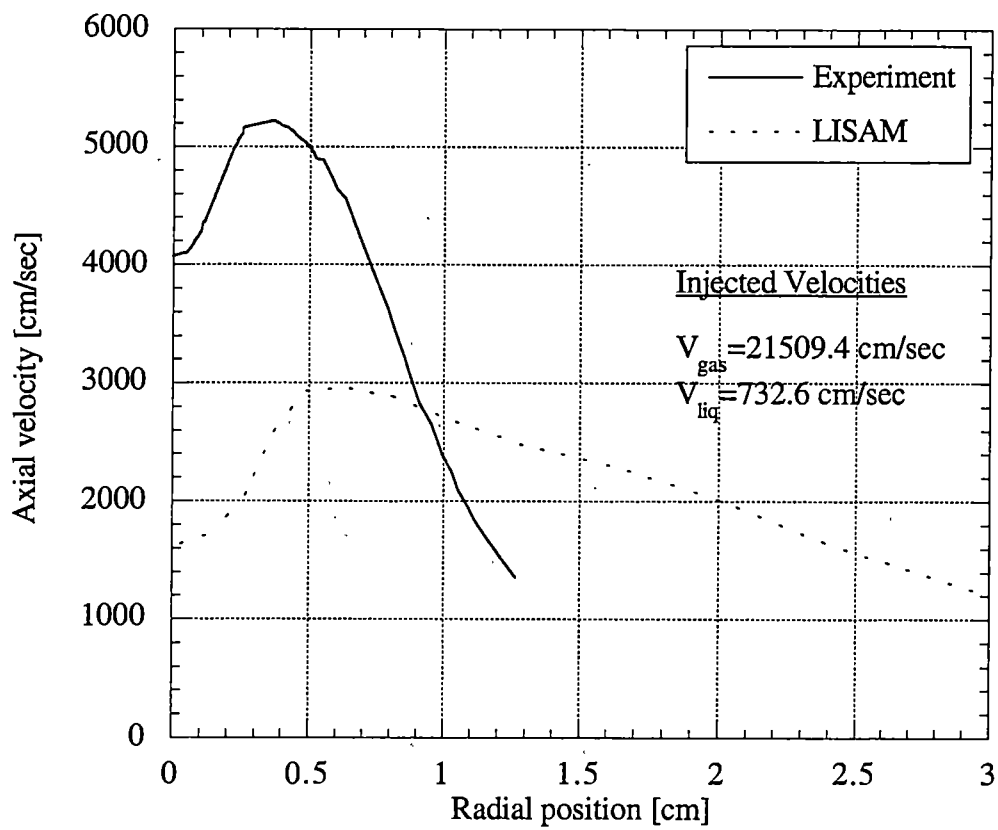


Figure 4-50. Comparison of Numerical and Experimental Axial Velocities for Case w8.

experimental factors affecting simulated drop sizes must be considered. No information is given in the experimental description regarding the surface roughness of the interior of the injector surface (the coaxial tube surfaces, Figure 4-1(a)). If there was significant surface roughness present, this would add additional turbulence and distortion to the liquid stream before it enters the computational domain [32]. These factors would increase the breakup seen on the edges of the spray resulting in smaller drops in these regions. It would also create additional spray dispersion moving more drops to the outer edges of the spray, which would improve the statistics in the outer region. These roughness effects are not modeled in LISAM.

Another factor is determining average drop sizes that should be studied is how that average is calculated. Figure 4-51 shows the radial drop size distribution for case w1 with drop size averages calculated in three different ways. The SMD calculation gives the largest average size, with the D_{mv} next and D_{10} giving the smallest. Each of these methods gives different weight to the size of a drop and the frequency of its appearance. The D_{10} distribution gives the smallest drop sizes because it is strictly an average of the drop diameters in the spray. This method gives less weight to parcels with larger, but fewer, drops and therefore predicts smaller sizes than other methods.

An interesting study was also conducted to determine the effects of initial drop size on the simulation results. Figure 4-52 shows the SMD distributions for various initial drop sizes. Drop sizes were varied from the original value of one nozzle diameter (0.132 cm or 1320 μm) to 20% of the nozzle diameter (264 μm). It is interesting to note that even for smaller initial drop sizes, large drops are predicted near the computational boundary. These average drop sizes are larger than the initial drop size for the $D_{noz}/3$ and $D_{noz}/5$ cases. This drop enlargement can occur in the Reitz

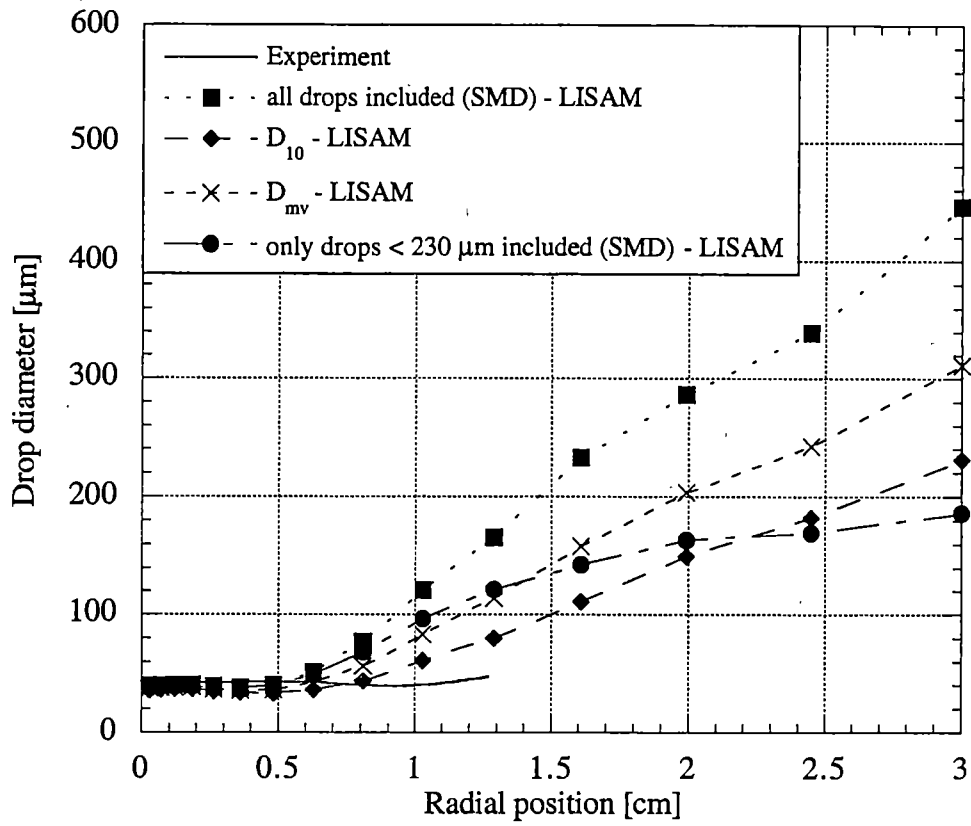


Figure 4-51. Comparison of the Effects of Methods of Average Drop Size Calculation.

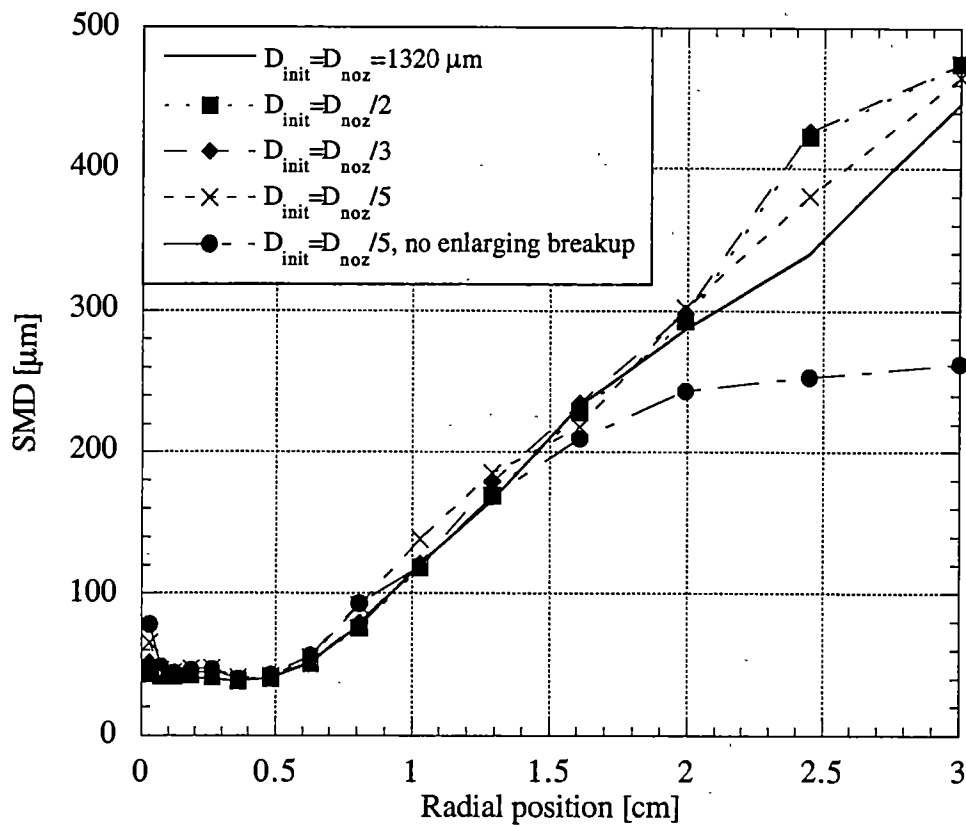


Figure 4-52. Effect of Varying Initial Drop Size.

atomization model because a drop-ligament can grow into a larger spherical drop in the Rayleigh breakup regime (See Section 2.3.1.1.1.1). An additional case was run with droplet growth or enlargement suppressed, and the results from that simulation are also shown in Figure 4-42. These results show that initial drop size does not greatly impact the downstream size distributions. Large drops will undergo more breakup and create more small drops while smaller initial drops will experience less breakup as they pass through the spray.

4.3.3 Summary of Computational Studies Using LISAM

Parametric studies and experimental comparisons were performed for fundamentally different liquid injector cases. The parametric studies showed that drop size predictions are sensitive to liquid modeling parameters, such as atomization model and collision model, and relatively less sensitive to gas modeling parameters. The spray tip penetration rate predicted by LISAM exhibited the opposite trends. It is primarily affected by gas modeling parameters, such as grid size and differencing algorithm, and is less influenced by liquid modeling variables. It does depend on the definition of the spray "tip" that is used. Turbulence modeling, not present in LISAM, is believed to be of importance and should be included in future modeling efforts. Statistical accuracy was also shown to be of great importance and care must be taken to ensure that adequate statistical representation of a spray is made, both experimentally and numerically.

The comparison between the NASA water/air experimental data and the LISAM predictions also yielded interesting information. The importance of a good experiment description was seen; it is vitally important to define in detail how the data was obtained and analyzed. This detail will directly effect how the spray is modeled and how the

computational results are analyzed. Also, the need and importance of a thorough description of the experimental setup was seen; the unknown surface roughness of the liquid injector used in these experiments call into question the smooth tube surface modeling assumptions used in LISAM. Some knowledge of the time involved in collecting the data would be useful to accurately compare predicted results to experimental results. If 20 minutes of experimental run time or sampling time was required at each measurement point in the spray to meet the requirements for statistical accuracy, this information is important to the modeler to ensure comparable spray statistics between experiment and predictions. The spray conditions predicted during the startup phase can be significantly different than those seen once a steady spray has been established. Knowledge of when the data was taken would allow the modeler to calculate drop size averages only during specific periods during the computation and better mimic the test conditions.

Chapter 5

Conclusions and Recommendations

5.1 Introduction

This chapter provides a summary and overview of the findings presented in this work. Conclusions drawn from the numerical studies are given and recommendations for future work are proposed.

5.2 Conclusions

Parametric studies yielded conclusions about drop size distributions and spray penetration behavior. Drop size distributions are highly dependent on liquid modeling parameters, such as: atomization model, empirical atomization constants, and collision model. Spray tip penetration rates are primarily dependent on gas modeling parameters such as grid spacing and convergence criteria and may also depend strongly on the transient of "ramp-up" behavior of the initial velocity of the spray droplets. Turbulence was not included in LISAM, but based on the comparison of LISAM results to results of Reitz, as well as on viscosity dependent parametric calculations (done, but not shown in the present study), is believed to have a impact on the predicted steady spray behavior, especially drop sizes. The sphere of influence (SoI) used in the collision model is very important and its size greatly impacts the predicted drop size distribution. Parcel injection rates must be large enough to ensure statistically significant results. Parcel injection rates that are too low result in poorly defined sprays and results that are not reliable. Trade-offs must be made in parcel injection rate and grid density to find a level that provides accurate predictions without resulting in unreasonably high run

times.

Steady state comparisons with NASA water/air experiments underscored the need for more complete experimental information. Experimental researchers need to provide as much detailed information on experimental setup and data acquisition as possible. More information about details of injector surface roughness and sample data acquisition times would greatly aid computational research. Researchers need also to provide more experimental results for simple test configurations to allow for more complete code validation. Experimental data on the initial transient period of the first few milliseconds of a liquid jet injection process near the injector face would be of great importance to improving and validating simulations such as LISAM. Also, simple test configurations that provide drop size and velocity distributions as well as spray penetration rates and even gas field visualization would be useful for detailed evaluation of code models.

5.3 Recommendations for Future Work

A turbulence model needs to be included in LISAM to improve steady state predictions. A method to account for injector wall surface roughness, in order to introduce additional *á priori* turbulence to the fluid could be useful, even critical, for improvement of simulation predictions. Additional numerical studies with more detailed numerical results are needed. Results such as: Details of drop trajectories, drop statistics, drop distributions, gas phase data, and grid sensitivity, would enable researchers to better predict and study spray atomization behavior.

References

References

- 1 Lefebvre, Arthur H., Atomization and Sprays, Taylor & Francis, 1989
- 2 Chigier, N. and Reitz, R.D., "Regimes of Jet Breakup and Breakup Mechanisms (Physical Aspects)", Recent Advances in Spray Combustion: Spray Atomization and Drop Burning Phenomena, Vol. 1, ed. Kuo, AIAA, 1996.
- 3 Ingebo, R.D., "Aerothermodynamic Effects on Liquid Jet Breakup in Two Fluid Fuel Nozzles", Recent Advances in Spray Combustion: Spray Atomization and Drop Burning Phenomena, Vol. 1, ed. Kuo, AIAA, 1996.
- 4 Reitz, Rolf D., "Modeling Atomization Processes in High-Pressure Vaporizing Sprays", Atomisation and Spray Technology, Vol. 3, No. 4, 1987, pp. 309-337.
- 5 Andrews, M.J., "The Large-Scale Fragmentation on the Intact Liquid Core of a Spray Jet", Atomization and Sprays, Vol. 3, 1993, pp. 29-54.
- 6 Reitz, R.D. and Diwakar, R., "Structure of High-Pressure Fuel Sprays", SAE Paper 870598, 1987.
- 7 O'Rourke, Peter J. and Amsden, A. A., "The TAB Method for Numerical Calculation of Spray Droplet Breakup", SAE Paper 872089, 1987.
- 8 O'Rourke, Peter J., "Collective Drop Effects on Vaporizing Liquid Sprays", Ph.D. Dissertation, Princeton Univ., 1981.
- 9 Reitz, Rolf D., "Atomization and Other Breakup Regimes of a Liquid Jet", Ph.D. Dissertation, Princeton Univ., 1978.
- 10 Faeth, G.M., "Structure and Atomization Properties of Dense Turbulent Sprays", Twenty-Third Symposium (International) on Combustion, The Combustion Institute, Pittsburgh, 1990.
- 11 Anderson, Dale A., Tannehill, J. C., and R. H. Pletcher, Computational Fluid Mechanics and Heat Transfer, Hemisphere Publishing Corp., Washington, 1984.
- 12 Amsden, A. A., O'Rourke, P. J., and T.D. Butler, "KIVA-II: A Computer Program for Chemically Reactive Flows with Sprays", LA-11560-MS, 1989.
- 13 Amsden, A. A., "KIVA-3: A KIVA Program with Block-Structured Mesh for Complex Geometries", LA-12503-MS, 1993.
- 14 Breisacher, Kevin, engineer, NASA Lewis Research Center, Personal Communication, 1994.
- 15 Dukowicz, John K., "A Particle-Fluid Numerical Model for Liquid Sprays", Journal of Computational Physics, Vol. 35, 1980, pp. 229-253.

- 16 Bird, G. A., Molecular Gas Dynamics and the Direct Simulation of Gas Flows, Clarendon Press, Oxford, 1994.
- 17 Taylor, G. I., "The Shape and Acceleration of a Drop in a High Speed Air Stream", The Scientific Papers of G. I. Taylor, ed. G. K. Batchelor, Vol. III, University Press, Cambridge, 1963.
- 18 Zaller, M. and Klem, M., "Coaxial Injector Spray Characterization Using Water/Air as Simulants", NASA TM 105322, 1991.
- 19 Taylor, G.I., "Generation of Ripples by Wind Blowing over a Viscous Fluid", Collected Works of G.I. Taylor, ed. G.K. Batchelor, Cambridge University Press, Cambridge, 1958.
- 20 Drazin, P.K. and Reid, W.H., Hydrodynamic Stability, Cambridge University Press, Cambridge, 1981.
- 21 Read, K.I. and Youngs, D.L., "Experimental Investigation of Turbulent Mixing by Rayleigh-Taylor Instability", UK AWRE report 011/83, 1983.
- 22 Chehroudi, B, Chen, S. H. and F.V. Bracco, "On the Intact Core of Full-Cone Sprays", SAE paper 850126, 1984.
- 23 Vardeman, Stephen B., Statistics for Engineering Problem Solving, PWS Publishing Co., Boston, 1994.
- 24 O'Rourke, P. J. and Bracco, F. V., "Modeling of Drop Interactions in Thick Sprays and Comparison with Experiments", Stratified Charge Automotive Engines, Institution of Mechanical Engineers, Pub. 1980-9, Nov. 1980, pp. 101-116.
- 25 Brazier-Smith, P. R., Jennings, S. G. and J. Latham, "The Interaction of Falling Water Drops: Coalescence", Proceedings of the Royal Society of London, A, Vol. 326, 1972, pp. 393-408.
- 26 Richardson, J.F. and Zaki, W.N., "Sedimentation and Fluidization: Part I", Trans. Instn. Chem. Engrs., Vol. 32, pp. 35-53, 1954.
- 27 Patankar, Suhas V., Numerical Heat Transfer and Fluid Flow, Hemisphere Publishing Corp., Washington, 1980.
- 28 Lefebvre, Arthur L., Gas Turbine Combustion, Hemisphere Pub. Corp., New York, 1983.
- 29 Hiroyasu, H. and Kadota, T., "Fuel Drop Size Distribution in Diesel Combustion Chamber", SAE Paper 740715, 1974.
- 30 Kuo, T. W. and Bracco, F. V., "Computations of Drop Sizes in Pulsating Sprays and of Liquid Core Length in Vaporizing Sprays", SAE Paper 820133, 1982.
- 31 Kuo, K., Principles of Combustion, John Wiley & Sons, New York, 1986.

- 32 Reitz, R. D. And Bracco, F. B., "On the Dependence of Spray Angle and Other Spray Parameters on Nozzle Design and Operating Conditions", SAE Paper 790494, 1979.

Appendices

Appendix A

Sample LISAM Input File

```
Tetradecane spray injected into N2. (Reitz case. 4/21/98)
none      Input restart filename (Enter none to start from zero).
restart_t1  Restart filename to write to.
5.e-3     Length of time to model (sec)
yes       Should subcycle output be written? (y/n)
1.e-4     Convergence criterion for drag sub-cycle.
10000     # of sub-cycle iterations.
500       # of cycles between output dumps, and restart writes.
1.e-6     Time step (sec)
1.e-6     Dual time step
no        Read grid in from file?
grid_t1    Name of grid file to open or to save to.
21        Number of grid cells in x direction (only useful
21        Number of grid cells in y direction if read file
21        Number of grid cells in z direction is no.)
20        Constant b1 for breakup routines
upwind    Axial differencing scheme (central/upwind)
1.e5      Injected comp. parcel flow (#/sec)
1.02e4    Injection velocity (cm/sec)
0.        Gas velocity in x direction (cm/sec)
0.        Gas velocity in y direction (cm/sec)
0.        Gas velocity in z direction (cm/sec)
298.      Liquid temperature (K)
21.8      Liquid surface tension (g/sec^2)
.01925    Liquid viscosity (dynes-sec/cm^2)
.77       Liquid density (g/cm^3)
1.e-2     Density convergence criterion
1.1e7     Chamber pressure (dynes/cm^2)
298.      Chamber temperature (K)
3011723.63 Gas constant (erg/g/K)
1.77268e-4 Gas viscosity (dynes-sec/cm^2)
0.        Gravitational acceleration in x direction (cm/sec^2)
0.        Gravitational acceleration in y direction (cm/sec^2)
0.0       Gravitational acceleration in z direction (cm/sec^2)
10.0      Chamber length (cm)
0.5       Chamber radius (cm)
0.045     Gas nozzle diameter(cm)
0.001     Post thickness (cm)
.03       Diameter of nozzle (cm)
0.0       Radial location of nozzle (cm)
drag      Use drag model or not - [drag or nodrag]
single    Single sphere or cluster drag model [single/cluster]
nocol     Use collision model or not - [col or nocol]
reitz     Name of atomization routine to use
- [reitz, andy, ndbt, tab, ndo or none]
```

Appendix B

Discretization of Gas Momentum Equation

The Delta form of the gas momentum equation is written as:

$$\begin{aligned} \Delta V_{\phi_x} + \Delta t \cdot [F_x(\Delta V_{\phi_x}) + G_y(\Delta V_{\phi_x}) + H_z(\Delta V_{\phi_x})] = \\ - \Delta t \cdot [F_x(V_{\phi_x}^n) + G_y(V_{\phi_x}^n) + H_z(V_{\phi_x}^n)] + \Delta t \cdot g_{\phi} - \frac{\Delta t}{\rho_{g_x}} \frac{dP}{d\phi} + S_{drop_{\phi_x}} \end{aligned} \quad (b.1)$$

where

$$\begin{aligned} \Delta V_{\phi_x} &= V_{\phi_x}^{n+1} - V_{\phi_x}^n \\ F_x(\chi) &= -\frac{\mu_g}{\rho_g} \frac{\partial^2 \chi}{\partial x^2} + u \frac{\partial \chi}{\partial x} \\ G_y(\chi) &= -\frac{\mu_g}{\rho_g} \frac{\partial^2 \chi}{\partial y^2} + v \frac{\partial \chi}{\partial y} \\ H_z(\chi) &= -\frac{\mu_g}{\rho_g} \frac{\partial^2 \chi}{\partial z^2} + w \frac{\partial \chi}{\partial z} \end{aligned}$$

In an Approximate Factorization method, equation (b.1) is written as [11]:

$$\begin{aligned} (1 + \Delta t \cdot F_x(-)) (1 + \Delta t \cdot G_y(-)) (1 + \Delta t \cdot H_z(-)) \Delta V_{\phi_x} = \\ - \Delta t \cdot [F_x(V_{\phi_x}^n) + G_y(V_{\phi_x}^n) + H_z(V_{\phi_x}^n)] + \Delta t \cdot g_{\phi} \\ - \frac{\Delta t}{\rho_{g_{ic}}} \frac{dP}{d\phi} + S_{drop_{\phi_{ic}}} - (\text{splitting error}) \end{aligned} \quad (b.2)$$

Using the approximate factorization method, equation (b.2), is solved in stages.

Three equations are solved sequentially. They are

$$[1 + \Delta t \cdot F_x(-)] \Delta \phi^{**} = \text{RHS} \quad (b.3)$$

$$[1 + \Delta t \cdot G_y(_)] \Delta \phi^* = \Delta \phi^{**} \quad (b.4)$$

$$[1 + \Delta t \cdot H_z(_)] \Delta \phi = \Delta \phi^* \quad (b.5)$$

where

RHS is all terms on the right hand side of equation (b.2).

Using second order central differencing for both first and second derivatives on the left hand side of equations (b.3), (b.4), and (b.5) allows a tridiagonal matrix solver to be used to solve for each level of $\Delta \phi$. The first derivative, using second order central differencing, is approximated as

$$\frac{\partial \chi}{\partial x} = \frac{\chi_{i+1} - \chi_{i-1}}{2h} \quad (b.6)$$

The second derivative, using second order central differencing, is approximated as

$$\frac{\partial^2 \chi}{\partial x^2} = \frac{\chi_{i+1} - 2\chi_i + \chi_{i-1}}{h^2} \quad (b.7)$$

where

χ is the variable being differentiated,

x is the variable being used to differentiate,

$h = x_i - x_{i-1}$, assuming uniform grid spacing [cm],

i is the point around which the derivative is being calculated.

If equations (b.6) and (b.7) are substituted into equation (b.3), it becomes

$$\Delta \phi^{**} - \frac{\mu_{\text{gas}} \Delta t}{\rho_{\text{gas}}} \left(\frac{\Delta \phi_{i+1}^{**} - 2\Delta \phi_i^{**} + \Delta \phi_{i-1}^{**}}{h^2} \right) + u_i \Delta t \left(\frac{\Delta \phi_{i+1}^{**} - \Delta \phi_{i-1}^{**}}{2h} \right) = \text{RHS} \quad (b.8)$$

Grouping like terms gives

$$\left(-\frac{\mu_{\text{gas}} \Delta t}{\rho_{\text{gas}} h^2} - \frac{u_i \Delta t}{2h} \right) \Delta \phi_{i-1}^{**} + \left(1 + \frac{2\mu_{\text{gas}} \Delta t}{\rho_{\text{gas}} h^2} \right) \Delta \phi^{**} + \left(-\frac{\mu_{\text{gas}} \Delta t}{\rho_{\text{gas}} h^2} + \frac{u_i \Delta t}{2h} \right) \Delta \phi_{i+1}^{**} = \text{RHS} \quad (\text{b.9})$$

This equation for all i forms a tridiagonal matrix, which can be solved numerically, using a tri-diagonal matrix solver [b-1].

The right hand side of equation (b.3) was discretized using a first order upwind (or central) scheme [b-1] for the first derivative and a second order central scheme for the second derivative for the interior points. The first and second derivatives are written as:

$$\chi_x = \frac{1}{h} (\chi_{i+1} - \chi_i) \quad (\text{upwind, } \chi_i < 0) \quad (\text{b.10a})$$

$$\chi_x = \frac{1}{h} (\chi_i - \chi_{i-1}) \quad (\text{upwind, } \chi_i > 0) \quad (\text{b.10b})$$

$$\chi_x = \frac{1}{2h} (\chi_{i+1} - \chi_{i-1}) \quad (\text{central}) \quad (\text{b.10c})$$

$$\chi_{xx} = \frac{1}{h^2} (\chi_{i+1} - 2\chi_i + \chi_{i-1}) \quad (\text{b.11})$$

On the boundaries, first order, one sided differencing was used. The derivatives for these points are written as:

$$\chi_{x_1} = \frac{\chi_2 - \chi_1}{h}; \quad \chi_{x_N} = \frac{\chi_N - \chi_{N-1}}{h} \quad (\text{b.12})$$

$$\chi_{xx_1} = \frac{\chi_3 - 2\chi_2 + \chi_1}{h^2}; \quad \chi_{xx_N} = \frac{\chi_{N+2} - 2\chi_{N+1} + \chi_N}{h^2} \quad (\text{b.13})$$

Once the right hand side of equation (b.3) is known, the left hand side of equation (b.3) can be solved simultaneously for all values of $\Delta\phi^{**}$ using a tridiagonal matrix solver.

Equations (b.4) and (b.5) are then solved in a similar fashion.

Vita

Nancy Diane O'Brien was born in Selma, Alabama on July 4, 1969. She was also raised in Selma. She attended Selma High School and graduated in 1987. She attended Auburn University with a National Merit Scholarship and graduated Magna Cum Laude with Bachelor of Science degree in Aerospace Engineering in 1991. She received a Master of Science degree in Aerospace Engineering from the University of Tennessee Space Institute in 1993. She was awarded a NASA Graduate Student Researcher Grant and the Zonta International Amelia Earhart Fellowship to begin her doctoral work, also at UTSI. Her Ph.D. was conferred in May, 2000.